Geology and Physical Properties Investigations by the InSight Lander

M. Golombek[1], M. Grott[2], G. Kargl[3], J. Andrade[4], J. Marshall[4], N. Warner[5], N. A. Teanby[6], H. E. Abarca[1], R. G. Deen[1], V. Ansan[7], E. Hauber[2], J. Voigt[2], R. Lichtenheldt[8], B. Knapmeyer-Endrun[9], A. Trebi-Ollennu[1], J. Singer[1], J. Maki[1], C. Schmelzbach[10], S. Kedar[1], D. Banfield[11], I. J. Daubar[1], D. Kipp[1], N. Muller[1], P. Lognonné[12], W. Folkner[1], S. Le Maistre[13], D. Mimoun[14], N. Murdoch[14], S. Piqueux[1], P. Delage[15], W. T. Pike[16], C. Charalambous[16], R. Lorenz[17], L. Fayon[12], S. Smrekar[1], A. Lucas[12], S. Rodriguez[12], P. Morgan[18], A. Spiga[19,20], T. Gudkova[21], Ö. Karatekin[13], M. Panning[1], R. Garcia[14], D. Giardini[10], U. Christensen[9], T. Nicollier[10], D. Sollberger[10], J. Robertsson[10], K. Ali[1], W. Kim[1], O. Khan[1], C. Sorice[1], P. Bailey[1], B. Kenda[12], M. Siegler[22], C. Vrettos[23], W. B. Banerdt[1]

[1]Jet Propulsion Laboratory, California Institute of Technology, Pasadena, CA 91109
[2]DLR, Institute of Planetary Research, Berlin
[3]Space Research Institute, Austrian Academy of Sciences
[4]Mechanical and Civil Engineering, California Institute of Technology, Pasadena, CA
[5]SUNY Geneseo
[6]School of Earth Sciences, University of Bristol, Wills Memorial Building, Queens Road, Bristol, BS8 1RJ, UK
[7]Laboratoire de Planétologie et Géodynamique, CNRS URM6112, Université de Nantes, Nantes, France
[8]DLR, Institute of System Dynamics and Control, Oberpfaffenhofen
[9]Max Planck Institute for Solar System Research, Göttingen, Germany
[10]ETH Swiss Federal Institute of Technology, Zurich, Switzerland
[11]420 Space Sciences, Cornell Center for Astrophysics and Planetary Science, Cornell University, Ithaca, NY, 14853
[12]Institut de Physique du Globe de Paris
[13]Royal Observatory of Belgium, Brussels
[14]Institut Supérieur de l'Aéronautique et de l'Espace (ISAE-SUPAERO), Université de Toulouse, 31400 Toulouse, France
[15]École des Ponts Paris Tech
[16]Imperial College, London
[17]Johns Hopkins University Applied Physics Lab
[18]Colorado School of Mines
[19]Laboratoire de Météorologie Dynamique (LMD/IPSL), Sorbonne Université, Centre National de la Recherche Scientifique, École Normale Supérieure, École Polytechnique, Paris, France
[20]Institut Universitaire de France, Paris, France
[21]Schmidt Institute of Physics of the Earth
[22] Planetary Science Institute
[23]University of Kaiserslautern

v. 5, January 25, 2018
Submitted to Space Science Reviews, Pre-landing InSight Issue

Abstract

Although not the prime focus of the InSight mission, the geology and physical properties investigations provide critical information for both placing the instruments on the surface and understanding the nature of the shallow subsurface and its effect on transmitted seismic waves. Two color cameras on the lander will obtain multiple stereo images of the surface and its interaction with the spacecraft. Images will identify the geologic materials and features present, quantify their areal coverage, help determine the basic geologic evolution of the area, and provide ground truth for orbital remote sensing data. A radiometer will determine the hourly temperature of the surface in two spots, which will determine the thermal inertia of the surface materials present and their particle size and/or cohesion. During the first two weeks after landing, these investigations will support the selection of instrument placement locations that are relatively smooth, flat, free of small rocks and load bearing. Location of the lander in high-resolution orbital images and direct-to-earth spacecraft tracking will yield the best located position on Mars in both inertial and cartographic space. Soil mechanics parameters and elastic constants of near surface materials will be determined from experiments with the arm and scoop of the lander (indentations, scraping and trenching), passive monitoring of seismic waves, mole penetration and thermal conductivity measurements from the surface to 3-5 m depth, and the measurement of seismic waves during mole hammering. These investigations will determine and test the presence and mechanical properties of the expected 3-17 m thick fragmented regolith (and underlying fractured material) built up by impact and eolian processes on top of Hesperian lava flows and determine its seismic properties for the seismic investigation of Mars' interior.

1. Introduction

The InSight (**In**terior Exploration using **S**eismic **I**nvestigations, **G**eodesy and **H**eat **T**ransport) mission is a Discovery Program lander to investigate the internal structure of Mars and the differentiation of the terrestrial planets (Banerdt et al. 2018). The spacecraft carries a seismometer (SEIS, Lognonné et al. 2018) with a Wind and Thermal Shield (WTS), heat flow probe (Heat Flow and Physical Properties Package, HP^3, Spohn et al. 2018) and a precision tracking system (Rotation and Interior Structure Experiment, RISE, Folkner et al. 2018) to measure the size and state of the core, mantle and crust. The lander is designed to operate on the surface for one Mars year after landing (November 2018), listening for marsquakes and impacts, measuring heat flow (including the surface temperature), and tracking the precession and nutation of the spin axis. The spacecraft is based on the Phoenix (PHX) lander and consists of a cruise stage, aeroshell, and backshell. It will land on smooth plains below -2.5 km elevation (for entry, descent and landing) and between 3°-5°N latitude (for solar power and thermal management) in western Elysium Planitia, which also satisfies other engineering and instrument deployment constraints (Golombek et al. 2017).

The spacecraft also carries a meteorology package (Banfield et al. 2018), a magnetometer (Banfield et al. 2018), two color cameras to image the surface (Maki et al. 2018), and an arm to deploy the instruments onto the surface (Trebi-Ollennu et al. 2018), that together allow investigations of the atmosphere, surface geology and physical properties of surface materials (Banerdt et al. 2018). The geology investigation on InSight is considered ancillary science that does not interfere with the main science requirements or objectives of the mission. Although determination of physical properties of surface materials during penetration of the heat flow probe or mole into the subsurface and the derivation of thermal inertia by the surface radiometer is part

of the HP^3 instrument investigation (Spohn et al. 2018), the physical properties of surface materials will also be studied by SEIS, both passively (e.g., Knapmeyer-Endrun et al. 2017) and actively during HP^3 hammering (Kedar et al. 2017), and via interactions of the scoop at the end of the arm (Trebi-Ollennu et al. 2018) with the surface. Both investigations are relevant to deploying the instruments on the surface and understanding the physical properties of the subsurface is important for interpreting the waveforms detected by SEIS. As a result, both investigations provide important information that supports the main science objectives of the mission. The geology and physical properties investigations are being developed and operated during the mission by two science theme groups, the Geology and Near Surface Properties theme groups; the change detection portion of geology (eolian activity) is being coordinated with the Atmospheres theme group.

The goal of this paper is to describe in one location, the geology and physical properties investigations planned by the InSight mission. Measurement of the physical properties by SEIS and HP^3 are described in the corresponding instrument papers and referenced and summarized herein, but this paper additionally includes contributions from the arm and scoop and explores the synergy between all of the measurements. Investigation of the geology of the landing site makes use of images acquired by the color cameras and the definition of surface materials and terrains observed in them as well as their physical properties. This paper begins with a brief description of the instruments and Instrument Deployment Arm (IDA) that are relevant to the geology and physical properties investigations. Next the landing site in Elysium Planitia and its geologic setting are described to frame the surface observations to be made by the lander. In addition, surface operations surrounding the selection of the locations to place SEIS and HP^3 instruments on the surface are described because many of these data products and mapping tasks are part of the geology and physical properties investigations. The geology investigation is described with special

reference to meteorology observations and their relation to eolian activity (motion of sand, granules and smaller grains, migration of bedforms, and dust devil tracks). Next the determination of the lander location in cartographic and inertial frames is described, which is a byproduct of the RISE investigation. The description of the physical properties investigation includes the contributions from HP^3, SEIS (both passive and active), and the IDA and includes a description of sophisticated terramechanics models that will help interpret the granular interactions during mole penetration and contact of the scoop with surface soils. Finally, results from the geology and physical properties investigations can be compared with predictions from remote sensing data and modeling investigations carried out during the landing site selection process (Golombek et al. 2017).

2. Instruments and Spacecraft Systems Relevant to Geology and Physical Properties

2.1. IDA

The InSight Instrument Deployment System (IDS) is comprised of the Instrument Deployment Arm (IDA), scoop, five finger "claw" grapple, motor controller, arm-mounted Instrument Deployment Camera (IDC), lander-mounted Instrument Context Camera (ICC), and control software (Trebi-Ollennu et al. 2018) (Figure 1). IDS is responsible for the first robotics precision instrument placement and release (seismometer and its wind shield and heat flow probe) on a planetary surface that will enable scientists to perform the first comprehensive surface-based geophysical investigation of Mars.

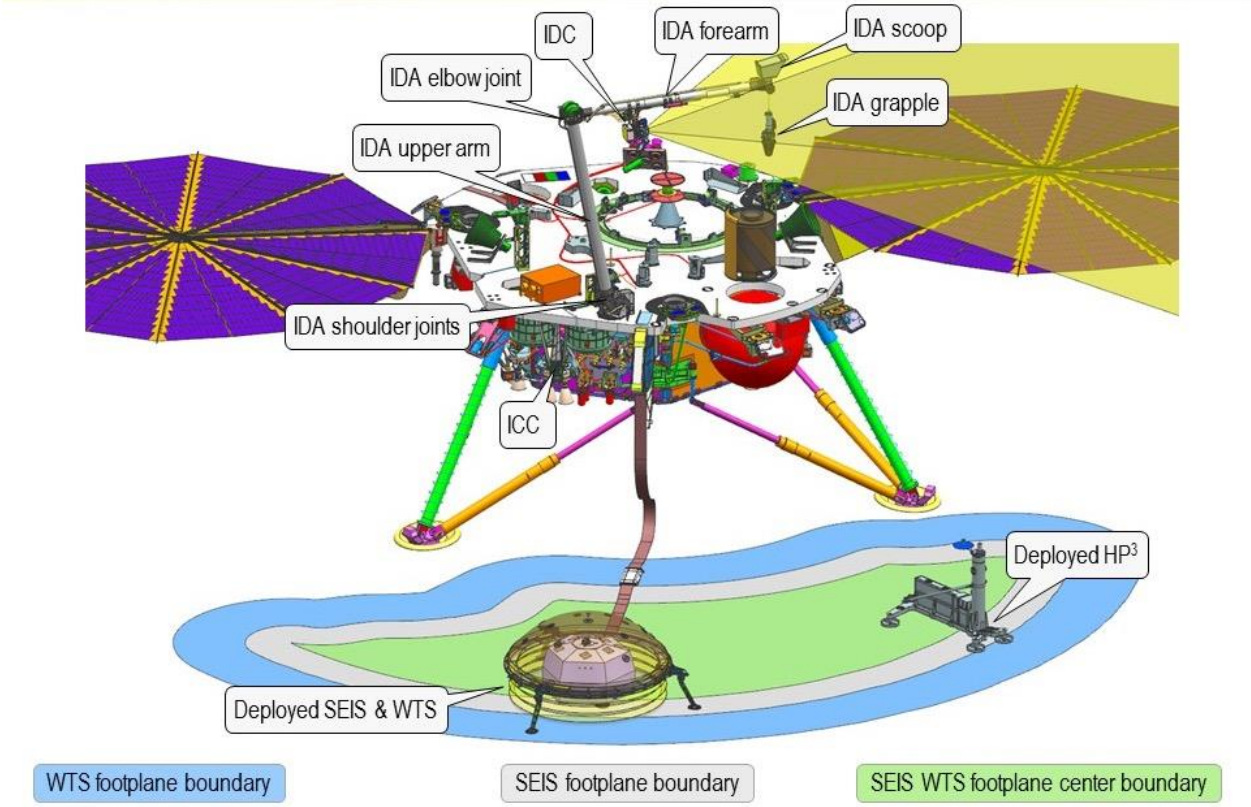

Figure 1. Perspective view of the InSight lander with IDS elements labeled is shown as well as the workspace and instruments deployed on the surface in their preferred positions (SEIS as far away as possible from the lander legs, HP^3 as far away from the lander as possible and >1 m to the right (east), from SEIS). The camera view of the IDC looking down the IDA from its mount near the IDA elbow is also shown in yellow. The green shows the boundary of the center point of the SEIS and WTS in the workspace. The gray shows the additional extent of the SEIS and the blue shows the additional extent of the WTS. Note that the ICC is mounted in a fixed position below the lander deck with most of the deployment area in its fish eye view. The IDA attachment to the deck is the origin of the IDA deployment reference frame with +X away from the lander (south), +Y to the right (from the lander or west), and +Z down. The SEIS tether is shown in its partially deployed state with the field joint near the lander. The grapple is shown in the unstowed state, hanging from the arm, in much of the field of view of the IDC. Workspace imaging during the ISSWG occurs with the grapple in the stowed configuration, attached to the IDA forearm.

The IDA is the flight arm from the original Mars ’01 lander that has been refurbished and rebuilt. It is a four degree of freedom back-hoe design manipulator with a 1.8-m reach that provides the following motion: yaw (shoulder azimuth) and three pitch joints (shoulder elevation, elbow, and wrist). The IDA links are made of titanium and, during normal operations, the actuators are

capable of generating 35, 120, 65, and 10.5 N-m of torque at the joints. The IDA can lift and deploy a 9 kg payload on Mars (33 N) at 1.65 m distance. The force the IDA end-effector can exert is configuration dependent, but the average is typically around 80 N.

Each joint has a temperature sensor and heater with a dust seal to prevent contamination of the motor and gearbox. The IDA is designed to withstand expected environmental temperatures from -110° to + 70°C, in a CO_2 atmosphere, with pressure as low as 5 torr. Each of the IDA joints consist of a brushed direct current motor with two-stage speed planetary gears and a harmonic drive at the output (except the wrist, which has a bevel gear at the output of the planetary gears). The IDA joints do not have mechanical braking systems but employ a dynamic braking system that actively shorts the motor leads to slow the motor until magnetic detents capture the rotor. The magnetic detents are sized to provide the appropriate holding torque to assure no slippage while IDA is powered off. Each joint has two position sensors, encoders on the joint input and potentiometers at the joint output. Each joint is equipped with two mechanical hardstops at the end of their range of travel.

The IDA end-effector consist of a five finger "claw" grapple hanging on an umbilical, a scoop and forearm mounted camera IDC (near the elbow joint). The IDA is used to point the IDC to take images of the surface, lander (selfie), lander elements, samples in the scoop, 360° panorama of the landing site and the workspace in which the arm can place the instruments. IDC images allow visual confirmation of deployment steps, as well as acquisition of stereo image pairs used to create a digital elevation model (DEM) and instrument deployment products of the workspace. IDC also provides engineering images of solar arrays, lander legs, payload deck, and instruments. The ICC is a single fish eye camera mounted underneath the lander deck (in a fixed location) and provides redundant context images of the workspace and horizon.

The scoop consists of a single chamber with a front blade and a secondary blade on the bottom side. The scoop's front and secondary blades can be used to excavate materials (digging or scraping) and collect materials excavated in the workspace. The scoop will enable scraping, trenching, and trench cave-in experiments to be conducted to infer mechanical properties of the martian soil at the landing site (section 7).

The grapple is a five finger "claw" and hangs by an umbilical at the IDA end-effector. The grapple is designed with five fingers to assure proper self-alignment and be position error tolerant while closing the grapple fingers around the spherical grapple hooks on SEIS, WTS and HP^3. The grapple fingers are opened by a single high output paraffin (HOP) actuator that slowly heats up, melts the wax that pushes a rod out to open the fingers. When the fingers are fully open, a limit contact switch trips, and turns the grapple HOP heater power off. As the grapple HOP cools down to ambient temperature, the grapple fingers slowly close passively without any actuation. The grapple umbilical provides the necessary compliance (unactuated additional 2 degrees of freedom for the 4 degrees of freedom IDA) for engaging and deploying the payloads on a tilted lander and uneven terrain. The grapple is stowed against the IDA forearm such that it does not obstruct the IDC field of view (FOV). However, when the grapple is unstowed it hangs in the FOV of the IDC such that the opening of grapple fingers and engagement of spherical grapple hooks on the payload can be imaged by the IDC.

During deployment the grapple is unstowed, hanging from the IDA end-effector by an umbilical cable. The IDA can position the grapple to capture the payload's spherical grapple hook, lift, and place SEIS, WTS and HP^3 on the martian surface. The grapple can be stowed using the IDA in a "ball-and-cup" maneuver to the grapple restraint mechanism on the IDA forearm.

The IDA motor controller consists of two printed-circuit boards located in the lower

Payload Electronics Box (PEB) and provides power conditioning, motor voltage control and drivers, heater drivers, joint encoder counting, and analog-to-digital conversion of potentiometer voltages, temperature sensor voltages, motor currents, and heater current. The PEB provides the interface to the Lander Command and Data Handling (C&DH) computer over a serial link. Firmware running on the IDA motor controller microprocessor provides for low-level motor command execution to move the joints to the specified positions, heater command execution, analog-to-digital calibration, and sensor monitoring.

2.2. Cameras

The Insight lander is equipped with two cameras (Maki et al. 2018): an Instrument Deployment Camera (IDC) mounted on the lander robotic arm and an Instrument Context Camera (ICC) hard-mounted beneath the lander deck (see Figure 1). The body-mounted ICC has a 124° x 124° FOV with a pixel scale of 2.1 mrad/pixel at the center of the image. The arm-mounted IDC has a 45° x 45° FOV, with a pixel scale of 0.82 mrad/pixel at the center of the image. The ICC is permanently pointed towards the deployment workspace, nominally located to the south of the lander, and the IDC pointing is controlled by the motion of the robotic arm. Stereo IDC images are acquired by moving the IDC between image pairs, and multi-image IDC panoramas can be acquired by pointing the camera around in a 360° fashion. A calibration target on the lander decks allows verification of the IDC radiometric performance, camera focus, and image scale.

Both of the Insight cameras are flight spare units inherited from the Mars Science Laboratory Mission (MSL) mission (Maki et al. 2012): the IDC is a spare MSL Navcam and the ICC is a spare MSL Hazcam, both of which are inherited designs from the Mars Exploration Rover (MER) cameras with the same names (Maki et al. 2003). The Insight project upgraded the MSL cameras from monochrome to color by replacing the MER and MSL monochrome detectors with

Bayer color filter array (CFA) detectors. The red, green, and blue (RGB) bandpasses are the same for both cameras and are centered at wavelengths of approximately 450, 550, and 620 nm, respectively. The upgraded cameras produce a raw 1024 x 1024 x12 bit Bayer pattern image. The Insight lander computer demosaics this raw image into a 3-channel RGB image, converts each channel to 8 bits, and compresses the RGB image to a user-specified quality level using JPEG (Joint Photographic Experts Group) lossy image compression. Typical JPEG compression quality values in use for the InSight mission include 85, 90, and 95, which approximately correspond to compressed bit rates of 1, 2, and 3 bits per pixel, respectively, although the exact relationship between compression quality and bit rate is scene-dependent. Upon receipt at Earth, the images are processed by the Multimission Image Processing Laboratory (MIPL) at JPL using software with heritage from previous Mars surface missions. Typical products generated by MIPL include mosaics, stereo disparity maps, 3-dimensional terrain meshes, slope maps, and instrument deployment products (section 4.7).

Although the primary requirements for the IDC and ICC are focused on the acquisition of data for the deployment and monitoring of the SEIS and HP^3 instruments on the Martian surface, images from the IDC and ICC will also be used by the Insight science team to characterize the geological properties of the terrain around the lander (section 5). Specific camera-related science investigations include the assessment of the landing site topography at centimeter scales and the characterization of the texture, roughness, size, color, and albedo of surface materials. Of particular importance to the geology science investigation is the ability to distinguish between gray basaltic material and bright red dust, something that is easily done with the color images (Maki et al., 1999). Images of the surface will also be used to characterize the spatial distribution of dust, soil, and rocks. Images of the sky will also be used to infer atmosphere dust optical depth and

distribution. All of the images acquired during the surface mission will be archived in the NASA Planetary Data System (PDS). For more information on the Insight cameras, see Maki et al. (2018).

2.3. HP^3

Although not a dedicated geotechnical instrument, the Heat Flow and Physical Properties Package (HP^3) will characterize the mechanical and thermophysical properties of the Martian regolith. HP^3 is comprised of a self-hammering probe called the HP^3 mole (also see Spohn et al. 2018), which will hammer itself into the Martian regolith to a target depth of 5 m (Figure 2). During the descent, HP^3 will stop at depth intervals of 50 cm to conduct thermal conductivity measurements, such that a depth profile of thermophysical properties will be obtained. In addition, the penetration speed of the probe depends on soil parameters including density, cohesion, and internal friction angle, and mole progress can be analyzed using numerical models (Hansen-Goos et al. 2014; Lichtenheldt et al. 2014; Lichtenheldt and Krömer 2016; Kömle et al. 2015; Poganski et al. 2017a) as well as laboratory experiments of mole-soil interaction (Marshall et al. 2017). Taken together, these efforts can then be used to constrain the mechanical properties of the Martian soil (see Section 7).

In addition to the thermal conductivity measurements carried out by the HP^3 mole, HP^3 uses an infrared radiometer to monitor the surface thermal environment (also see Spohn et al., 2018). Surface brightness temperatures in two fields of view facing north (opposite of the workspace) will be monitored continuously four times per day for the entire duration of the mission and hourly on planned sols, and each field of view will be observed using three bandpass filters with transmission in the 8-10 μm, 8-14 μm, and 15-19 μm wavelength range. A numerical model calculating surface and subsurface heat transfer (Kieffer 2013) will then be used to determine the

surface layer thermal inertia, which can be related to regolith grain size and/or cohesion (Presley and Christensen 1997a,b; Presley and Craddock 2006; Piqueux and Christensen, 2009). Stereo images of the two radiometer spots will allow separation of the rocky and fine components (Fergason et al. 2006; Putzig and Mellon 2007; Vasavada et al. 2017; Hamm et al. 2018).

The depth range probed by surface brightness temperature measurements depends on the thermal skin depth of the relevant surface temperature forcing, and thermal inertia determined from the diurnal temperature curve will be sensitive to the upper ~2 cm of Martian soil (e.g., Grott et al. 2007). However, one of the radiometer fields of view is expected to be partially covered by shadows from the solar panels in the morning and afternoon during some part of the year, including the deployment phase. Additionally, Phobos and Deimos will partially eclipse the sun for short periods of time at specific times. The temperature response to these shorter period fluctuations will be sensitive to material properties at shallower depths. Thus, near surface layering may also be detected using radiometer data. In addition, the continuous long-term observation of identical surface locations may furthermore allow for a direct measurement of the rate at which dust resettles at the landing site after being blown away by the retrorockets during landing (Daubar et al. 2015, also see Section 3.8).

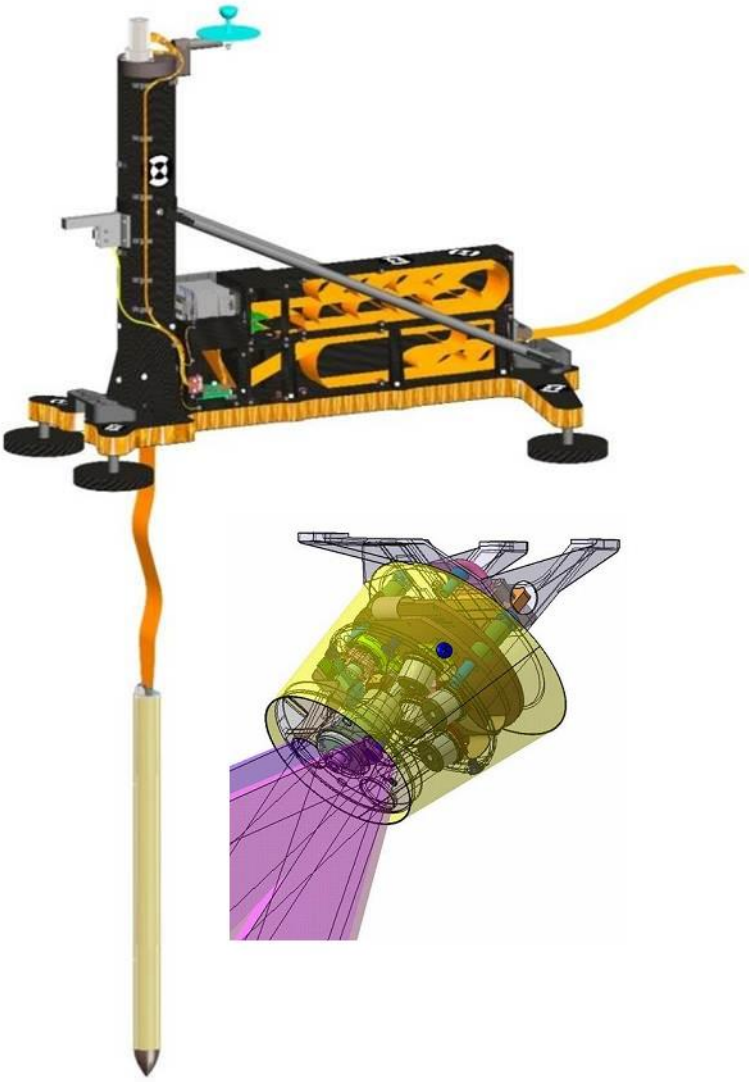

Figure 2: Schematics of the HP^3 instrument system showing the support system (black) that houses the mole during launch, cruise, and deployment with the mole (yellow) and science tether (orange) partially deployed. The radiometer, which is mounted underneath the InSight lander deck, is shown in the lower right of the image and the six thermopile sensors (gray) as well as the corresponding fields of view (pink) indicated.

2.4. SEIS

The SEIS experiment consists of a 3-axis very broad band (VBB) and a 3-axis short period (SP) seismometer (Lognonné et al. 2018). SEIS will be deployed on the surface, in direct contact with the soil through the three feet of the leveling system. The regolith's physical properties will influence SEIS measurements from resonances within the regolith layer, which should be

resolvable in SEIS recordings at the highest acquisition rate of 100 Hz, corresponding to a maximum resolvable frequency of 50 Hz. Based on estimated mean P- and S-wave velocities of the regolith of around 200 m s^{-1} and 125 m s^{-1}, respectively (Delage et al. 2017; Morgan et al. 2018), the seismic wavelengths are 2.5 to 4 m, similar to the expected regolith thickness. High-frequency waves recorded by SEIS VBB and SP will therefore be affected by the regolith structure. On the long-period end of the spectrum, the VBB outputs allow recording not only the ground velocity, but also the ground tilt with very high sensitivity. Both of these quantities can provide constraints on the physical properties of the shallow subsurface as described below.

The first constraint results from the ground tilt, which is expected to vary due to a number of sources, such as the thermal tilt of the subsurface (see Clinton et al. 2017, 2018 for time domain simulations), static loading of the lander in response to wind dynamic pressure (Murdoch et al. 2017a), and static loading caused by atmospheric pressure fluctuations due to planetary boundary layer activity (Murdoch et al. 2017b), including those associated with dust devils (Lorenz et al. 2015, Kenda et al. 2017). All of these sources generate significant seismic noise (Mimoun et al. 2017, section 4.5). These tilts can also be treated as signal and processed together with the pressure data to provide a profile of the subsurface shear modulus (section 7.4.1). To analyze small tilts at long periods (> 200 s), a correction for the larger signal due to the response of the VBBs to daily temperature variations is required. With an expected temperature sensitivity of the VBBs of about 10^{-5} m s^{-2} K^{-1} and daily temperature variations at the VBB of up to ±10 K in summer, time-varying signals equivalent to ±30 μrad of tilt will be recorded. Correcting this daily drift, a resolution of a few nrad in ground tilt in the 100-1000 s periods range may be achieved. The VBBs' gravity output might therefore also be used for active experiments with IDA, aiming to generate ground tilt in excess of these levels (section 7.4.2).

The second constraint (section 7.4.1), comes from the micro-seismic noise in the 1-30 Hz frequency band. This noise is mostly composed of high-frequency surface waves trapped in the upper layers of the regolith, due to the low seismic velocities of these layers (Delage et al. 2017; Knapmeyer-Endrun et al. 2017). Such surface waves generated by winds are commonly observed on Earth (e.g., Withers et al. 1996) and motivate the placement of seismometers on bedrock, away from low-velocity surface layers, and at depth in vaults or boreholes to avoid the disturbing influence of wind. High-frequency surface waves have also been observed on the Moon, where they are excited by thermal cracking (Larose et al. 2005; Tanimoto et al. 2008; Sens-Schönfelder and Larose 2008). These waves sound the ground with a maximum sensitivity at a depth of about 1/3 of their wavelength, and are mostly sensitive to the shear-wave velocity of the regolith. In addition, at frequencies higher than 20 Hz, differences in the placement of the six SP and VBB axes on the SEIS leveling system might enable a direct measurement of the phase velocities of these waves.

The third constraint is associated with the transfer function of the leveling system itself when deployed on the ground. As described in section 7.4.2, the horizontal transfer functions show resonances, and the frequencies at which these occur are related to the elastic properties and stiffness at the 3 contact points between the SEIS leveling system and the ground.

Finally, the last constraint will be derived from seismic monitoring of the signals generated by the penetration of the HP^3 mole (Kedar et al. 2017) and is discussed in section 7.5. HP^3 will act as an active source near SEIS, moving from the surface to a depth of up to 5 m. Specific signal processing will allow combining the SP signals in the 50-100 Hz frequency band with the VBB recordings at frequencies below 50 Hz to increase temporal resolution. This will enable the

detection of not only the direct P, S and surface waves, but also of possible reflections from the boundary between regolith and coarse ejecta and from scatterers within the regolith.

2.5. HP^3 – SEIS Hammering Investigation

The hammering of the HP^3 mole into the ground to measure a vertical thermal conductivity profile will generate seismic signals that provide a unique and unprecedented opportunity to investigate the shallow Martian subsurface using seismic-exploration techniques (Kedar et al. 2017). The analysis of the seismic signals will provide the opportunity to conduct the first-ever seismic study of the shallow (meters to possibly few tens of meters) martian subsurface. This HP^3-SEIS geotechnical experiment will reveal near-surface elastic properties that will be required to reduce travel-time and amplitude errors of globally propagating seismic waves as well as help test hypotheses of the shallow structure of the landing site.

The HP^3 hammering will consist of ~3 s cycles of hammer strikes driving the mole into the ground at <0.1 to 3 mm per stroke. The timing of each hammer strike can be deduced from the timing of the HP^3 built-in inclinometer used to track the location of the mole (Kedar et al. 2017). It is expected that the mole will require several thousand strikes to reach 3-5 m depth. Each strike will generate a seismic signal and so can be used in a similar manner to high-resolution active-seismic experiments conducted with sledgehammers for terrestrial engineering and environmental applications (e.g., Schmelzbach et al. 2005).

Seismic field data recorded with an HP^3 prototype by Kedar et al. (2017) as well as numerical simulations indicate that the seismic signals will be characterized by a dominant frequency of around 150 to 200 Hz. Because the objectives of SEIS are focused on the global martian structure (and thus long period waves) and due to bandwidth limitations, SEIS was designed to acquire seismic data with a maximum frequency of 50 Hz (Nyquist frequency for

100 samples per second, sps sampling). Consequently, the standard anti-alias filters would severely hamper a high-resolution seismic analysis of the HP^3 seismic signals. This can be avoided by taking advantage of the fact that two seismic instruments, the VBB and SP with independent data streams, will record the HP^3 hammering signals and that anti-alias filters implemented in the acquisition hardware can be changed during the mission. An optimized strategy that includes two separate recording settings has been designed to maximize the science return of this active-seismic experiment.

At the beginning of the HP^3 penetration when the most surface waves generated by the hammering are expected, all six axes of SEIS will be recorded at the maximum rate of 100 sps. Assuming a S-wave velocity of 125 m/s, the surface waves are expected to have a wavelength of around 2-2.5 m at 50 Hz. The distance between two feet of the LVL will therefore be about 10% of the wavelength. Because the three SP and three VBB axis on the LVL platform are placed at different distances from the SEIS center-of-gravity, the six axes of SEIS will allow the separation of the high-frequency ground rotation effects from acceleration and, therefore, estimation of the Rayleigh-wave phase velocity of the upper-most layers.

After this first penetration phase, the sampling of the seismic wavefield during the reminder of the HP^3 experiment will be improved by filters that will allow recording information up to 100 Hz. The sampling strategy is illustrated in Figure 3 which shows how the anti-alias filter of the VBB instrument will be kept the same as for the standard 100 sps recording with a passband between 0 and 50 Hz. The anti-alias filter of the SP instrument, however, will be replaced by a bandpass filter that passes frequencies between 50 and 100 Hz. Because the SP data sampling remains at 100 sps, the SP signals will be aliased and folded one time at the sampling frequency of 50 Hz onto the 0 to 50 Hz band. For reconstruction of the full 0 to 100 Hz bandwidth sampled

at 200 sps, the aliased SP signal will first be folded back onto its original band after which the non-overlapping (in frequency) VBB and SP recordings will be added together after corresponding instrument responses corrections.

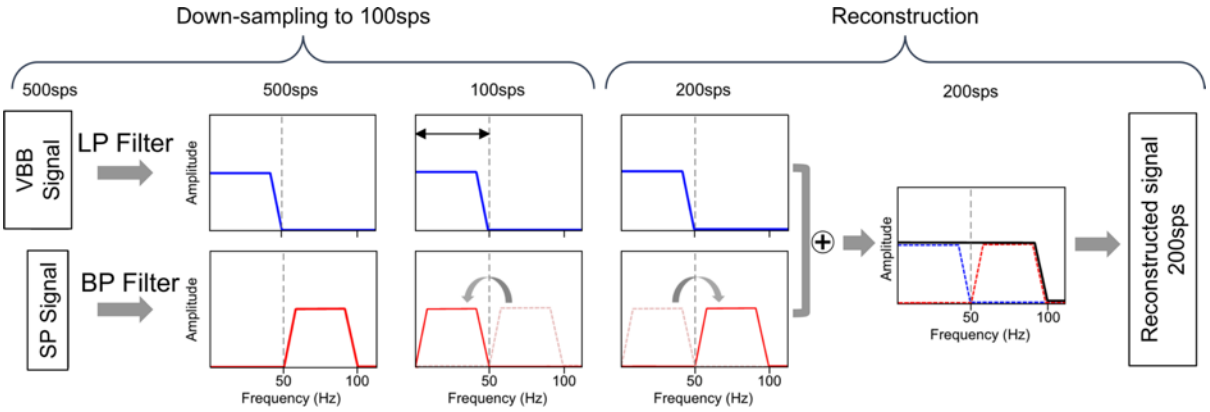

Figure 3. Illustration of the sampling strategy to record signals with frequencies up to 100 Hz (simulating a sampling rate of 200 sps from two separate 100 sps recordings). Whereas the VBB data will be acquired with the pre-set anti-alias filter (0–50 Hz low-pass filter; LP filter) when down-sampling the signals digitized at 500 sps to 100 sps, the SP data will be filtered with a 50–100 Hz bandpass filter (BP filter), which results in the SP data being aliased and folded one time at 50 Hz. For the reconstruction of the 0–100 Hz bandwidth (corresponding to 200 sps sampling), the aliased SP data are folded back before adding the VBB and SP data together.

2.6. Meteorology Instruments

InSight is equipped with a sophisticated package of meteorological instrumentation, comparable to prior landers, but exceeding their capabilities in several ways. The main goal for the meteorological instrumentation is to supply data that can be used to remove environmental contamination of the seismic data. However, the meteorological data will also prove particularly useful in understanding the eolian processes at the InSight landing site.

InSight's meteorological instrumentation is part of the Auxiliary Payload Sensor System (APSS), which includes a high precision pressure sensor, two booms to measure air temperature and wind, and a magnetometer. These are discussed in detail in Banfield et al. (2018). The pressure

sensor's sensitivity exceeds that of those on previous Mars landers by roughly a factor of 20 (e.g., Gomez-Elvira et al. 2012, Taylor et al. 2008, Seiff et al. 1997, Chamberlain et al. 1976), with a typical noise level of ~10 mPa on a particular measurement. While the primary use for this instrument is to remove the influence of passing atmospheric pressure variations from the seismic signals (e.g., Murdoch et al. 2017a,b), it will also prove useful in identifying nearby passage of dust devils (which may be confirmed by other sensors on InSight, e.g., Kenda et al., 2017, or from orbital images). It will be sampled continuously at 20 Hz. The pressure sensor itself is located within the lander, in the relative protection of the electronic box. However, it communicates with the ambient air pressure through tubing that opens to the outside air near the center of the lander deck, in a location that is the cruise and landing stowage point for the WTS. The early presence of the WTS is not expected to significantly modify the performance of the pressure sensor. Once the WTS is removed, the pressure inlet is exposed to the winds. The "quad-disc" structure is based on commercially available infrasound inlets and is designed to minimize any dynamic pressure effects from the wind (Nishiyama and Bedard 1991). The length and diameter of the inlet plumbing limit the response of the sensor to frequencies lower than about 5-10 Hz (Banfield et al. 2018).

The Temperature and Winds for InSight (TWINS) pair of booms will measure winds with similar technology as that from MSL (Gomez-Elvira et al. 2012) and that will fly on Mars 2020 Rover. The wind sensors, which are large finger-like probes with 3 wind sensing elements around their tips, are positioned at either end of the spacecraft deck, facing away from the center of the deck and out over the solar panels. This orientation is specifically chosen to have one boom facing upwind and away from the rest of the deck's obstructions at all times and wind azimuths. We expect to switch operating from one boom to the other to maintain the operational boom as the upwind one. The 3 sensing elements around the tip of each boom can be combined to yield the

three-dimensional wind impinging the boom. The booms can each resolve winds above 1 m/s to an accuracy of about 1 m/s with a response time of <~1 s. InSight will record winds from the TWINS booms at a nominal sampling rate of 0.5 Hz (Banfield et al., 2018).

The fact that both the pressure and TWINS sensors will be sampled continuously throughout the mission lifetime represents a unique capability that InSight offers surpassing previous landed Mars missions. Because there will be no gaps in the meteorological coverage (as there have been for all previous landers (e.g., Chamberlain et al. 1976; Seiff et al. 1997; Taylor et al. 2008; Gomez-Elvira et al. 2012), InSight will be able to conclusively quantify the peak winds occurring during an interval in which eolian change is observed.

2.7. RISE

RISE will use an X-band (8 GHz) radio transponder, power amplifier, and two medium-gain antennas on the lander in combination with tracking stations of the NASA Deep Space Network (DSN) to provide measurements of the Doppler shift of the InSight radio signal. Although RISE measurements are primarily aimed at determining properties of the martian interior (Folkner et al. 2018), a byproduct of this tracking is the determination of the location of the lander in inertial space to about five times better than any previous lander on Mars. Coupled with images to determine a cartographic position of the lander, will yield a superb tie between the cartographic and inertial frames, which is important for landing spacecraft and to aid in our understanding of the spatial distribution of features on Mars, which is a fundamental part of geology.

The measured Doppler shift is proportional to the rate of change of distance ρ between the DSN tracking station and the InSight lander (Yoder and Standish 1997):

$$\frac{\partial \rho}{\partial t} = \frac{\partial \rho_{EM}}{\partial t} + \frac{\partial \rho_{DSN}}{\partial t} - \frac{\partial}{\partial t}[R_z \sin \delta_E + R_s cos\ \delta_E \cos(\phi + \lambda - \alpha_E)] \quad (1)$$

where ρ_{EM} is the distance from the center of Earth to the center of Mars, ρ_{DSN} is the fraction of distance from the DSN tracking station to the center of Earth parallel to the Earth-Mars direction, R_z is the distance of the lander from the Martian equatorial plane, R_s is the distance of the lander from the Martian spin axis, λ is the longitude of the lander, ϕ is the rotation angle of Mars about the spin axis relative to the Mars equinox, and α_E and δ_E are the right ascension and declination of Earth as viewed from Mars. The right ascension and declination of Earth depend on the positions of Earth and Mars and on the direction of the martian spin axis in inertial space. The positions of Earth and Mars are well known from radio range measurements to Mars orbiters and from Very Long Baseline Interferometry (VLBI) measurements of Mars orbiters with respect to quasars that define the inertial reference frame (Folkner et al. 2014). The direction of the martian spin axis in inertial space is described by precession and nutation models. The precession rate has been accurately estimated from previous Mars missions (Yoder and Standish 1997; Folkner et al. 1997; Konopliv et al. 2006, 2011, 2016; Kuchynka et al. 2014). The precession has been useful with other measured properties of Mars to constrain models of the planet's interior (Dehant et al. 2009, 2011; Rivoldini et al. 2011). The main goal of RISE is to measure the nutation of the Martian spin axis for the first time to provide constraints on the core radius and density. RISE will measure changes in the rotation rate of Mars on seasonal time-scales and corresponding changes in the atmospheric angular momentum. RISE will also determine the coordinates of the InSight landing location as parameters necessary for the reduction of the radio Doppler measurements.

3. InSight Landing Site

3.1. Landing Site

Landing site selection for InSight has taken approximately five years and included defining the engineering requirements for safe landing and deploying the instruments, mapping those requirements onto Mars using remote sensing data, and evaluating the surface characteristics in targeted orbital observations (Golombek et al. 2017). Constraints on the landing site were derived from the entry, descent and landing scenario and design of the spacecraft and lander, which are similar to the PHX mission, and the InSight instruments. These constraints include: MOLA elevation below −2.5 km for sufficient atmosphere to slow the spacecraft during entry, descent and landing, latitude between 3°-5°N for solar-power and thermal management of the lander, reference ellipse of 130 km by 27 km for ballistic landing trajectory, radar-reflective surface for correct operation of the altimeter, thermal inertia >100–140 J m^{-2} K^{-1} $s^{-1/2}$ for a load-bearing surface without substantial fine-grained dust, rock abundance <10 % for low probability of impacting a rock that could damage the base of the lander, impede opening the solar panels, or restrict placement of the instruments on the surface, 1–5 m and 84 m scale slopes <15° for touchdown stability, leveling of SEIS and radar tracking of the surface, and a fragmented regolith 3–5 m thick for penetration of the HP^3 mole. Unlike all other Mars landing site selections (e.g., Golombek et al. 1997b, 2003a, 2012a), there were no science objectives that influenced landing site selection. All of these requirements are met by the selected landing ellipse in western Elysium Planitia located at ~4.5°N, ~135.9°E (Golombek et al. 2017) (Figure 4).

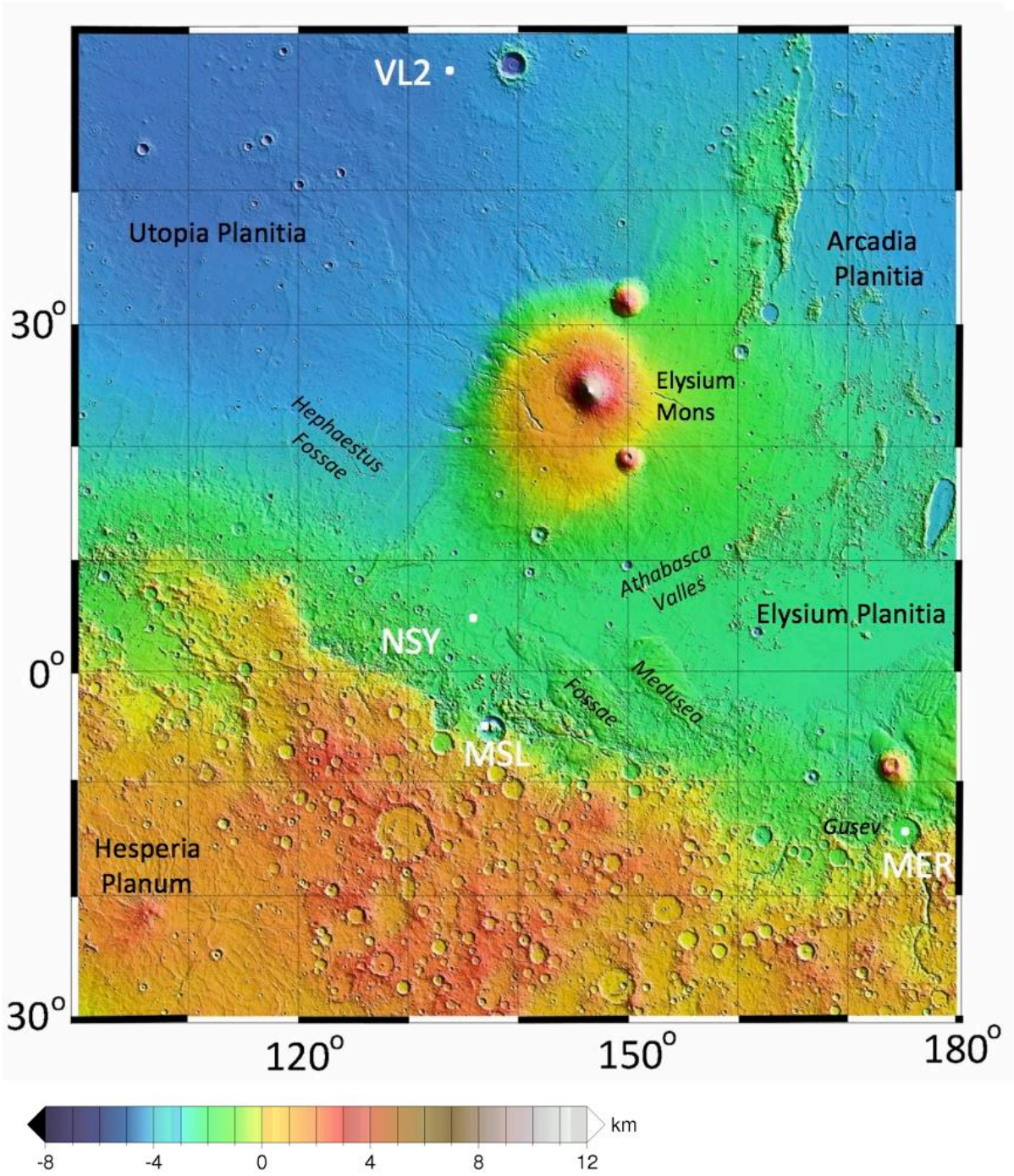

Figure 4. Topographic map of the region around the InSight landing site (NSY) showing major physiographic features, mentioned in the text, as well as the Viking Lander 2 (VL2), Mars Science Laboratory (MSL) Curiosity, and Mars Exploration Rover Spirit (MER) landing sites. Spirit landed in Gusev crater and Curiosity landed in Gale crater. The map is a portion of the MOLA topographic map of Mars with elevations with respect to the geoid (Smith et al. 2001).

3.2. Remote Sensing Properties

Analysis of remote sensing data during landing site evaluation and selection is described in detail in Golombek et al. (2017), to which the reader is referred for more extensive treatment, and provides substantial insight to the characteristics of the surface and subsurface properties. The bulk thermal inertia, or the resistance to a change in temperature of the upper 2–30 cm of the surface, and the albedo of the InSight landing site surface, are similar to the two Viking, MSL and Spirit landing sites. These sites all have moderate thermal inertia and intermediate to high albedo. The Thermal Emission Spectrometer (TES) thermal inertia (Mellon et al. 2000; Putzig and Mellon 2007) of the InSight landing site (~200 J m^{-2} K^{-1} $s^{-1/2}$) is consistent with a surface composed of cohesionless sand size particles or a mixture of slightly cohesive soils, some rocks and thermally thin coatings of dust (e.g., Golombek et al. 2008a). Thermal Emission Imaging System (THEMIS) thermal inertias of the landing site show high thermophysical homogeneity at the 100 m scale, with a median of ~180 J m^{-2} K^{-1} $s^{-1/2}$ (Golombek et al. 2017), corresponding to cohesionless ~170 μm, fine sand based on laboratory work and theoretical relationships (Presley and Christensen 1997a,c; Piqueux and Christensen 2011). The lack of significant seasonal variations in thermal inertia suggest the same material exists down to a few tens of centimeters depth. Although the spectral signature of atmospherically deposited dust is ubiquitous in the InSight landing region (i.e., relatively high dust cover index, Ruff and Christensen 2002), thermal inertia values are nowhere dominated by very fine material (at the 100 m scale), suggesting that dust forms an optically thick but thermally thin coating (hundreds of μm) on most surface materials in this region of Mars. Supporting this, orbital images show that most of the area is relatively high albedo with dark dust devil tracks, typical of areas with a thin layer of dust coating. Comparison with remote sensing properties of existing landing sites (Golombek et al. 2008a) suggests the soils at the InSight

landing site have bulk densities of ~1000–1600 kg m^{-3}, particle sizes of ~0.25-0.06 mm (medium to very fine sand), cohesions of less than a few kPa, and angle of internal friction of 30–40°. Albedo and dust cover index are similar to dusty and low-rock abundance portions of the Gusev cratered plains, which have been dominantly shaped by impact and eolian processes (Golombek et al. 2006a).

THEMIS thermal inertia is locally elevated around craters with rocky ejecta, and the thermal response has been modeled and correlated with the measured rock abundance (Golombek et al. 2017). Rock abundance at the landing site (Golombek et al. 2017) has been measured utilizing the same technique that has been used for previous landing site selections (Golombek et al. 2008b, 2012b): rock shadow segmentation, analysis, and modeling method using High Resolution Imaging Science Experiment (HiRISE) images. Rock abundance at the landing site ranges from no rocks detected in most of the smooth terrain, to 36% around rocky ejecta craters. The average rock abundance in the ellipse is 1.3%, and the area that exceeds 10% rock abundance is approximately 0.8 %. The rock abundance at the InSight landing site is among the lowest of previous landing sites (Golombek et al. 2017) and lies somewhere between that at the Phoenix landing site (2-4%) (Golombek et al. 2012b) and that at the Spirit landing site (~5%) (Golombek et al. 2005, 2006a).

Slopes at 1-5 m and 84 m length scales were evaluated in CTX and HiRISE digital elevation models or DEMs (Fergason et al. 2017) as well as tuned photoclinometry (Beyer 2017). The InSight landing site is among the smoothest surfaces investigated for landing spacecraft on Mars with < 0.5 % area exceeding 15° slope at 2 m length scale. Five meter root mean square (RMS) slopes are 2°-3° and are smoother than all other landing sites with the possible exception of the Opportunity landing site at Meridiani Planum or the PHX landing site in the northern plains

(Golombek et al. 2017). The surface is thus remarkably smooth and flat, except for common primary craters and secondary craters from the fresh, rayed crater Corinto, which is located ~600 km north-northeast of the landing site. These secondaries in DEMs and photoclinometry slope maps show very shallow depth/diameter ratios (~0.05) and interior slopes that rarely approach the 15° limit, indicating that they are not an engineering hazard and do not contribute significantly to the average slope distribution of the landing site.

3.3. Regional Geology

3.3.1. Geologic Setting

Western Elysium Planitia lies just north of the global dichotomy boundary between elevated heavily cratered southern highlands and lower-standing, less cratered, northern plains (Figure 4). The formation of the northern lowlands is the oldest geological event recognized on Mars, occurring in the pre-Noachian (Frey 2006), although younger tectonic and erosional processes have affected the dichotomy boundary since (McGill and Dimitriou 1990). The plains of western Elysium Planitia near the InSight ellipses are wedged between highlands to the south and west, a ridge of Medusae Fossae Formation to the east and southeast, Hesperian and Amazonian lavas from Elysium Mons to the north (Tanaka et al. 2014), and very young lavas from Cerberus Fossae and Athabasca Valles to the east (Vaucher et al. 2009).

The plains surface on which the InSight ellipses are located is mapped as an Early Hesperian transition unit (eHt) by Tanaka et al. (2014), which could be either sedimentary or volcanic. A volcanic interpretation of the plains is supported by: 1) the presence of rocks in the ejecta of fresh craters ~0.4–20 km diameter arguing for a strong competent layer ~4–200 m deep and weaker material above and beneath (e.g., Golombek et al. 2017; Warner et al. 2017; Catling

et al. 2011, 2012); 2) exposures of strong, jointed bedrock overlain by ~10 m of relatively fine-grained regolith in nearby Hephaestus Fossae in southern Utopia Planitia (Golombek et al. 2017; Warner et al. 2017); 3) mapping of volcanic flow fronts and vents in higher-resolution images described in the next section; and 4) the presence of wrinkle ridges, which have been interpreted to be fault-propagation folds, in which slip on thrust faults at depth are accommodated by asymmetric folding in strong, but weakly bonded layered material (such as basalt flows) near the surface (e.g., Mueller and Golombek 2004; Golombek and Phillips 2010).

Gravity data for Mars has a resolution of about 225 km (Konopliv et al. 2011, 2016). When analyzed with topography data in the spectral domain, some general constraints on the bulk crustal density can be obtained. Ojha et al. (2018) modeled the admittance, the ratio of gravity to topography in the spectral domain, in the region of the InSight landing site and found a relatively low density upper crust of ~2400 kg m^{-3}. Goossens et al. (2017) use the higher resolution topography data along with constraints from higher resolution GRAIL data for the moon to derive higher resolution gravity. They use this gravity field to estimate a global average bulk density of 2582±209 kg m^{-3}. This bulk density is similar to that found for the Moon of 2550±18 kg m^{-3} (Wieczorek et al. 2012). They also derive regional variations in crustal thickness in areas where the data is sufficiently robust. The Insight landing site is on the edge of one of these areas, with a bulk density ~2400 kg m^{-3}, in agreement with Ojha et al (2018). The exact depth range over which this density estimate applies is poorly constrained, but may be on the order of the upper 10 km, and is consistent with a regolith that is lower density at the surface and becomes denser with depth, as inferred for the Moon (Wieczorek et al. 2012) and expected for a region dominated by impact cratering (Section 3.5).

3.3.2. Regional Geology

The region around the InSight landing site was mapped from nadir visible images of Mars Express High Resolution Camera (HRSC) at 30 m/pixel combined with visible images acquired by Mars Reconnaissance Orbiter (MRO) Context Camera (CTX) at 6 m/pixel (Figure 5). The plains north of the landing site and including the northern and eastern edge of the ellipse is composed of lava flows, showing a large diversity of textures from smooth, planar surfaces suggesting low viscosity lava (Figure 5c, d and e) to rough platy surfaces likely related to more viscous flows forming lobate lava fronts (Figure 5g). Lobate lava flow fronts in the northern part of the InSight ellipse, indicate that flow was to the south from near or around Elysium Mons. The lava flow-dominated terrains have been deformed by ~5 km wide, ~300 m high, sinuous wrinkle ridges generally less than tens of km long, suggesting a tectonic shortening in competent, layered material (Watters 1988; Golombek et al. 1991; Schultz 2000; Mueller and Golombek 2004). We re-designate these volcanic plains as the Hv plains unit (Hesperian volcanic unit) (Figure 5b) based on direct observations of lava flow morphologies and the cumulative size frequency distribution of craters > 5 km in diameter. The N(5) value (cumulative number of craters with D>5 km per 10^6 km^2) for this unit is 86 to 200, which corresponds to the Early and Late Hesperian (Werner and Tanaka, 2011; Tanaka et al. 2014).

A more spatially-restricted crater count (~3.3 x 10^3 km^2) using CTX images was also conducted over the landing ellipse (Warner et al. 2017). This count included all craters with D > 200 m. The derived cumulative size-frequency distribution confirmed a Hesperian age from a fit to km-sized craters. However, a kink in the distribution exists for craters smaller than 2 km suggesting resurfacing of 100-m-scale craters in the Early Amazonian. A fit to the cumulative distribution at D < 1 km, including and excluding resurfacing corrections (Michael and Neukum

2010; Platz et al. 2013), provides model ages of 1.5 to 1.7 Ga. These data suggest that while the plains materials in the InSight landing region were largely emplaced during the Hesperian, that Amazonian-age resurfacing completely obliterated craters with maximum pristine depths of 200 m, assuming a depth to diameter ratio of ~0.2 for 1 km diameter craters (Pike 1974; Garvin et al. 2003; Watters et al. 2015). Furthermore, partially filled craters north of the landing ellipse indicate that the volcanic infill is ~300 m thick (Figure 5c and e).

The chronology data and evidence for resurfacing suggests that Early Amazonian-age volcanic activity, possibly associated with activity that emplaced unit AHv from Elysium, covered the InSight landing region with order of 100 meters of volcanic material. Many of the most pristine flow lobes and fronts that are observed within and north of the ellipse are likely from this younger volcanism. Northeast of the landing ellipse, these Hesperian to Early Amazonian-age flows and plains materials are superposed by very young lava flows (lAv) from central Elyisium Planitia, sourced from Cerberus Fossae to the northeast. These youngest flows have been dated between 274 Ma to 2 Ma (Vaucher et al. 2009) and are not deformed tectonically. This suggests that the wrinkle ridges observed in the plains material are inactive since ~300 Myr and may have formed during the Late Hesperian global peak in wrinkle ridge formation on Mars (e.g., Mangold et al. 2000; Golombek and Phillips 2010). These observations suggest a long period of volcanic activity in the region, spanning the Hesperian and into the Amazonian. This is also supported by lava flows covering sedimentary material of Aeolis Planum (Figure 5e) dated as Amazonian/Late Hesperian.

Within the majority of the landing ellipse and extending south to the planetary dichotomy, small, individual lava flow fronts are largely absent. However, the plains materials here exhibit wrinkle ridges, contain rocky ejecta craters, and embay remnant buttes of the southern highlands suggesting a similar lava flow origin. At the boundaries of these embayments, thick margins in the

plains material are evident, further supporting a lava plains origin. Volcanics close to the Martian dichotomy may have erupted from fissures as indicated by long rectilinear dikes (>100 km long) and volcanic vents (Figure 5g). Their spatial distribution is higher in the northern plains and they generally trend towards the north. The remnant highland buttes in this region are composed of sub-horizontal layers (Figure 5f), similar in structure to volcanic (effusive or pyroclastic) layers found in Valles Marineris (e.g., McEwen et al. 1999) and are likely remnants of the heavily cratered terrains of the southern hemisphere (here, mapped as HNt unit present in Nepenthes and Aeolis Mensae).

From a regional count (~1.3 x 10^5 km^2) of all craters > 2 km in diameter, Warner et al. (2017) obtained an Early Hesperian model age for the smooth plains unit extending from the final landing ellipse south to the planetary dichotomy. The N(2) and N(5) values of this count are 590 and 180, respectively. This is generally consistent with the maximum age of the Hv plains unit north of the landing region. However, smaller Early Amazonian-age flow lobes and fronts are absent here. We therefore also include the southern reaches of the landing region, south to the dichotomy, within the same Hv chronostratographic unit but surmise that Amazonian-age volcanism associated with Elysium did not extend this far south.

A geologic cross-section shows the spatial-temporal relationships between different units (Figure 5i). The InSight lander will land on a stack of Hesperian age lava flows, deformed by surficial wrinkle ridges, with diverse Noachian units beneath. If InSight lands further north or east of center of the landing zone, particularly within the ellipse that represents the orientation at the start of the launch window, InSight may land on or proximal to lobate lava flows from Early Amazonian volcanism.

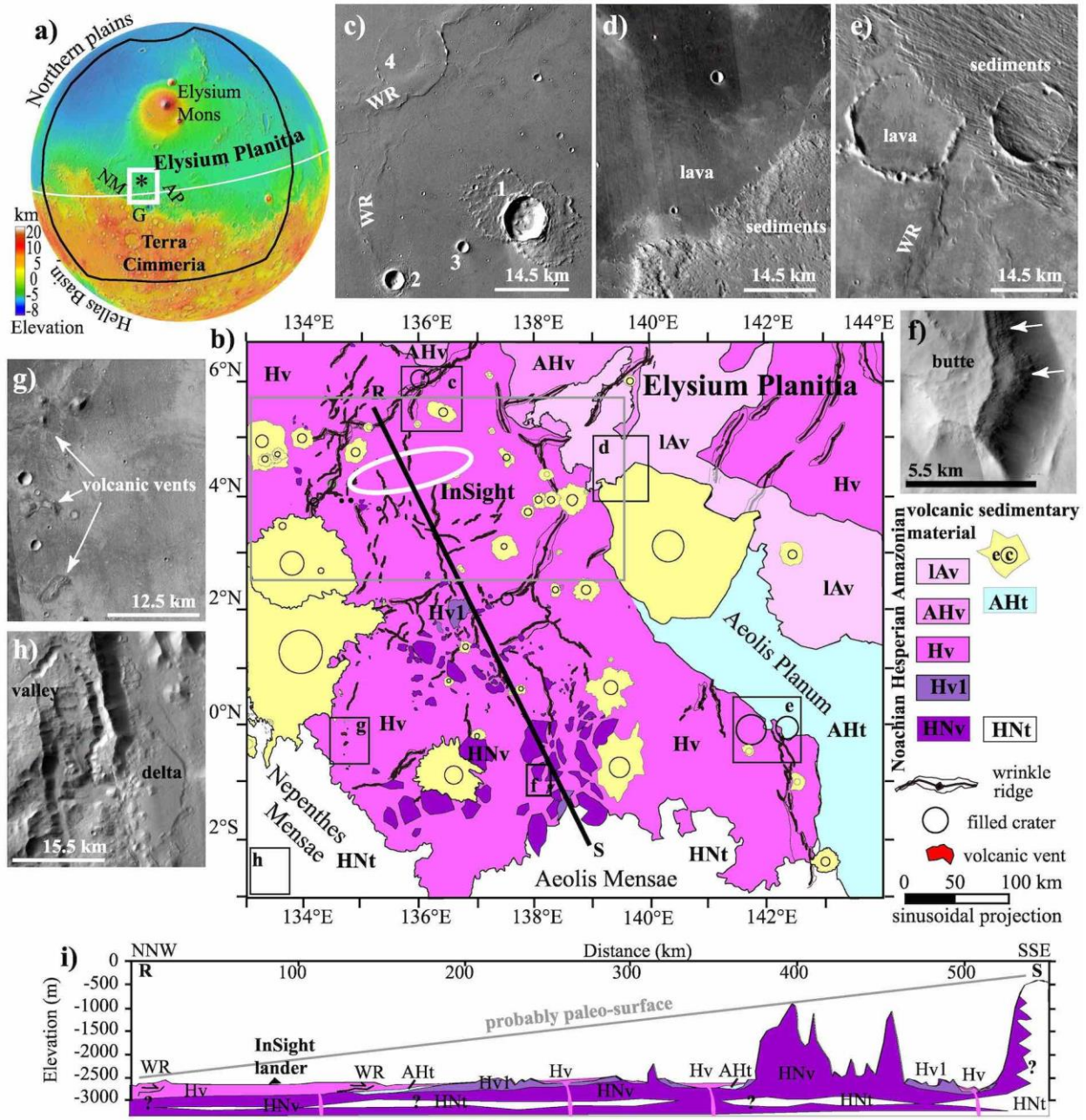

Figure 5. Regional geologic map and supporting information. a) MOLA topography centered on Elysium Planitia. Black box corresponds to location of Figure 4. White box corresponds to the location of the regional geologic map (viewed in b) in which elevation ranges from 0 m to -3000 m. The star symbol (*) marks the InSight landing site. NM: Nepenthes Mensae. AP: Aeolis Planum. G: Gale crater. White line is equator. b) Regional geologic map made from nadir visible HRSC and CTX images. Colors and symbols of geologic units refer to Tanaka's nomenclature (N: Noachian >3.7 Ga, H: Hesperian 3.7 to 3.1 Ga, and A: Amazonian <3.1 Ga, l: late period, v: volcanic unit; t: transitional unit corresponding to unit located along the Martian dichotomy). Elysium Planitia is covered by volcanic material (pink color) with ages from the end of Noachian (HNv in remnant buttes) to very Late Amazonian period (lAv in the NE part of Elysium Planitia

dated from 250 to 2.8 Ma (Vaucher et al. 2009). Nepenthes Mensae and Aeolis Mensae are mainly composed of old surficial sedimentary material (Noachian to Hesperian, NHt) or younger volcano-sedimentary material (AHt), belonging to Medusae Fossae Formation, respectively. Main geologic structures are plotted: fresh impact crater (c) and ejecta (e) in yellow, wrinkle ridges, filled or partially filled impact craters, and volcanic vent. White ellipse corresponds to the InSight landing site. Grey box corresponds to the location of Figure 6. Black boxes correspond to the location of insets: c) HRSC image showing lava flows filling crater (1, fresh impact crater with its ejecta; 2 and 3 ejecta partially to totally covered by lava flows, respectively; 4, impact crater embayed by lava flow), WR: wrinkle ridges; d to h: CTX images: d) Amazonian lava flows (lAv) covering the cratered sedimentary material of Aeolis Planum; e) Impact craters filled by lava flows (left) and the sedimentary material of Aeolis Planum (right); f) Remnant 1300 m high butte showing dark layers probably composed of volcanic material; g) Volcanic vents in southern part of western Elysium Planitia near Nepenthes Mensae; h) Example of geologic structures found in Nepenthes and Aeolis Mensae: large impact craters (Gale) incised by valleys ending by delta fans. i) Geologic cross-section located along RS line on regional geologic map: stack of volcanic materials interbedded by sedimentary materials.

3.3.3. Volcanic Landforms of the Landing Site

The local geology of the landing ellipse and area immediately around it was mapped at a scale of 1:50,000 on HRSC and CTX images (Figure 6). Most of the surface within the final ellipse corresponds to the Early Amazonian to Hesperian volcanic unit in section 3.3 and the Ridged and Smooth Terrain units (section 3.4). Observations of flow fronts and lava inflation plateaus also strongly support a volcanic origin (Figures 7a-c). The plan-view orientation of the flow fronts is indicative of an emplacement from the north, i.e. from Elysium Mons or thereabouts. Flat-topped plateau-like areas with rounded margins (Figures 7d-e) are morphologically similar to lava inflation plateaus on Earth (Walker 1991; Hon et al. 1994), which have also been identified on Mars before (e.g., Bleacher et al. 2017; Golombek et al. 2006a). Lava inflation is most common in relatively fluid pahoehoe lavas, so it is expected that at least parts of the volcanic stratigraphy consists of thin (~meter-scale) pahoehoe sheet flows, although we did not observe any diagnostic volcanic surface patterns (Gregg 2017) on the flows shown in Figure 7 at HiRISE scale. Platy-like flow facies (Figure 7f), which form from differential flow velocities and related shear movements

are also indicative of lavas with relatively low viscosity. Further evidence for a volcanic origin of the smooth plains comes from the observations of closely spaced contractional ridges parallel to flow lobe margins, called "festoon ridges" by Theilig and Greeley (1983). We also map the wrinkle ridges in the landing site area and noted some cases where wrinkle ridges seem to trace the rims of buried impact craters (Figure 8). As these craters are numerous and large (Figure 8d), the basement beneath the lava flows is likely to be ancient Noachian crustal materials.

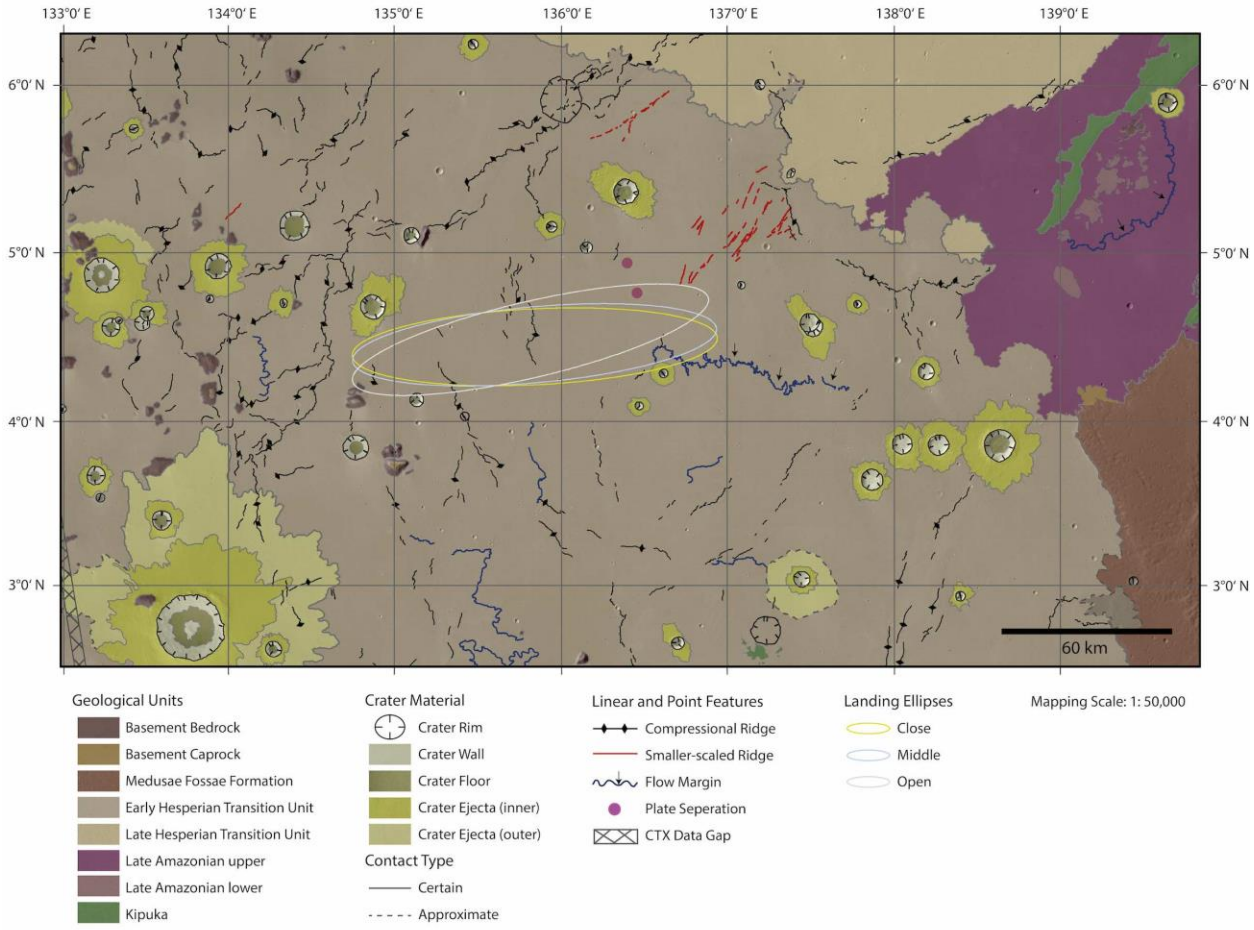

Figure 6. Geological context map of the InSight landing site region overlain on an HRSC-mosaic (with a pixel size of 25 m). CTX-images (6 m/pixel) were used to generate the geologic map at a digitizing scale of 1:50,000. White, blue and yellow are 130 km by 27 km ellipses for the open, middle, and close of the launch period.

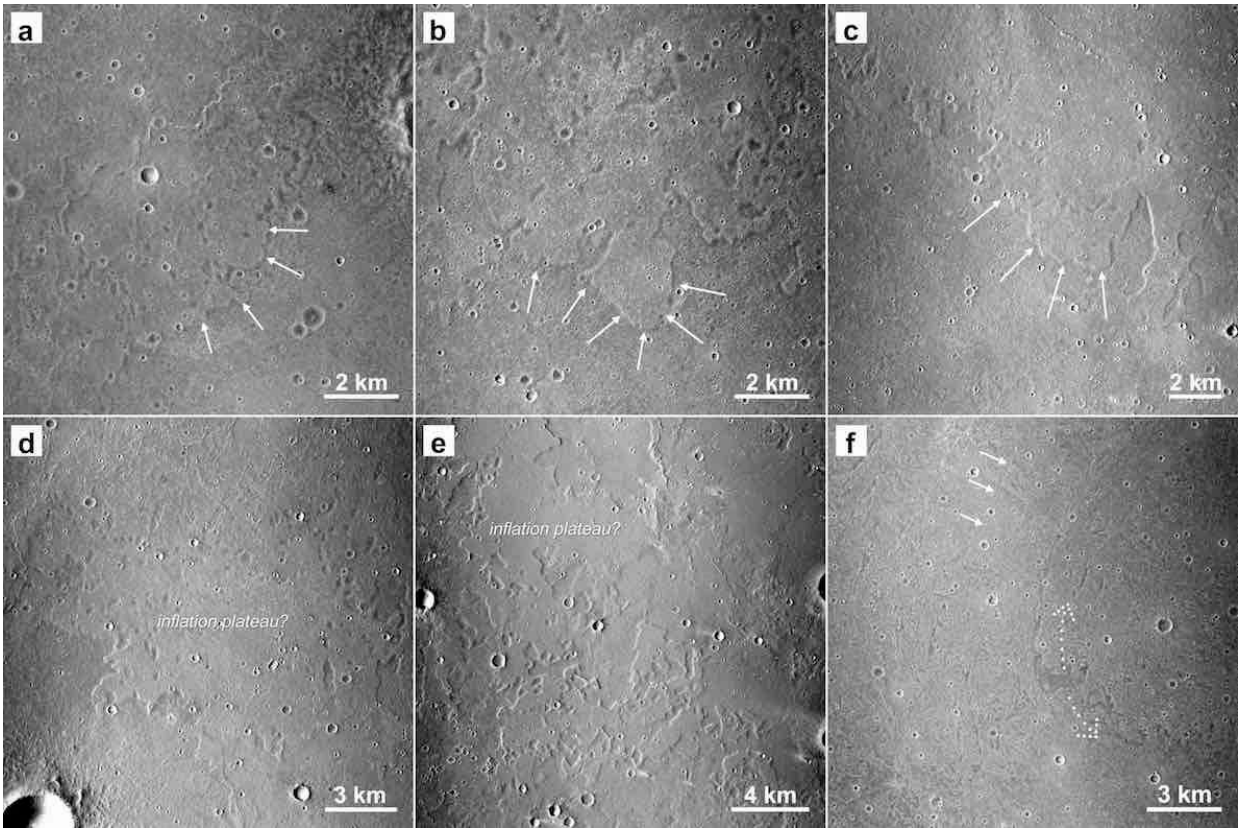

Figure 7. Lava flow morphology at the InSight landing site. (a-c) Lobate flow fronts (arrows). The low aspect ratio of the flow fronts suggests an emplacement as sheet flows (a: CTX D14_032660_1843; image center at ~4.22°N, 136.5°E; b: D15_033227_1841, ~4.37°N, 136.95°E; c: D04_028757_1855, 4.23°N, 137.3°E). (d, e) Plateau-like flow units with flat surfaces, suggestive of lava inflation (d: D04_028968_1853, 4.42°N, 136.72°E; e: D04_028757_1855, 6.29°N, 137.1°E). (f) Platy flows, with shear fractures (white arrows) and relative motion indicated by dotted arrow (D14_032660_1843, 4.79°N, 136.44°E). North is up for all images.

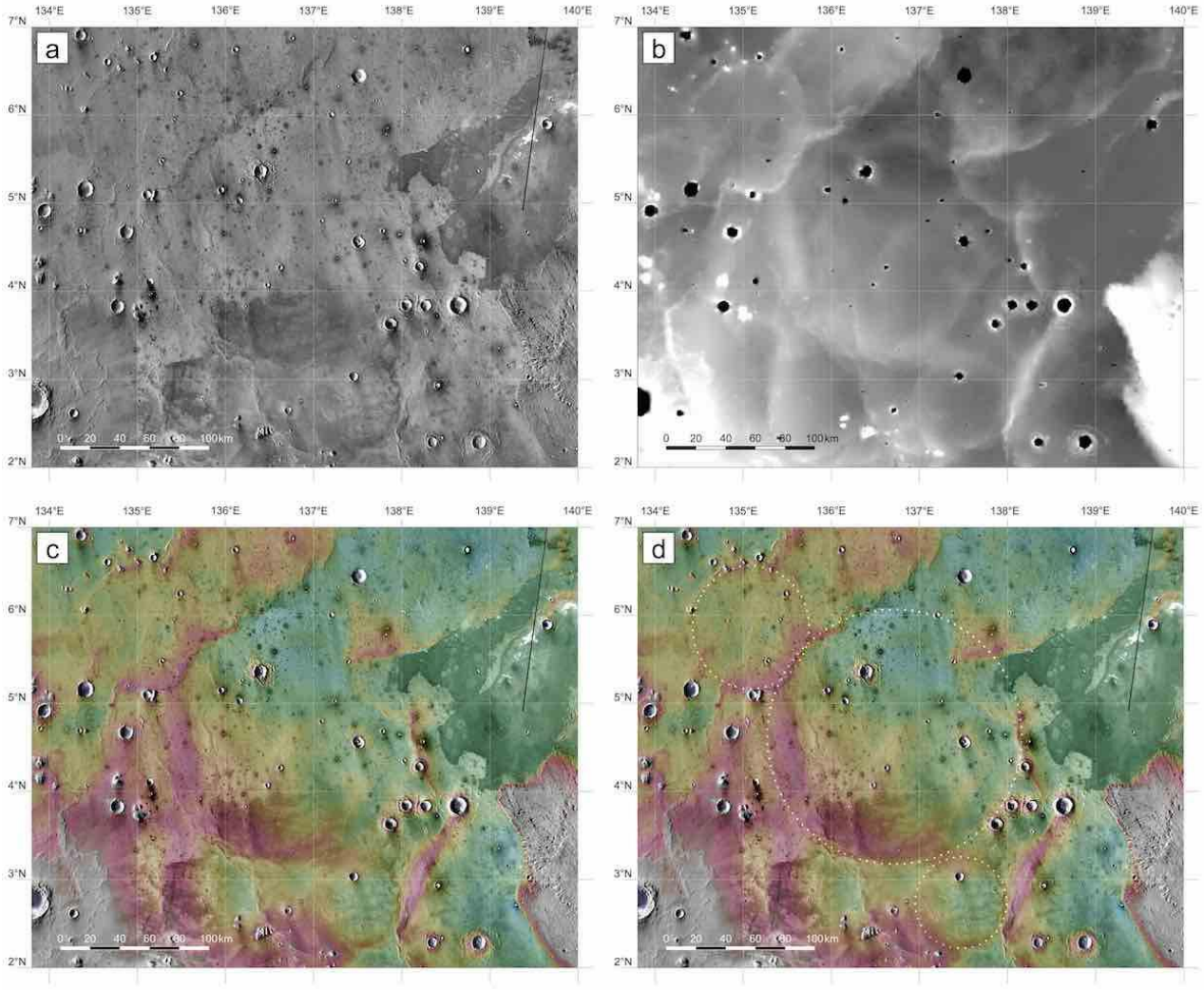

Figure 8. Thermal and topographic maps of the InSight landing site region showing evidence for buried craters. (a) THEMIS-IR daytime image mosaic (Edwards et al. 2011). Note the dark impact craters with relatively cool daytime temperatures indicating they have higher thermal inertia. These correspond to ejected rocks in rocky ejecta craters. Note large craters are not rocky indicating they are ejecting weak material from below the 200-300 m thick lava flows. Dark unit to the east is made of very young volcanics from Athabasca Valles. (b) MOLA DEM emphasizing subtle topography of the volcanic plains. (c) Color-coded MOLA DEM overlaid on THEMIS-IR daytime image mosaic. (d) Same as c, with possible buried impact craters marked by dotted circles. Note how wrinkle ridges trace the rims of the craters.

3.4. Terrains in the Landing Ellipse

The surficial characteristics of the landing ellipse were evaluated and mapped during landing site selection (Golombek et al. 2017) using co-registered MOLA, THEMIS (100 m/pixel),

CTX (6 m/pixel), and HiRISE imagery (25 cm/pixel). A final terrain map (Figure 9) was produced at a scale of 1:40,000 using a complete CTX mosaic, with confirmation of terrain types from HiRISE. The terrains were defined by their topographic characteristics, thermal properties (relative daytime and nighttime temperatures), albedo, rock abundance, and geomorphology. The terrain map is distinct from geologic maps that identify contacts between distinct chronostratigraphic units (section 3.3). Rather, the terrain map displays surficial characteristics and variations that are relevant for landing and surface operations.

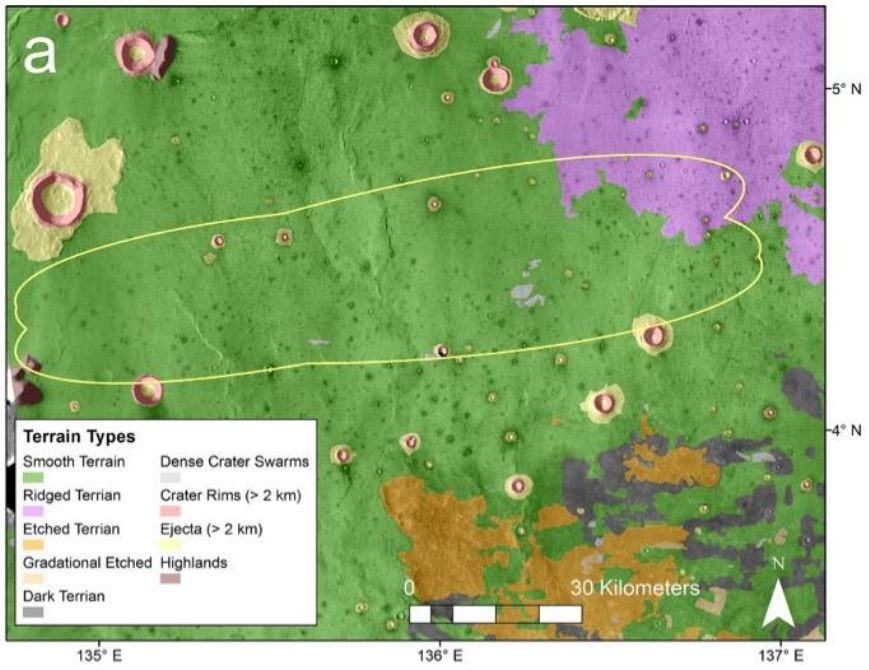

Figure 9: Terrain map of the InSight landing region. The open, middle, and close orientations of the final landing ellipse (they rotate clockwise with launch date) were merged to display the possible range of landforms and surface terrains within the landing region. The dominant terrain types in the landing site include Smooth Terrain and Ridged Terrain. Crater Rims and Ejecta for craters > 2 km in diameter and Dense Crater Swarms (secondary crater clusters) are also present. Further information on the terrains can be found in Golombek et al. (2017)

Visible light images reveal a constant moderate albedo, low relief and low regional and local slopes across the ellipse. THEMIS daytime and nighttime infrared mosaics (Christensen et al. 2004) indicate that the surficial material in the ellipse is thermally uniform (Figure 8a) and is composed of poorly consolidated sand that lacks rocks, with limited dust cover (section 3.2). Variation in the thermal characteristics only occurs proximal to impact craters, where higher thermal inertia materials are indicated. CTX and HiRISE imagery reveal that abundant >meter-sized rocks correspond with this high thermal inertia signature around craters (Figure 10). The rocks extend approximately 1 crater diameter (1D) from the rims of all fresh craters larger than 200 m but less than 2 km in diameter, as well as surrounding some ≤ 200 m diameter craters. Eolian bedforms are also observed in the ejecta of fresh craters, trapped against rocks and crater rims. Bedforms and rocks are largely absent in the inter-crater regions, implying that rock and sand production, as well as recent sand mobilization and deposition, are limited to impact-proximal regions (Golombek et al. 2017; Sweeney et al. 2018). Dust devil tracks are ubiquitous across the region and suggest a dominant northwest to southeast wind direction (Figure 11). The prevailing winds result in preferential bedform accumulation on the northwest exterior of crater rims and the formation of northeast-southwest trending bedforms on the floors of craters (Figure 10).

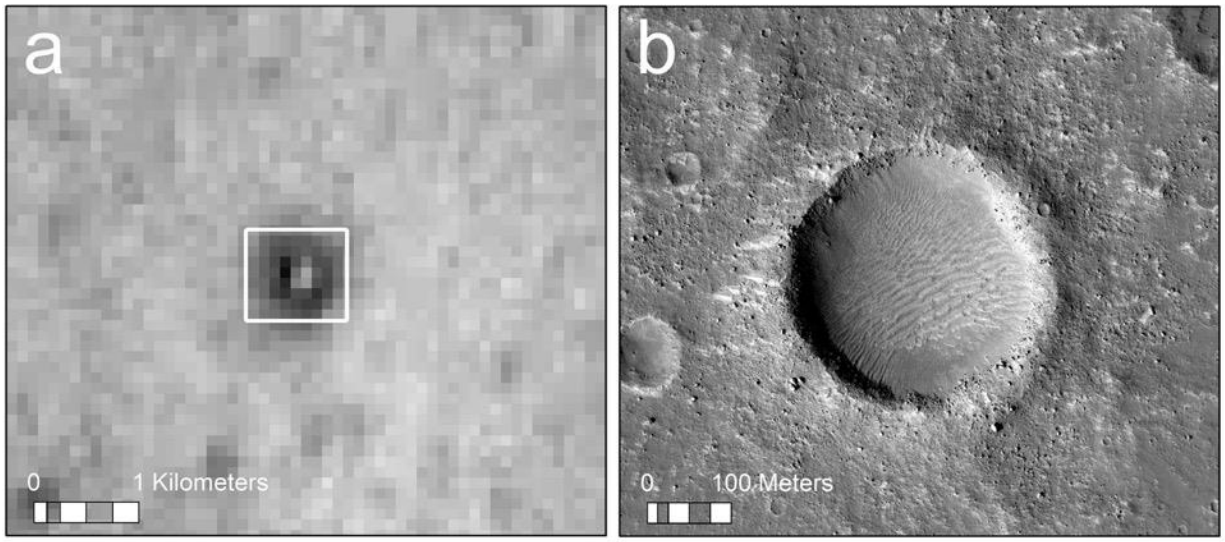

Figure 10: Example Rocky Ejecta Crater (REC) on Smooth Terrain in the landing ellipse. The daytime THEMIS image (a) displays a halo of relatively cooler temperatures, indicating a higher thermal inertia. The HiRISE image of the white box (b) shows that the higher thermal inertia halo correlates with abundant rocks within the ejecta blanket of the crater. Meter to 10-meter-size rocks are identified by their shadows. Relatively bright eolian bedforms are present within the ejecta, trapped against the northwest rim of the crater, and on the floor of the crater.

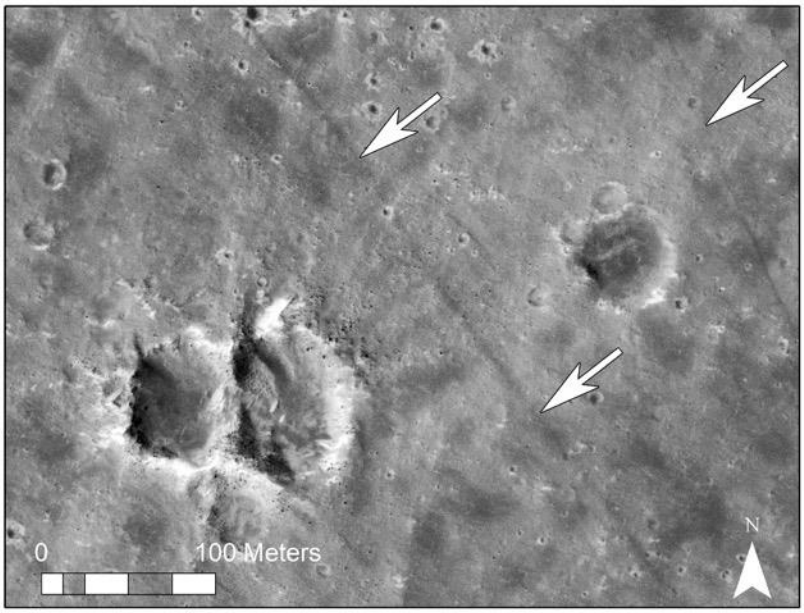

Figure 11: HiRISE image displaying NW-SE dust devil tracks (white arrows) in the laning ellipse. Dust devils expose lower albedo surface material by removing relatively higher-albedo dust. The dust devil orientation and bedform accumulation pattern against the rims of craters suggest wind from the northwest.

Gentle topography, overall uniformity in thermal/albedo characteristics, and low rock abundance define the Smooth Terrain surficial unit (Figure 12). Smooth Terrain dominates the landing site and is regionally-extensive, occurring across western Elysium Planitia (Golombek et al. 2017). Coupled with observations of wrinkle ridges and rocky ejecta craters, the Smooth Terrain surficial characteristics are consistent with a regolith that overlies a more competent bedrock unit. This is in agreement with the lava plains interpretation for the Early Hesperian transition unit (eHt) that extends across the ellipse (section 3.3). Associated terrain types, identified during the landing site downselection mapping phase, further imply that the Smooth Terrain has a regolith. The Etched and Gradational Etched terrain units occur outside of the ellipse (Figure 9) and likely represent regions where the upper regolith was either completely or partially stripped of sand-size grains by eolian activity (Golombek et al. 2017). These units occur in localized 1 to 10-km-scale pockets surrounded by Smooth Terrain and are noted for their comparatively rougher topography, higher rock abundance, and higher thermal inertia. The higher rock abundance may represent a lag that was left behind after the sand was removed.

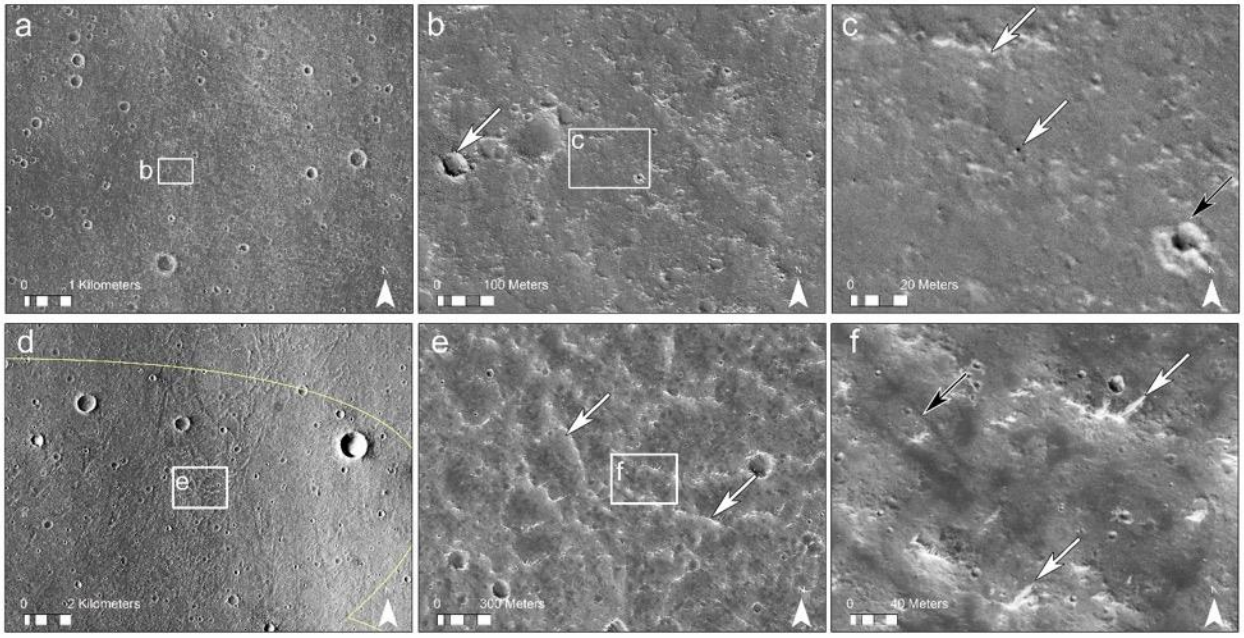

Figure 12: Terrain samples from the InSight landing ellipse. (a) CTX image showing a typical example of Smooth Terrain. (b) HiRISE image sample of Smooth Terrain. The white arrow points to a relatively fresh, 50 m diameter REC. (c) Zoomed in portion of the Smooth Terrain showing one rock and bright bedforms (white arrows). Rocks and bedforms are rare on the intercrater plains. The black arrow is a secondary crater from Corinto with characteristic bright ejecta. (d) CTX image displaying the Ridged Terrain in the northeast corner of the ellipse (open orientation). Ridged terrain is identified by lobate landforms and sub-parallel ridges that are oriented parallel to the lobate margin. (e) HiRISE image of the ridged terrain. White arrows point to the crests of the sub-parallel ridges. These ridges are interpreted to represent compression ridges on the surfaces of lava flows. (f) The ridges are elevated landforms that trap eolian bedforms (white arrows). Dust devil tracks are also common in the Ridged Terrain (black arrow).

The open orientation of the landing ellipse also incorporates a localized terrain unit along its northeast margin called Ridged Terrain (Figure 9). Ridged Terrain is defined by degraded lobate landforms that exhibit characteristic lava flow morphology (Figure 12). The orientation of the margins indicate flow from the northeast, consistent with a volcanic source southwest of Elysium Mons. The surface of the lobate features exhibit meter-scale (in width and relief) sub-parallel ridges that are aligned perpendicular to the inferred flow direction and may be relic compressional ridges that formed in the lava crust during flow. The local and regional slopes, thermal properties, albedo, and rock abundance of the Ridged Terrain are similar to the Smooth Terrain, implying

some regolith cover. However, the preservation of lobate margins and surface ridges suggest that the ridged terrain is younger Amazonian lava plains from Elysium Mons or thereabouts (see also section 3.3). This is consistent with the crater chronology that suggests relatively thin (~ 200 m) Early Amazonian resurfacing within the ellipse.

3.5. Rocky Ejecta Craters and Regolith Thickness

The presence of rocky ejecta craters (RECs) in the landing ellipse indicate that a more competent rock-bearing unit occurs at depth. Mapping of all RECs in the landing ellipse using HiRISE images revealed that all craters between 200 m and 2 km in diameter exhibit meter-size rocks in their ejecta (Warner et al. 2017). However, most craters below 50 m in diameter, including fresh craters and young (< 2 Mya) secondaries from Corinto crater (Preblich et al. 2007; Bloom et al., 2014; Hundal et al. 2017) completely lack rocks. This suggests that smaller impacts did not excavate deep enough to access the rocky unit. The cumulative size-frequency distribution (SFD) of RECs in the ellipse confirms this observation and demonstrates a roll-off in the frequency of RECs at diameters ≤ 200 m and a complete lack of RECs below 50 m (Warner et al. 2017). These observations support the hypothesis that the landing site is capped by a less competent, loosely-consolidated regolith, consistent with the terrain mapping.

Using established depth of excavation relationships (including the d = 0.084D relationship from Melosh 1989), and the minimum cut-off diameters for rocky ejecta around craters, Warner et al. (2017) determined that the landing ellipse is covered by a 3 to 17 m thick regolith. Concentric craters, identified in HiRISE images, further indicate a two-layer, near-surface stratigraphy that is consistent with a weaker regolith layer overlying competent rock (Figure 13). The inner concentric craters form within the larger outer crater at depths between 2 and 5 m, measured relative to the surrounding plains.

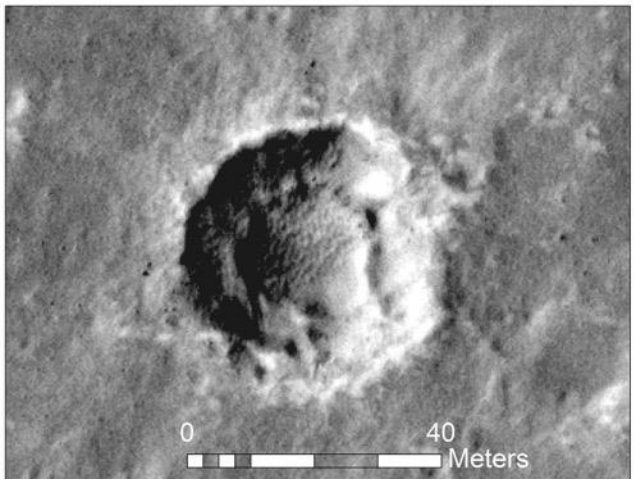

a

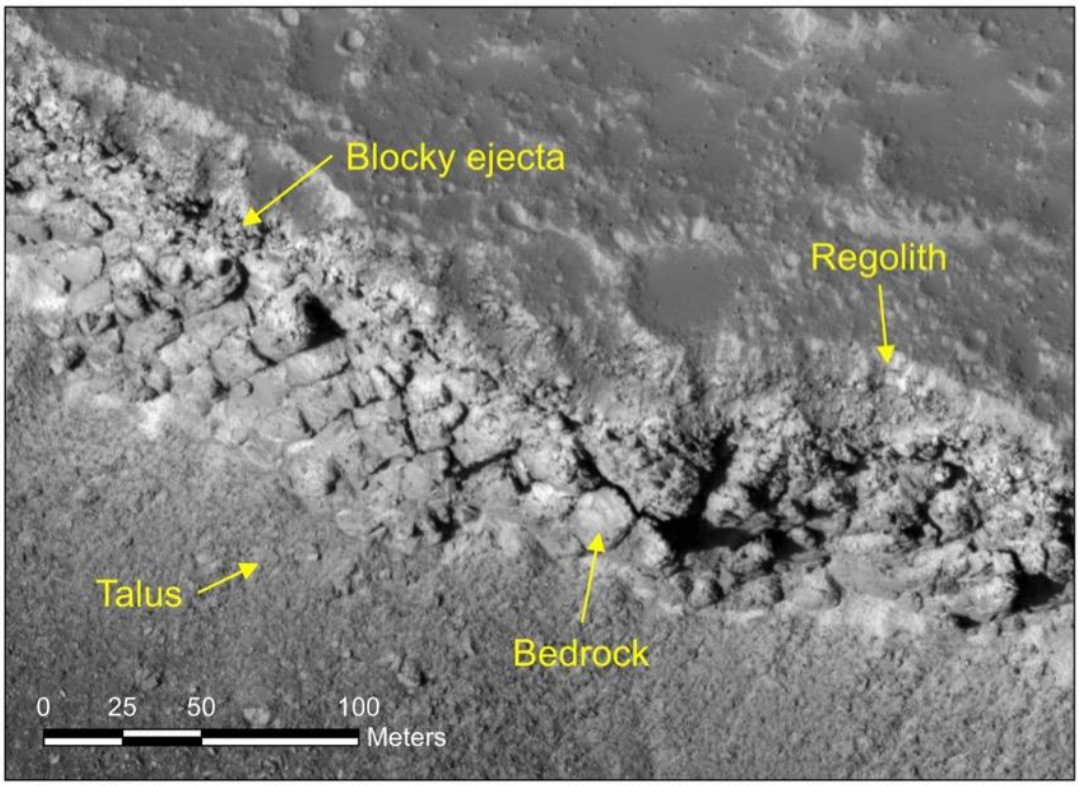

b

Figure 13. (a) Concentric (nested) crater (HiRISE images) within the InSight landing ellipse. Most concentric craters are <100 m in diameter and are typically less than <50 m in diameter. This 40 m example exhibits low rock abundance in its continuous ejecta. The inner nested crater and the overall lack of rocks within the ejecta support the presence of a two-layer stratigraphy of a weak regolith that overlies a more competent rocky unit. (b) A portion of the exposed steep scarp of Hephaestus Fossae in southern Utopia Planitia at 21.9°N, 122.0°E showing ~10 m thick, fine

grained regolith overlying blocky ejecta that grades into strong, jointed bedrock.

A preliminary REC density distribution map, from a set of 16 HiRISE images, indicated the possibility for spatial variations in regolith thickness across the landing ellipse (Warner et al. 2017). A higher density grouping of RECs, associated only with the order of ≤100-m-scale rocky crater population, was found to correlate with the location of a north-south trending wrinkle ridge that bisects the middle of the landing ellipse. This could be due to a locally-thin regolith along the ridge. Excluding the presence of unique, local-scale (order of 10-100 km^2) chronostratigraphic units in the landing site, other possibilities for the spatial variations include random and non-random variations in the cratering pattern of primaries (Platz et al. 2013; Warner et al. 2015) and the influence of non-random secondary clusters. A new REC map (diameter > 30 m), constructed using all HiRISE images that cover the landing ellipse, confirms that the higher density grouping of fresh (Class 1 -3; see next section and Warner et al. 2017), small rocky craters correlates almost exclusively to the strike of the ridge. Although obvious secondary clusters and chains (noted for their alignment with other clusters and their uniform state of preservation), including those derived from Corinto crater to the north, were removed from the density analysis, it remains possible that the high density of RECs is a function of non-random clustering in the crater population. To evaluate this possibility, all similarly fresh > 30 m diameter non-rocky craters were also mapped using a set of 15 HiRISE images (Figure 14). The non-rocky count targeted locations of Smooth and Ridged Terrain in the eastern and western regions of the ellipse as well as the Smooth Terrain at the center of the ellipse, correspond with the ridge. The density of RECs was normalized to account for possible spatial clustering by comparing the total number of rocky craters within 5 km grids to the total number of all fresh craters present (rocky + non-rocky) in that same grid. The data indicate that there is higher percentage of RECs relative to the total number of craters along

the strike of the wrinkle ridge. There, 60% to 90% of all fresh craters that are > 30 m in diameter exhibit rocks in their ejecta. However, the relative percentage of rocky craters to total craters generally decreases away from the ridge near the eastern and western edges of the ellipse. At those locations between 10% and 40% of all craters in this size range exhibit rocks in their ejecta. This suggests that the regolith is locally thin proximal to the ridge. At these locations, the regolith may be < 3 m thick along the crest and immediate flanks of the wrinkle ridge. A second, smaller ridge extends into the southwestern part of the ellipse. Here, a similar trend between rocky and non-rocky craters is identified suggesting the possibility of a locally thin regolith.

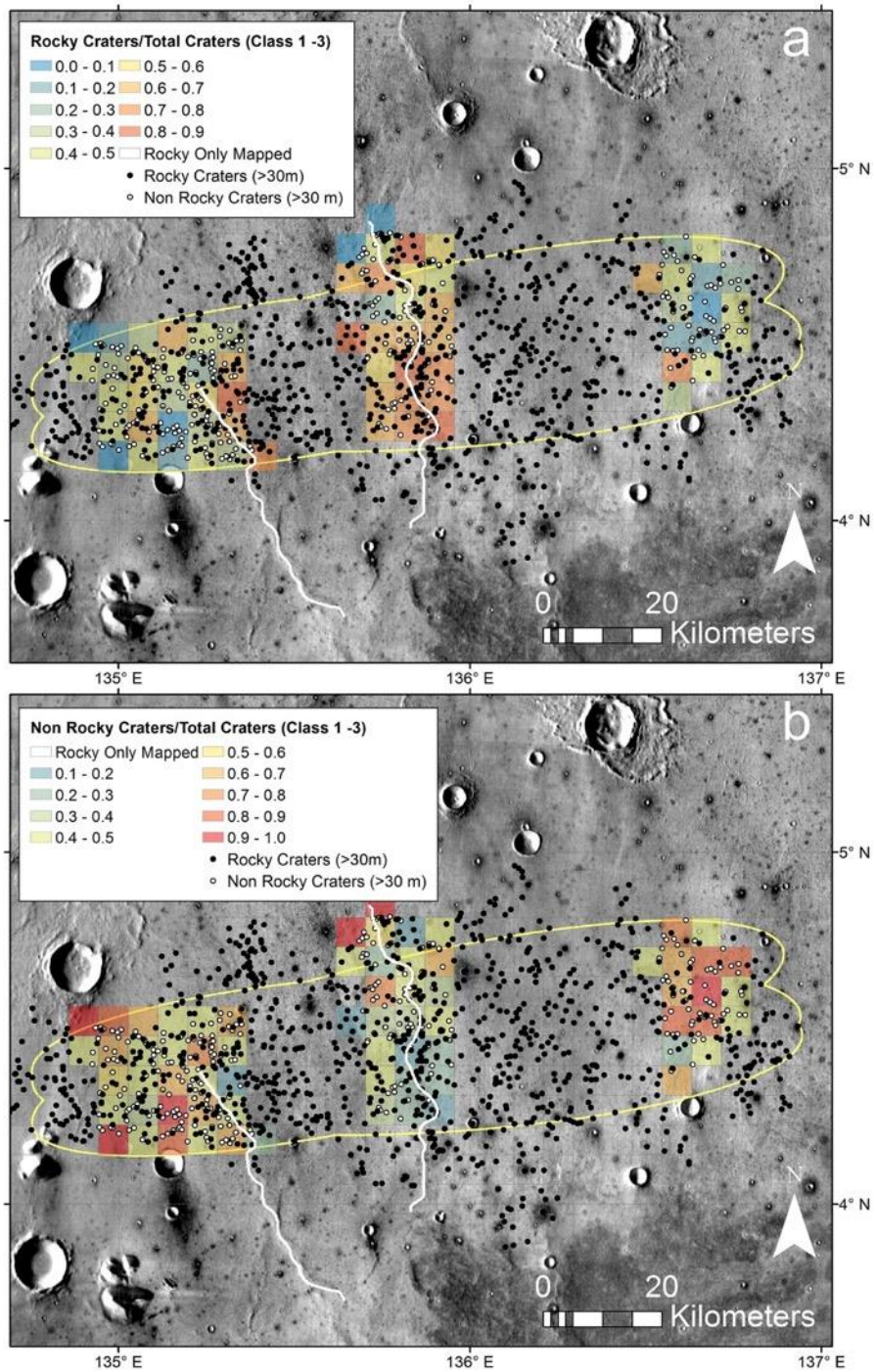

Figure 14: Map of the distribution of fresh, > 30 m diameter RECs and fresh non-rocky ejecta craters within the InSight landing site. Only the freshest Class 1 to 3 craters are included here (see Warner et al. 2017 for classification description). (a) A grid (5-km-spacing) showing the ratio of fresh RECs relative to the total number of fresh craters. The white lines indicate the center-line of wrinkle ridges. An overall higher ratio of rocky craters occurs along the ridges. A lower ratio of rocky craters relative to the total occurs further from the ridge. (b) A grid (5-km-spacing) showing the ratio of fresh non-rocky craters to the total. The wrinkle ridges correspond with an overall lower ratio of > 30 m diameter, fresh non-rocky craters indicating a thinner regolith.

3.6. Surface Processes

Craters in the InSight landing site degrade over time, like all martian craters do, through an overall reduction in rim height, lowering of the interior and exterior rim slope, and infill by eolian materials. Golombek et al. (2017) and Warner et al. (2017) defined a 1 to 5 morphologic classification system for the RECs, relating crater interior, rim, and ejecta characteristics (e.g., rock abundance) to relative age. Class 1 craters represent the most pristine, youngest RECs, while Class 5 represent the oldest craters to still preserve rocks in their ejecta. Using the size-frequency distribution of different class groupings, Warner et al. (2017) and Sweeney et al. (2016, 2018) show that ~150 to 200 Myr separate each morphologic class. The age constraints, coupled with morphometric data gathered from HiRISE DEMs, indicate that craters here predominately degrade through relatively slow diffusional slope processes (e.g., mass wasting, gravitational creep and eolian abrasion) at rates similar to other estimated erosion rates on Hesperian-age terrains on Mars (Sweeney et al. 2018), including Gusev crater (Spirit) (Golombek et al. 2006a,b) and Chryse Planitia (Pathfinder) (Golombek and Bridges 2000). The measured reduction in rim height over measurement time intervals of ~150 Myr and ~500 Myr indicates extremely slow surface erosion rates relative to terrestrial and Noachian rates on Mars of ~0.02 m Myr^{-1} and 0.002 m Myr^{-1}, respectively (see Golombek et al. 2014 for discussion). However, slope processes do not account for the total crater depth-related degradation, as a significant component of eolian infill is also observed.

Eolian bedforms occur almost exclusively on the floors and within the ejecta blankets of all RECs, suggesting that the impact process supplies the sand. Fragmentation theory supports the likelihood that ongoing comminution of bedrock to regolith by impact gardening can produce an

abundance of sand-size material (Charalambous et al. 2017; Morgan et al. 2018). Comparing the morphology of Class 1 craters to Class 5 craters, eolian materials organize into bedforms soon after crater formation and migrate over the rims and into the interiors of the craters, contributing to the total depth degradation. Through a comparison of crater topographic profiles from DEMs at different states of modification that are modeled through diffusional slope modification, ~30% of the total measured depth-related degradation at the Insight landing site is related to eolian infill (Sweeney et al. 2018). Using the age constraints for the RECs, this provides an eolian infill rate of ~0.008 m Myr^{-1}. Combined with rim erosion, the infill rate results in an overall crater degradation rate of 0.03 m Myr^{-1} and 0.01 m Myr^{-1} measured over 150 Myr and 500 Myr, respectively. These rates are so slow, that they argue for a surface dominated by impact and eolian processes since the lava flows were deposited (e.g., Golombek et al. 2014, 2017).

3.7. Fragmentation

Fragmentation theory developed by Charalambous (2015) shows that repeated fragmentation can be modeled by a negative binomial (NB). Using the observed rock distribution at the landing site, the theory was used to determine the abundance of 10 cm size rocks that could potentially stop the HP^3 mole (Golombek et al. 2017). The size-frequency distribution of impact craters and the age of the surface was used to define a maturity index to synthesize the particle size distribution of the regolith.

A compilation of rock counts from HiRISE images for the InSight, Phoenix and Spirit landing sites and surface rock counts from the later two was matched using fragmentation theory (Golombek et al. 2017). The model predicts that the rock population down to 5-10 cm is likely similar to that observed at the Spirit landing site (Columbia Memorial Station, CMS) (Golombek et al. 2006a, 2017). Subsequently, the model was extrapolated to smaller size particles (~0.6 mm,

coarse sand) (Morgan et al. 2018; Charalambous et al. 2017) using microscopic image measurements of the size-frequency distribution of sand at the Spirit and Curiosity landing sites (McGlynn et al. 2011; Minitti et al. 2013; Ehlmann et al. 2018). This extrapolation indicates that sand at the InSight landing site could have been produced by impact comminution.

3.8. Surface Modification During Landing

All previous landers on Mars have modified the surface during landing (e.g. Smith et al. 2009; Daubar et al. 2015). The InSight lander will use pulsed retropropulsive thrusters to slow itself during landing. The thrusters on InSight are the same as those used by the Phoenix lander, which dispersed 5-18 cm of soil when landing, exposing hard unaltered ice (Mehta et al. 2011). Modeling showed that pulsed thrusters lead to explosive erosion via cyclic shock waves that fluidize soils, producing ten times greater erosion than conventional jets (Mehta et al. 2011; 2013). For Phoenix, craters of approximately 80 cm diameter and 13 cm depth formed where the exhaust plumes impinged on the surface. Conservative estimates of the maximum possible crater size, generated by applying a conservation of momentum analysis, indicate an upper limit of 1.6 m on the crater diameter and an upper limit of 40 cm on the crater depth. The best estimate predictions of 1.1 m diameter and 18 cm depth are notably smaller than the bounding estimate. Regardless, there should be negligible impact to the topography at the lander footpad locations (and thus the surface modification from the thrusters won't pose a risk to landing, Golombek et al. 2017) or the instrument deployment zone given the distance to the thruster impingement points. Nevertheless, surface soils will be dispersed away from the lander with sand and pebbles being eroded from the jet impingement locations and deposited away from the spacecraft.

The landing site surface is expected to be covered with fine, high-albedo dust (Golombek et al. 2017) that will be displaced by the lander thrusters (e.g., Daubar et al. 2015; Mehta et al.

2013, 2011; Plemmons et al. 2008). As a result, the surface albedo will be lowered, as has occurred around previous landers. The albedo decrease can be predicted to be intermediate between the cases of Phoenix and MSL. Daubar et al. (2015) measured the albedo changes at these sites. For the MSL descent stage, the albedo was initially lowered by ~50%. The majority of the darkened area faded to ~90% of the surrounding albedo by ~500 days after landing, but the darkest areas did not disappear completely in a few Mars years. The Phoenix landing reduced the albedo to ~60-80% of the surrounding surface. Tracking the fading of the darkened area was incomplete due to seasonal imaging limitations at high latitude, but the darkened area disappeared completely over the first winter at the site (Daubar et al., 2015). Polar seasonal processes most likely played a part in this disappearance (this will not be the case for InSight). Based on these observations, we predict the surface albedo at the InSight landing site will be reduced by ~20-50% upon landing, then exhibit a rapid initial brightening, and then gradually return to the surrounding albedo over the next several Mars years.

4. Surface Operations

4.1. Selecting Instrument Placement Sites

After landing and assessment of the condition of the lander, the most important activity is placing the instruments onto the surface as quickly as possible (Banerdt et al. 2018). Project surface operations scenarios allocate approximately 50 sols for deploying the SEIS, WTS and HP^3 within a crescent-shaped workspace that can be reached by the arm. During the first two weeks, the Instrument Site Selection Working Group (ISSWG) must decide where to place the instruments in the workspace based on the spacecraft tilt, workspace topography, surface characteristics (soils, rocks, etc.) and instrument placement requirements. Because much of this activity relies

extensively on the geology and physical properties of surface materials in the workspace, we include a description of this phase of surface operations in this paper.

4.2. ISSWG Operations Group

The ISSWG is an operations group of the project tasked with selecting the locations to place the instruments. It will evaluate the suitability of deploying the instruments at locations in the workspace that meet the instrument deployment requirements that stem from the instrument configurations, surface properties and topography, and arrangement of the tethers from the lander to the instruments. The ISSWG is composed of six subgroups: geology, physical properties, arm and deployment engineers, MIPL, and instrument representatives for SEIS and HP^3. The geology subgroup will evaluate the surficial geology and map soils, rocks, eolian bedforms and other geological features such as craters. The physical properties subgroup derives the thermal inertia from hourly radiometer measurements of two spots on the surface (which are on the opposite side, north of the lander from the instrument deployment workspace), separates the rocky from fine component of the thermal inertia from stereo surface images and measurements of their areal contributions, and estimates particle size and cohesion of the fine component to determine if the soil is load bearing. The soil maps from the geology subgroup allow the extrapolation of physical properties of similar materials to the workspace. The arm and deployment engineers derive the workspace from the attitude of the lander and topography of the surface, evaluate locations in the workspace where the arm can deploy the instruments, and assess instrument tether configurations. MIPL creates and distributes the image products upon which most of the analysis of the other groups rely on (see Section 4.7). Representatives from the SEIS and HP^3 teams evaluate prospective locations where their instruments can be deployed and produce noise maps to identify preferred deployment positions.

4.3. Workspace

The instrument deployment workspace is the area in front (south) of the lander where the IDA can place the SEIS, WTS, and HP^3. The instrument deployment workspace for a horizontal lander in flat terrain with nominal lander deck height are shown in Figures 15 and 16 for SEIS and HP^3, respectively. The workspace boundary is a convolution of the following requirements and constraints: IDA kinematics, collision prevention between lander deck and IDA, IDA torque limits, and instrument tether length. The IDA reachability constraints change as a function of lander tilt, lander deck height, and terrain geometry. The final extent of the workspace will be updated after landing based on actual lander attitude knowledge. For SEIS and WTS placement, there is an additional constraint to have a minimum standoff of WTS over SEIS so the two do not touch. There is also an additional unique constraint for SEIS placement that the tether pinning mass be reachable with the IDA scoop so that its position can be adjusted if necessary. The reason for adjusting the location of the pinning mass is to assist the separation of the load shunt assembly (LSA) mechanism. Separation of the LSA is required for SEIS to meet its performance requirements as it enables the SEIS service loop to dampen the effects of tether thermoelastic noise on the seismic measurements. In addition, there is margin added for 3 cm placement accuracy and a requirement to be able to recapture the instruments by the grapple if necessary. As discussed in the subsequent sections on the instrument deployment requirements, desirements, and noise considerations, the "preferred" deployment locations for SEIS is located as far from the two southern lander feet as possible. For HP^3 the preferred location is as far from the lander as possible and >1 m to the east of SEIS.

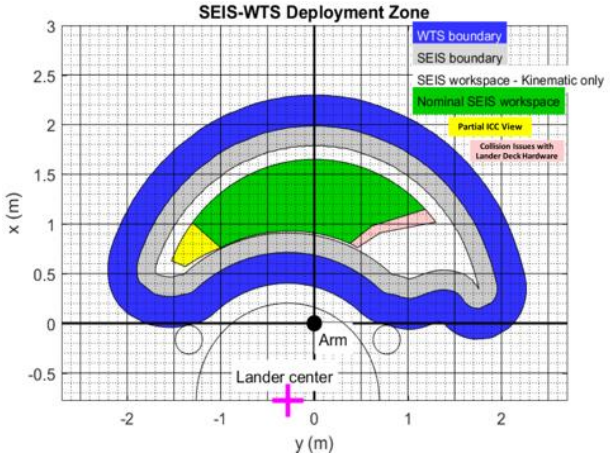

Figure 15. Dimensional SEIS and WTS instrument deployment workspace (note x and y dimensions in m) showing the lander, center, arm and lander feet (circles). The green area is the nominal SEIS deployment area. The surrounding grey and blue areas show the edge of the SEIS and WTS if the instrument is placed at the boundary of the green area. The white represents the area that is reachable with the grapple, but the nominal SEIS workspace is reduced to the green area to allow for margin to recapture the instrument and to provide sufficient clearance of WTS over SEIS during WTS deployment. The yellow area shows where the ICC view of the instrument site is partially obscured by lander deck hardware and the pink represents an area where there are reachability issues due to close clearances between the IDA and lander deck hardware. The spacecraft is programmed to land with the workspace facing due south (so south is in the +x direction).

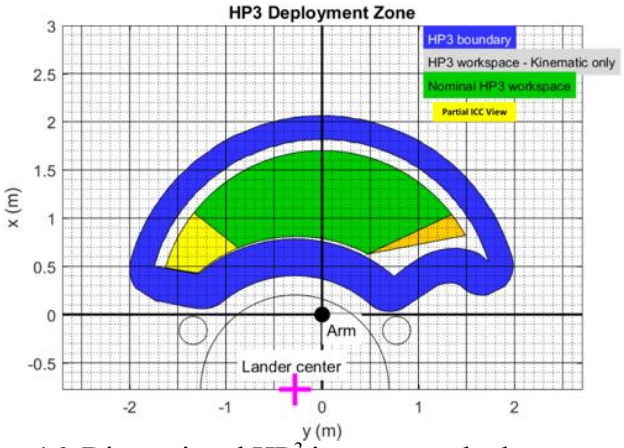

Figure 16. Dimensional HP^3 instrument deployment workspace showing the lander, center, arm and lander feet (circles). Green area is the nominal HP^3 deployment area. The blue area shows the edge of the HP^3 instrument if placed at the extreme edge of the workspace. The yellow area is only partially in view by the ICC. The orange represents an area where there are reachability issues due to close clearances between the IDA and lander deck hardware. Note that south is in the +x direction.

4.4. Instrument Placement Requirements

In addition to falling within the constraints of the deployment workspace, each instrument site must satisfy additional requirements resulting from the instrument capability and performance. These requirements as well as some "desirements" are summarized in Tables 1 and 2. SEIS has a leveling system that can accommodate up to 15° and the HP^3 mole is designed to penetrate close to the gravity vector so both instruments and the WTS must be deployed on surfaces with slopes of <15° (and <13° negative pitch for SEIS). Both the SEIS leveling system and HP^3 have clearances of ~3 cm and so must be placed on surfaces with no rocks or protrusions higher than 3 cm. In addition, the SEIS leveling system can accommodate rocks or protrusions <2 cm and <1 cm high for instrument tilts of 11°-13° and 13°-15°, respectively. For stability, footpatch roughness or relief of both instruments must be less than 1.5 cm, and WTS <3 cm. The soil beneath both instruments and WTS must be load bearing, as unequal sinkage could lead to additional tilt. After deployment, SEIS and WTS must not touch (for noise reasons), so the SEIS footplane (the plane formed by the SEIS feet) must be less than 1.5 cm higher than the WTS footplane and the relative tilt between the two must be less than 5°.

Both instruments have "desirements" for deployment. SEIS would prefer to be >1 m from HP^3 to reduce noise. HP^3 has a similar desirement to be >0.9 m from WTS to avoid thermal noise from shadows. If HP^3 is deployed to the east (left from the lander) of SEIS, the tethers will not cross, resulting in a simpler deployment, although crossing tethers will be acceptable in some cases. There are also constraints on the location of the SEIS tether pinning mass (to mechanically isolate SEIS from the tether, Lognonné et al. 2018) and the tether field joint (the connection between the two SEIS tether sections, one from the lander and one from the instrument). The pinning mass and field joint must be free of rocks or other obstructions and on a gentle slope so

that if the pinning mass needs to be moved, there will not be obstacles or a tilt hindering the movement. Finally, the HP^3 would prefer to have no rocks beneath the mole exit and be placed in a configuration in which any instrument rocking is minimal with all four feet on a single plane.

Table 1. SEIS & WTS Deployment Site Requirements.

SEIS & WTS Deployment Site Requirements
Requirements
Tilt
SEIS < 15 ° Tilt (must also be < 13° of negative pitch)
WTS <15° Tilt
Terrain
No Rocks Under SEIS > 3 cm high for tilts ≤ 11°
No Rocks Under SEIS > 2 cm high for 11° < tilt ≤ 13°
No Rocks Under SEIS ≥ 1 cm high for 13° <tilt ≤ 15°
No Rocks under WTS > 6 cm high
SEIS Footpatch Roughness: <1.5 cm
WTS Footpatch Roughness: <3 cm
Load Bearing Soil
SEIS/WTS Relative Placement
SEIS footplane < 1.5 cm higher than WTS footplane
Less than 5° relative tilt between SEIS/WTS
SEIS not to exceed WTS DNE envelope
Desirements
Tether Configuration
Place SEIS on the right side of workspace to avoid tether crossing
No rocks under pinning mass or field joint
Pinning mass orientation desireable for adjustment with scoop
SEIS Noise – wind and other noise sources
SEIS Away from the lander
SEIS >= 1m away from HP3

Table 2. HP^3 Deployment Site Requirements.

HP3 Deployment Site Requirements

Requirements
HP3 tilt < 15°
HP3 No Rock under: > 3 cm high
HP3 Footpatch Roughness: <1.5 cm
Load Bearing Soil
Desirements
HP3 Away from Lander (thermal noise map)
HP3 Shadows (Noise) – Thermal map
Mole exit clear of rocks
HP3 Slopes – rocking
HP3 >= 0.9m from SEIS (away from WTS shadow)

4.5. SEIS Noise Placement Considerations

The various noise contributions (both instrumental and environmental) that are expected to influence the seismic measurements of InSight are described in detail in Mimoun et al. (2017). One of the main environmental noise contributors expected to be measured by SEIS, in addition to the atmospheric pressure noise (Murdoch et al. 2017a,b), is the mechanical noise of the lander transmitted through the ground to the seismometer. The dynamic pressure due to wind results in stresses on the InSight lander body, leading to ground deformation at the lander feet that are transmitted to the SEIS feet, as demonstrated by Murdoch et al., (2017b) using an elastic ground deformation model. Several key parameters influence the noise contribution of the lander: the distance between SEIS and the lander feet, the mean slope on which the lander is located, and the wind speed and direction. Using the same modeling approach, the mechanical noise the HP^3 instrument creates has also been calculated to constrain the relative deployment positions of SEIS and the HP^3. We find that, to remain (statistically) within the noise budget (Mimoun et al. 2017), the centers of SEIS and HP^3 should be at least 1 m apart (assuming day time, 70% wind amplitudes;

see Murdoch et al. 2017b). Therefore, in order to minimize both the lander and HP^3 mechanical noise and other noise sources such as the thermoelastic deformation of SEIS and the tether (see Mimoun et al. 2017), it is desirable to choose a deployment site as far from the lander as possible and at least 1 m from the HP^3, which has the smallest temperature variations, and on ground as flat as possible with similar soil properties beneath each of the three SEIS feet. In addition, a stiff, consolidated soil below the SEIS feet could be advantageous by minimizing unequal penetration of the spikes that could tilt the instrument. Noise "maps" have been developed to indicate where the highest and lowest noise levels that are expected to be found within the SEIS deployment zone for a given set of ground, winds and HP^3 locations. These noise maps will be updated to incorporate specific properties of the site after landing to aid in selecting optimal locations for SEIS, particularly if the preferred instrument locations are unsuitable.

4.6. HP^3 Thermal Placement Considerations

To accurately determine the martian planetary heat flow, measurements of subsurface temperatures by the HP^3 instrument should reflect the undisturbed subsurface temperature profile. However, the presence of the InSight lander as well as the WTS will change the surface energy balance by casting shadows that will move with the azimuth and inclination of the Sun. Thermal perturbations will slowly diffuse into the subsurface, and thus it is desired to place the HP^3 instrument as far as feasible from shadows. With the lander in the default east-west facing orientation with the workspace to the south, HP^3 should be deployed directly south of the lander to minimize thermal disturbances (Siegler et al. 2017), while at the same time keeping a distance of roughly 1 m from the WTS (Grott 2009).

4.7. Image Processing

The ISSWG process is highly dependent on image products, and especially mosaics, created from the IDC and ICC cameras (e.g., Maki et al. 2018). These products are created by the MIPL at JPL, which also performs similar functions for the MER, MSL, Mars 2020, and Phoenix missions. The software used is the Mars software suite (Alexander et al. 2006; Deen et al. 2003), part of the Video Image Communication And Retrieval (VICAR) image processing system (VICAR 2016). It is a reusable, multimission set of applications and libraries designed for Mars lander and rover operations. Functions include stereo correlation, mosaic generation, terrain mesh generation, radiometric correction, pointing correction (bundle adjustment), linearization (epipolar alignment), and creation of derived, mission-specific products such as surface normals, slope maps, arm reachability maps, XYZ point clouds, and roughness maps. A pipeline handles systematic, automated execution of the programs that create these products on every image and stereo pair received. In all, 56 different image products will be made from each InSight stereo pair (Deen et al. 2018), mostly within a half hour of receipt of the data.

The IDC is a single camera mounted on the arm; it is not a stereo camera. To achieve stereo with a single, arm-mounted camera, two images without the usual stereo toe in (where they are pointed to a common focal point) are acquired from different locations typically by moving only the shoulder joint to reduce error. Each IDC frame is marked as a left eye or right eye image to create a disparity map (or spatial difference between a feature's location in the left and right images of a stereo pair). The disparity map is then used to create an XYZ point cloud in which rays are projected out into space using the camera model for each eye (e.g., Alexander et al. 2006; Deen et al. 2018).

ISSWG work is vastly facilitated by mosaics and data products showing an overhead view of the workspace. These pointing-corrected mosaics are created by an analyst using MIPL software

tools and the stereo products described above. Once multiple sets of stereo pairs are processed, an iterative pointing correction (bundle adjustment) process minimizes geometric seams (discontinuities) between frames. The results of pointing correction are fed back into the individual image inputs, resulting in adjusted XYZ points and other derived values. Once pointing-corrected XYZ products are generated, orthorectified mosaics are processed at both 1 mm and 2 mm resolution from the images (Figure 17a). Orthorectified mosaics use the stereo-derived XYZ data to show a "true" overhead view of the scene, without distortion due to parallax. The removal of parallax necessarily leads to holes or gaps in the mosaic behind obstructions (e.g. rocks). Orthorectified mosaics are created for both the images and Z values; the latter creates a digital elevation model (DEM) (Figure 17b). In addition to the products described in the next sections, other standard MIPL products commonly used for terrain assessment include terrain slope (which is distinct from instrument tilt), and the component of slope in the radial direction, outward from the lander. See Maki et al. (2018) for more details on image processing of ICC and IDC data.

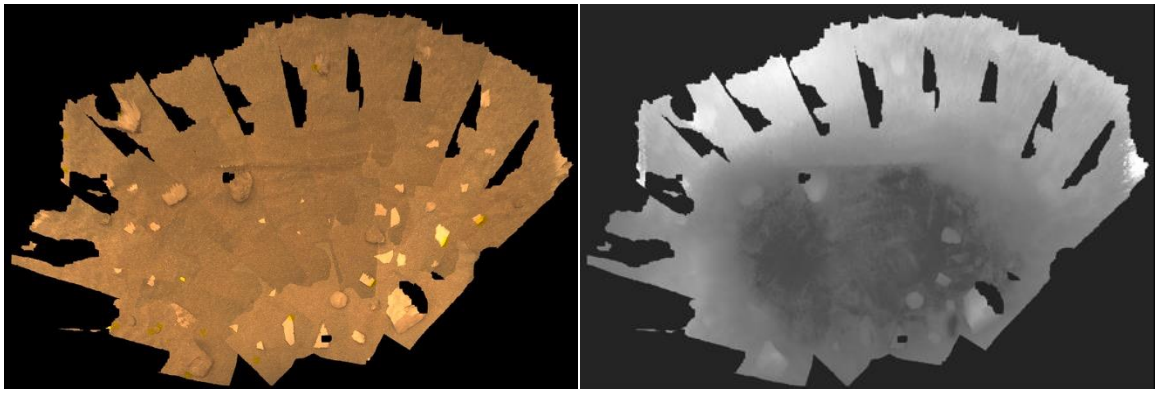

Figure 17. (a). Example orthorectified IDC mosaic of the workspace created from stereo images taken before launch by an engineering model camera in the JPL testbed. Note data gaps behind rocks produced by image pair parallax, and gaps due to obscuration of the IDC image by the arm/grapple in the upper tier. (b). DEM of the same mosaic. Darker tones are lower in elevation and lighter tones higher.

4.7.1 Instrument Placement Products

Unique to InSight are a number of "instrument placement" products, which show the instrument tilt, roughness of terrain under the instrument, or delta tilt between the SEIS and WTS at any point in the workspace. At each point, the instrument is virtually placed with the grapple at those pixel coordinates. The instrument is "settled" onto the terrain, with an allowance for sinkage of the legs beneath the surface. Because the SEIS and WTS feet are narrow with spikes underneath, they are designed to sink up to 2 cm in unconsolidated sand – or not at all, if it is hard rock. This sinkage will affect both the tilt and the clearance underneath the instrument. Thus, the programs model each leg sinking, or not, independently of the other legs, up to 1.5 cm for SEIS, and 2.0 cm for WTS. The wide feet of the HP^3 make sinkage unlikely, so no sinkage is modeled. The WTS is nominally placed 5 cm closer to the lander than the SEIS, in order to better accommodate the LSA. Thus, the WTS products analyze a spot 5 cm closer to the lander (radially in IDA coordinate frame), but report the results at the pixel indicating where the SEIS is deployed. This is especially notable for delta tilt (section 4.7.4).

The instrument deployment mechanism does not control the axial rotation or "clock angle" of the instrument, although it is constrained to be within a range of ±15° of the tether, which deploys radially from the lander. To account for this, the analysis is repeated at a range of likely clock angles (-15°, 0°, and +15°, where 0° is defined to be the angle where the tether goes straight back to the lander deployment point). The minimum and/or maximum values across all clock angles and sinkage values are gathered, and the results are stored in the placement product at that pixel. In each case, a "goodness" value is included in the image product that indicates whether the values are within established thresholds set by the instrument placement requirements (Section 4.4).

High level descriptions of these placement products are presented below, with details given in Deen et al. (2018). It is important to note that each pixel represents the entire state of the instrument if placed at that point. In other words, if areas that pass thresholds are encoded in green, only the central pixel will be green, not the entire area covered by the instrument.

4.7.2 Workspace

The IDC workspace mosaic (Figure 18) shows the reachable boundaries of where the InSight instruments can be deployed as specified in section 4.3. The boundaries are computed by incorporating the effect of the tilt of the lander (which affects the angle at which the grapple hangs) on where the arm can reach for each instrument. Workspace mosaics are made for both the HP^3 and combined SEIS/WTS.

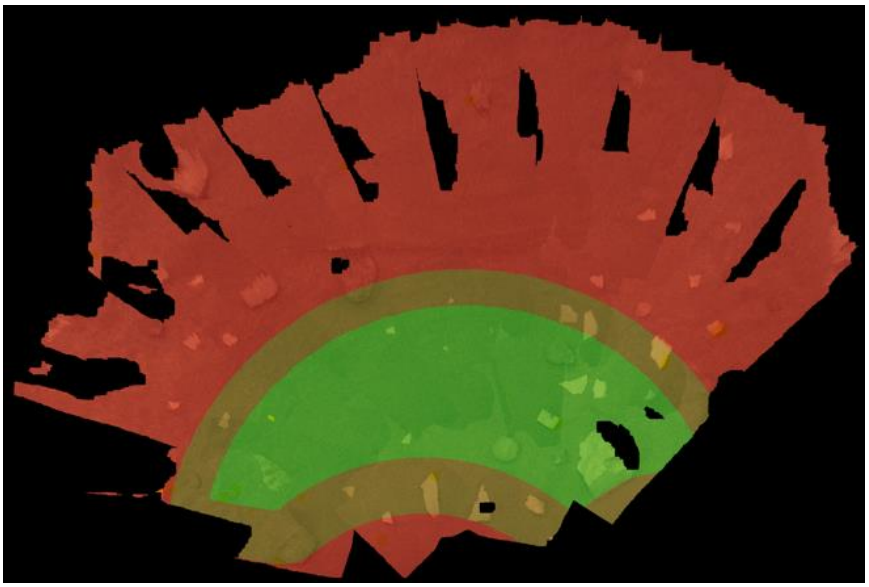

Figure 18. Example mosaic showing the workspace for HP^3 overlaid on the IDC orthomosaic of the JPL testbed. The area in bright green shows where the grapple point for HP^3 could be placed, with the yellow area showing the extent of the instrument beyond the grapple point, and red showing areas where HP^3 can not be placed.

4.7.3 Instrument Tilt

The instrument tilt product computes the absolute tilt (in degrees, relative to the gravity vector) an InSight instrument would have if it were placed at the given pixel (Figure 19). Tilts are calculated from the plane created from the location of the three feet at a given grapple location, and the maximum dip of the plane defines the tilt. Tilt is determined by trying all combinations of foot sinkage and a range of clock angles for the instrument. In the case of HP^3, which has 4 feet, all combinations of 3 feet are calculated in case the 4th foot does not contact the ground. The minimum and maximum values of tilt across all of these cases are determined and reported in the tilt product. All pixels where the maximum tilt is within the placement requirements of <15° are marked as acceptable.

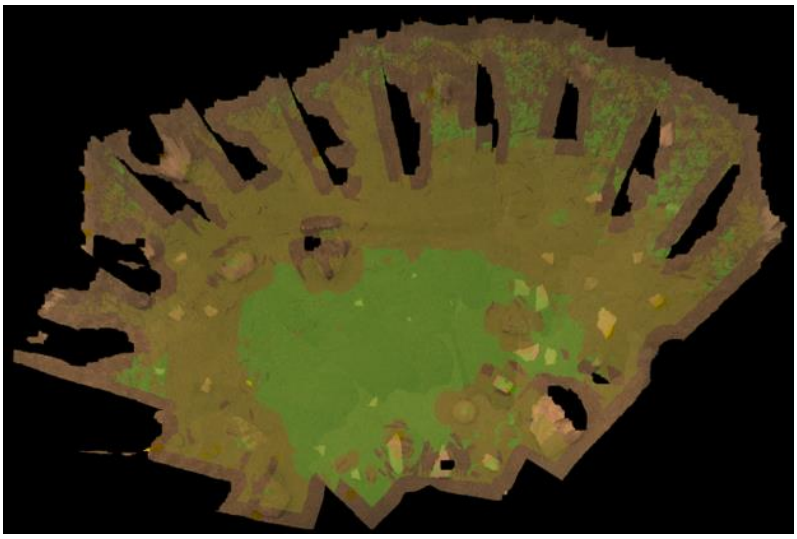

Figure 19. Example workspace mosaic of SEIS tilt overlaid on the IDC orthomosaic of the JPL testbed. The green areas are within the tilt threshold of <15°, indicating the instrument would meet tilt requirements if placed there. Yellow indicates the threshold was exceeded, whereas brown are areas where no solution was obtained due to lack of stereo overlap.

4.7.4 Delta Tilt

The delta-tilt product (Figure 20) computes the difference between the tilts of the SEIS and WTS to ensure that they don't touch. It is computed by first determining the SEIS tilt as described

above. At each SEIS point, the tilt of the WTS is also computed in the same manner, except the feet are clocked independently, and the WTS is offset toward the lander by 5 cm. The arc cosine of the dot product between the two normal vectors is the delta tilt. Areas where the delta tilt is within the <5° limit are marked as acceptable.

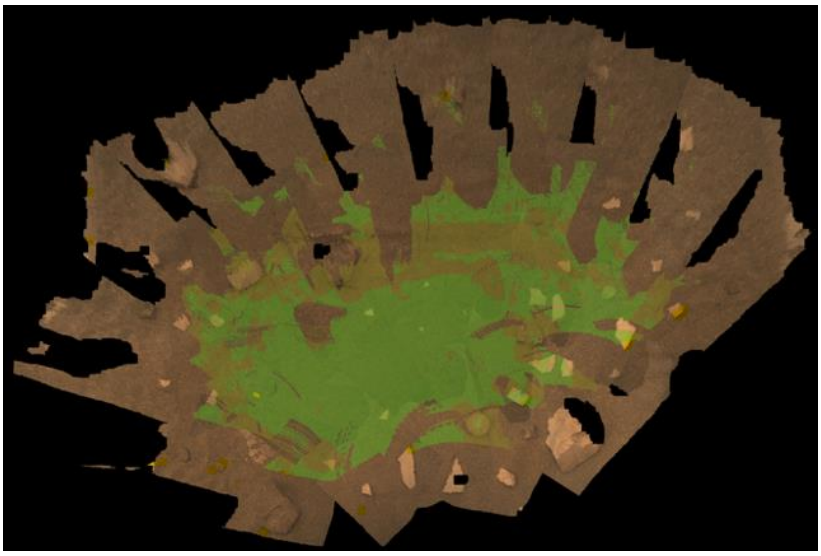

Figure 20. Example workspace mosaic of the SEIS-WTS delta-tilt overlaid on the IDC orthomosaic of the JPL testbed. Green pixels indicate a point within threshold of <5° where the instrument would meet delta-tilt requirements if placed there. Yellow indicates the threshold was exceeded, whereas brown are areas where no solution was obtained due to lack of stereo overlap.

4.7.5 Instrument Roughness

The instrument roughness product (Figure 21) determines two aspects of surface roughness underneath the instrument. Generally, roughness is defined as the maximum difference of any two points (after outlier rejection) above or below the plane defined by the instrument. In order to make this product computationally tractable, roughness analysis is carried out using only one value of instrument tilt (and thus one plane, at a clock angle of 0°), with no sinkage. However, a range of clock angles is used to determine the locations of the feet for the roughness calculation.

The first aspect, called footpatch or foot roughness, is a measure of roughness in the area covered by the feet. It thus considers only pixels in the area of the feet, and looks for both (small

scale) hills and valleys in those areas; the foot can sit on top of a hill, but could also slip into a valley. The footpatch thresholds are 1.5 cm for SEIS, 3 cm for WTS, and 1.5 cm for HP^3.

The second aspect, called footplane or body roughness, is concerned with clearance for the belly of the instrument. Thus, valleys are not relevant, as the instrument can clear them but rocks or "hills" sticking up can be a problem. This roughness examines pixels across the entire body of the instrument, but only looks for excursions *above* the plane defined by the instrument feet. For this computation, fully sunk feet are assumed, since that is the worst case for roughness above the plane. The footplane thresholds are 3 cm for SEIS, 6 cm for WTS, and 3 cm for HP^3. Note that the "No rocks under SEIS" requirements in Table 1 varies based on the actual tilt, which is always assumed to be a worst-case. Both maximum footpatch and footplane roughness are reported in the product. All areas that are within the threshold for both footpatch and footplane roughness are marked as acceptable.

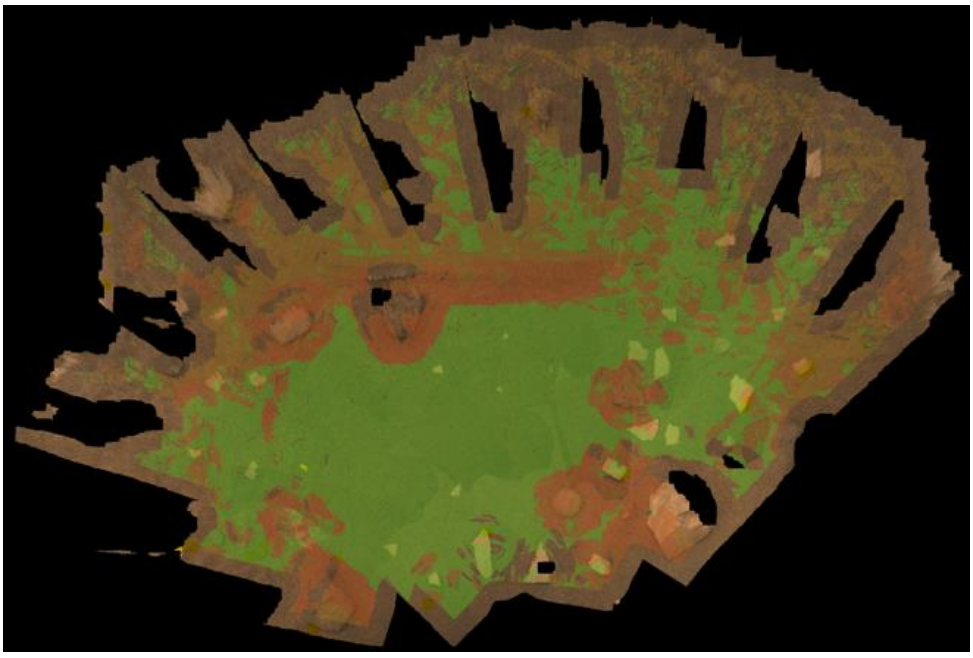

Figure 21. Example workspace mosaic of HP^3 roughness overlaid on the IDC orthomosaic of the JPL testbed. Green pixels indicate points where both roughness values are within the threshold, i.e. the instrument would meet roughness requirements if placed there; orange pixels show one of the roughness requirements for either the footplane or footpatch is met and

red pixels show where neither requirement is met. Brown are areas where no solution was obtained due to lack of stereo overlap.

4.7.6 Instrument Goodness

The goodness maps (Figure 22), are products that summarize locations where all the instrument deployment products described above for each of SEIS/WTS and HP^3 are acceptable. This includes workspace boundaries, maximum tilt (and delta-tilt for SEIS/WTS), and the maximum roughness for footpatch and footplane. This product is intended as the first "go to" product to assess overall accessibility for deployment, before assessing details of the specific instrument locations (e.g., it does not represent individual rock sizes, soil properties or tether configurations).

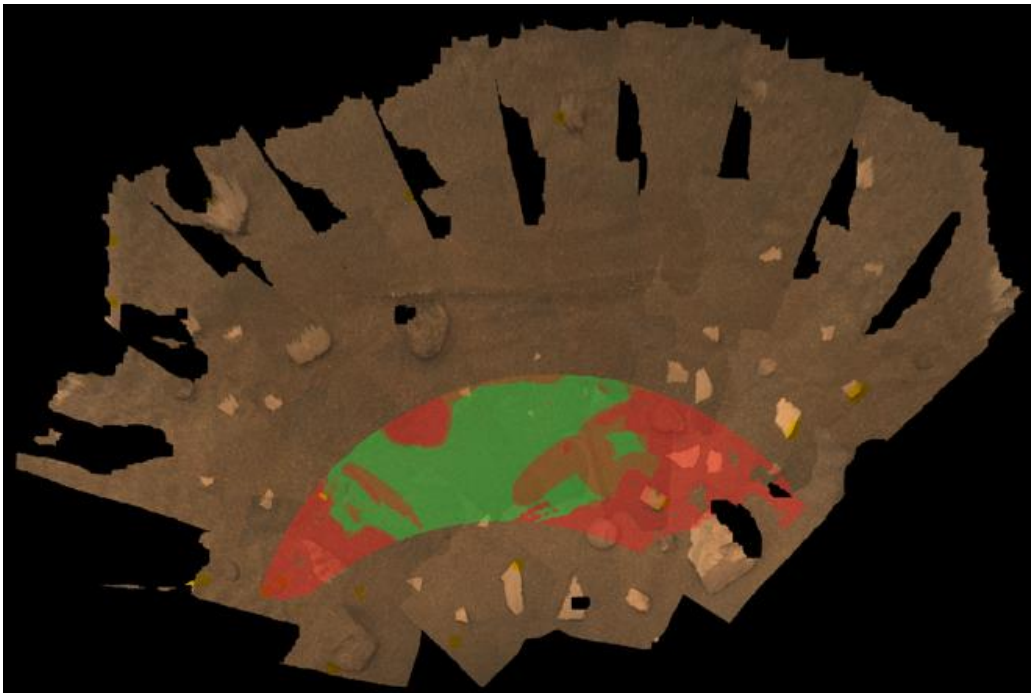

Figure 22. Example workspace mosaic of goodness for SEIS overlaid on the IDC orthomosaic of the JPL testbed. Green pixels represent locations that pass all of the instrument placement criteria, orange represents one requirement has been violated, and red means two or more criteria are violated.

4.8. ISSWG Phases

There are three phases of ISSWG operations whose timing is determined by when data are acquired by the spacecraft, downlinked to earth, processed into data products and when decisions are made based on the data: 1) initial assessment, 2) systematic workspace mapping and site selection, and 3) site confirmation with high-resolution imaging. Time between phases is also allotted for data analysis and decisions to be made based on the data. Note that although the ISSWG timeline is based on sols, InSight operations during this time will be performed on a modified Earth time schedule, which shifts to accommodate Mars time but does not require overnight work shifts. The timeline described is based on plans developed by the project for operations, but is subject to change.

4.8.1 ISSWG Phase 1: Initial Assessment

The first phase of ISSWG takes place during the first 4 sols (martian day) of the mission, which includes landing, assessment of the lander condition, and deploying the IDA. During this period, lander health and orientation are established, ICC images are obtained at different times of the day, the IDA is deployed, and the IDC acquires images of the spacecraft, lander footpads, context images in 4 directions and stereo images of the two radiometer spots.

During this period, only ICC images of the workspace are acquired (Figure 23a). Because the ICC is not a stereo camera, true overhead (orthorectified) mosaics cannot be made. Instead, vertical projections of the ICC images are created (Figure 23b). These provide an overhead view, but suffer from severe distortion due to layover effects as they project a mono image without range information onto a flat surface. A simulated three-dimensional map of the workspace using a flat surface is used to create a simulated workspace reachability map projected onto a two-dimensional plane (Figure 24). While this does not provide true workspace boundaries, it yields preliminary,

poorly controlled, qualitative maps in which to evaluate the surficial geology and discriminate areas of low slope that are relatively rock free in which the instruments might be deployed. The orientation and tilt of the lander (obtained from the spacecraft team right after landing) are used to create a map, assuming a flat surface (no stereo).

Later IDC images of the spacecraft feet will give initial views of surface soils and their alteration from the landing retro rockets. Context images will provide an idea of the surface setting. The ISSWG will evaluate these data and prioritize the return of data from IDC imaging campaign that begins on sol 5 so that the highest priority areas most suitable for instrument placement are downlinked first.

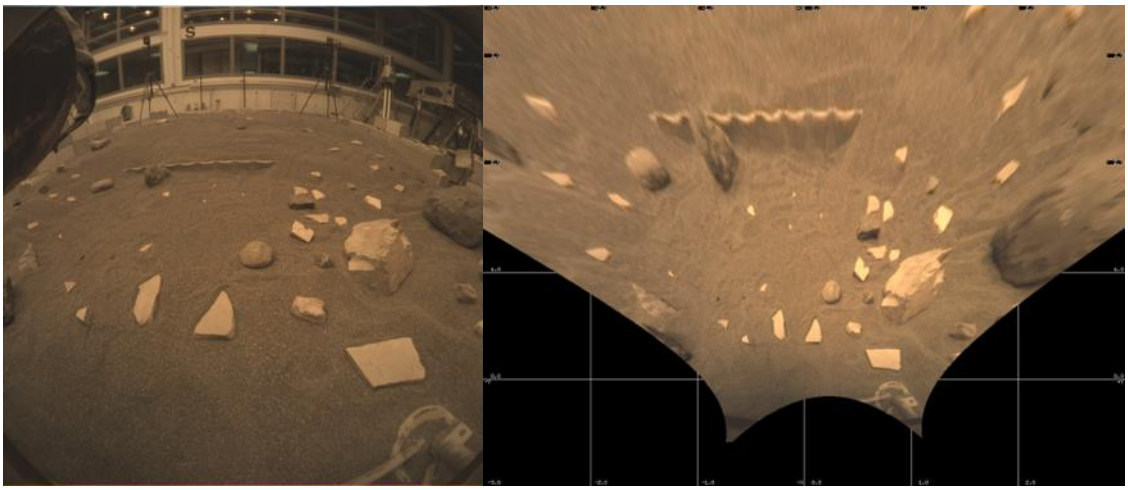

Figure 23. (a) Example ICC image acquired in the JPL testbed. (b) Vertical projection of the same ICC image showing the top down view of the workspace assuming a flat planar surface.

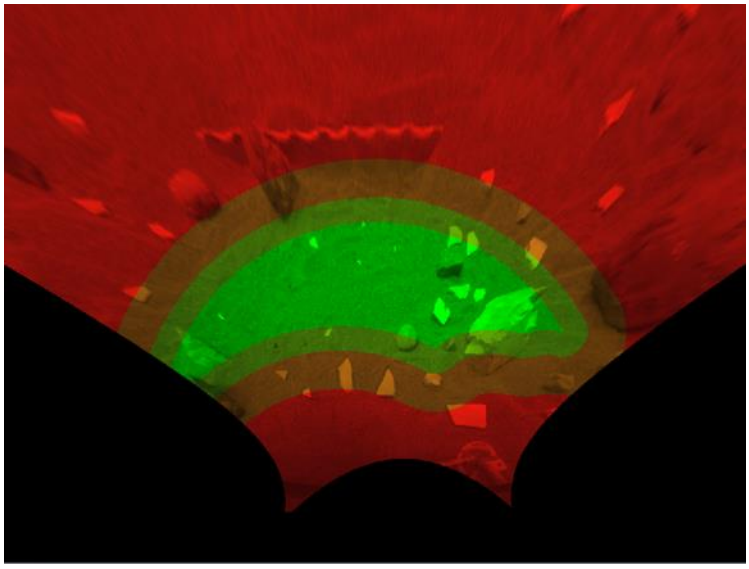

Figure 24. Example vertical projection of ICC image of the workspace in the JPL testbed for SEIS/WTS, assuming Cartesian coordinates projected on a flat plane. The areas in bright green show the center grapple point of the SEIS and WTS with darker shades showing their extents respectively, and red showing areas where the instruments cannot be deployed.

4.8.2 ISSWG Phase 2: Systematic Workspace Mapping and Site Selection

Phase 2, the period of the most intensive ISSWG work, starts on sol 5 when the IDC begins a systematic imaging campaign of the workspace with the camera higher than the lander deck (for safety). This workspace mosaic consists of 3 tiers of stereo images made up of 26 stereo image pairs total, and 4 "tie point" mono images that help to tie the tiers together with additional overlap. Each of the 56 images are taken 1.5 m above the nominal ground plane, which provides approximately 1.3 mm per pixel resolution. Using the DEM produced, MIPL creates derivative maps to aid in instrument deployment, as described in Section 4.7. Due to large data volumes, it may take multiple days to receive the full IDC workspace data set from the lander, so this may be an iterative process. Downlink of workspace areas will be prioritized during ISSWG Phase 1, so the most promising areas will arrive first. The MIPL products will be updated each day as new images are downlinked.

The DEMs and the orientation and tilt of the lander will be used to determine the geometry of the workspace and where the arm can place the SEIS, WTS, and HP^3. The configuration of the tether and the placement of the field joint and pinning mass can be evaluated from the DEMs and location of rocks. In addition, the mosaics can be used to map the surficial geology. Maps of different soil types based on their color, texture and presence of pebbles and rocks will be made along with the identification of eolian bedforms, rocks, and surface features. Measurement of rocks will allow size-frequency distributions to be plotted and the areal fraction of rock coverage. The relative areal fraction of rocks versus soil in the two radiometer spots can be measured and used to separate the rocky versus fine component of the bulk thermal inertia and then those physical properties can be extrapolated to the workspace. The particle size and cohesion can be inferred from the thermal inertia and used to determine if the soils are load bearing. Soils in the radiometer spots can be compared to soils in the workspace to infer their suitability for providing a stable footing for the instruments. The DEMs and rock maps along with the lander orientation and tilt will be used by the SEIS and HP^3 instrument teams to prepare noise maps for SEIS and thermal maps for HP^3, which will be used to evaluate potential instrument sites.

Based on all of these data, the ISSWG in Phase 2 will identify the best pair of sites for SEIS and WTS, and HP^3, and a backup pair if necessary. The project will also physically modify the JPL testbed, which includes a model of the lander, IDA, instruments and sandbox, to mimic the workspace on Mars and test instrument deployment at these sites.

4.8.3 ISSWG Phase 3: Site Confirmation with High-Resolution Imaging

The third and final phase of ISSWG involves confirming that the highest priority sites are in fact suitable for instrument deployments and meet all of the instrument deployment requirements. During this phase, starting on sol 9, higher resolution stereo images of the best sites will be obtained with the arm camera below the lander deck. These images will be acquired at a

lower height, with the IDC 1 m from the terrain as a confirmation of the site terrain geometry. The resolution of these images is about 0.8 mm per pixel. These images will be point-corrected, processed into higher-resolution orthorectified mosaics, and used to create all instrument placement products, in the same manner as in Phase 2. These images and data products will be used to confirm that the instrument sites meet all of the instrument deployment requirements.

At the end of all three phases, the ISSWG will brief the project, instrument PIs and mission PI on the status and recommendations. At the end of the third phase, on sol 12, the project will decide on which sites to place the SEIS, WTS and HP^3.

4.9. Instrument Deployment

The rest of the instrument deployment phase includes deploying SEIS on sol 19, leveling the SEIS, assessing the load shunt assembly and moving the pinning mass (if necessary) and imaging the instruments after each phase. Images will be taken at all phases of instrument deployment and mosaics made in order to confirm successful grapple, placement, release, and tether locations (e.g., Figure 25). WTS will be deployed on sol 39, HP^3 will be deployed on sol 47 and the mole will begin hammering on sol 55.

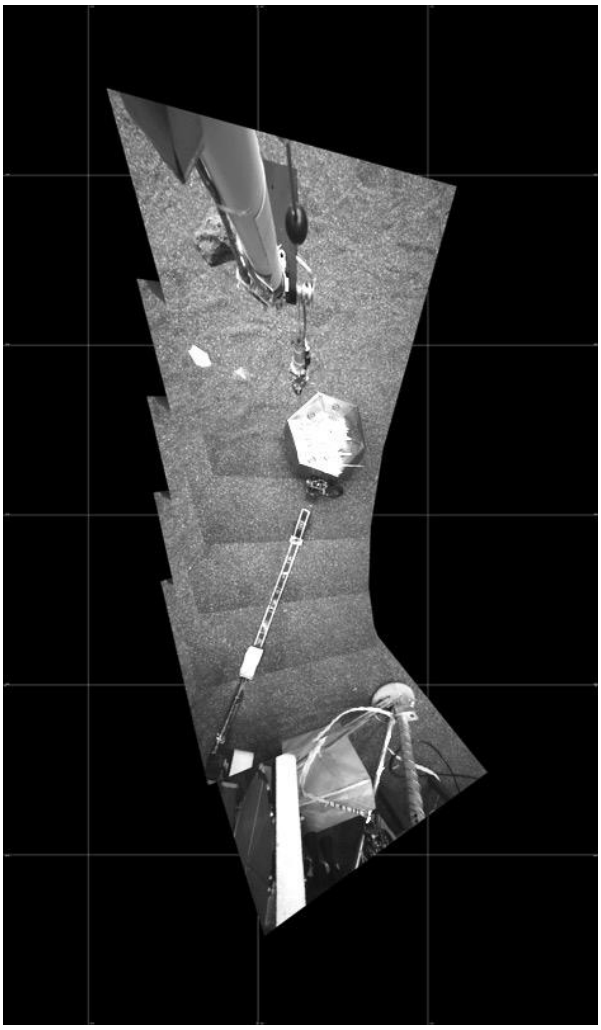

Figure 25. Example vertical projection confirmation mosaic of SEIS deployment and tether acquired in the JPL testbed. Note the location of the tether field joint near the lander and the LSA near SEIS.

4.10. Geology and Physical Properties Science Operations

The geology and physical properties investigations will be carried out by two science theme groups within the InSight operations team. These groups are the Geology and the Near Surface Properties Science Working Groups and are staffed by science team members interested in these investigations. During normal operations, decisions about what observations to carry out for the specific sols (martian day) being planned on Mars by InSight are made by the Science Operations

Working Group (SOWG). At each SOWG meeting, a member from each of the Geology and Near Surface Properties Groups will advocate for observations important to these investigations based on prioritized observations and activities developed by the group. Observations and activities relevant to geology and physical properties would be coordinated by the Geology and Near Surface Properties Science Working Groups, respectively. Surface changes due to atmosphere surface interactions would be coordinated with the Atmospheres Science Working Group. Determining the location of the lander in cartographic space and coordinating HiRISE imaging of InSight after landing would be done by the Geology Science Working Group. After instrument deployment is complete operations planning will proceed on a weekly basis. The stereo color panorama has been elevated into a project requirement. Soil mechanics experiments with the arm would begin after instrument deployment is completed.

5. Geology Investigation

5.1. Geology of Landing Site

The surface geology investigation will characterize the geology of the InSight landing site, and provide ground truth for orbital remote sensing data. Similar investigations for previous missions have established the basic geologic evolution of the local region, identified the geologic materials present, and quantified their areal coverage. By understanding the materials that surround the InSight lander, the site can be also be used as ground truth for orbital remote sensing data and thus aid in scientific analysis and future landing site selections (e.g., Golombek et al. 2008a).

5.2. Geologic Materials and Surfaces

The geological materials and surfaces present can be mapped in surface images by evaluating their texture, fabric and color. Surface images of all landing sites on Mars have thus

been analyzed to determine the surficial geology, the geologic evolution of the area and processes responsible. Although rovers have a distinct advantage understanding the geology by being able to traverse and inspect surface materials at disparate locations up close, even fixed landers (Viking Lander 1 and 2, Phoenix) or those with a small rover (Pathfinder) have performed successful surface geology investigations (e.g., Binder et al. 1977; Mutch et al. 1977; Smith et al. 2009; Golombek et al. 1997a). These investigations characterized and mapped soil deposits, rocks and their distributions, and identified eolian bedforms, craters, and troughs (due to ice). They also placed the surfaces observed into orbital context and showed that materials and their properties observed by the landers could be related to orbital remote sensing observations (e.g., Christensen and Moore 1992; Golombek et al. 2008a).

The InSight geology investigation will be similar to those conducted by these previous missions. Color images of the surface will be examined to distinguish different geologic materials such as soils, rocks, and bedrock. In addition, craters, eolian bedforms and any other geologic features observed will be mapped. Stereo images and full 360° panoramas along with images of the lander feet and area beneath the lander will be examined for alteration during landing. Thermal inertia of the radiometer spots will provide information about particle size and cohesion (section 4.6). The areal extent of different materials will be measured along with the sizes of rocks within view of the lander. Rock morphology, morphometry and size-frequency distributions can be characterized and measured and related to their origin and emplacement (e.g., Garvin et al. 1981; Craddock and Golombek 2016). All of these observations can be compared to expectations from orbital data and used to characterize the material present on Mars and improve future landing site selection (e.g., Christensen and Moore 1992; Golombek et al. 2008a).

5.3. Geologic Evolution and Subsurface Structure

The information gathered about the geology of the surface can be used to infer the geologic processes responsible and the geologic evolution of the surface. As examples, eolian bedforms and craters indicate saltation of sand size grains and impact processes, two processes that are expected to have been active at the landing site as they have been observed in orbital images (e.g., section 3). Rock texture and morphometry have been related to their origin and the mechanism of emplacement (Binder et al. 1977; Mutch et al. 1977; Yingst et al. 2007, 2008, 2013; Craddock and Golombek 2016).

The shallow subsurface structure of the landing site was also a topic of intensive investigation during landing site selection (Golombek et al. 2017) and is clearly important for the SEIS and HP^3 (section 3). As a result, the geology of the surface and its evolution will be used to infer the subsurface structure. This will also depend on information gathered from the physical properties investigation (section 7). Both of these investigations will be used to characterize the surface structure of the landing site and its relation to the surface geology, geologic evolution and the processes responsible for its formation.

5.4. Comparison to Landing Site Predictions

Evaluation of orbital information during landing site selection led to predictions of the surface characteristics, materials present and the geologic processes responsible for the formation and evolution of the site. During landing site selection for Mars Pathfinder (MPF), Mars Exploration Rover (MER), Phoenix (PHX), Mars Science Laboratory (MSL), their remote sensing properties were compiled (Golombek et al. 1997b, 2003a, 2012a, 2017; Arvidson et al. 2008). After landing, characteristics of the surface were compared to those expected prior to landing (e.g., Golombek et al. 1999, 2005). Specific comparisons included thermal inertia inferences of soil

properties and particle sizes, the albedo and presence of bright dust, rock abundance, slopes, and radar inferences of bulk density and roughness. At MPF, PHX and Opportunity specific predictions of the geologic setting (MPF-catastrophic flood depositional plain, PHX-shallow ground ice, MER, Opportunity-presence of hematite) were found to be correct with information collected after landing. Measurement of rocks from shadows in orbital HiRISE images (Golombek et al. 2008b, 2012b, 2017) and size-frequency distributions can also be compared with rock measurements from the surface (Golombek et al. 2008b, 2012b). Specific predictions that have been made regarding surface characteristics, surface materials and their properties and the geologic processes responsible for their formation and evolution at the InSight landing site and tests that can be done after landing to confirm or reject these predictions are described in section 8. The physical properties investigation (section 7) also addresses some of these topics.

5.5. Thermophysical Properties

Thermal inertia values on Mars can be interpreted in terms of regolith physical properties using analogous laboratory experiments and theoretical considerations. Thermal inertia (Piqueux and Christensen 2011) is defined as $I = (k\rho c)^{1/2}$, where k is the thermal conductivity, ρ is the bulk density of the surface material, and c is the specific heat. The thermal inertia represents the resistance to a change in temperature of the upper 2–30 cm of the surface. While the density and specific heat capacity of geological materials only vary slightly (Neugebauer et al. 1971), thermal conductivity values range over several orders of magnitude and are controlled for the most part by the typical grain size (Presley and Christensen 1997a). As a result, grain sizes can be derived from thermal inertia values, and laboratory experiments have quantified this relationship (Presley and Christensen 1997b). Fine particles change temperature quickly and so have a lower thermal inertia, whereas larger particles, have higher thermal inertia. Numerical modeling at the regolith grain

scale have also been used to understand regolith density variations (Piqueux and Christensen 2011). In situ temperature measurements by rovers have been used to derive the thermal inertia of and properties of surface materials (Fergason et al. 2006; Hamilton et al. 2014; Vasavada et al. 2017).

One other factor that may significantly impact the thermal inertia of the Martian regolith is cementation (Jakosky and Christensen 1986). Laboratory measurements (Presley and Christensen 1997a,b,c) and field measurements on Earth (Mellon et al. 2008) have demonstrated that small amounts of pore-filling cements can result in significant increases of thermal inertia values, and numerical theoretical work has quantified this effect (Piqueux and Christensen 2009). The mechanical properties seem similarly impacted, with mildly encrusted samples behaving mechanically like harder rocks (Piqueux and Christensen 2009).

The presence of rocks can also impact the interpretation of thermal inertia, even though rock abundance does not control the bulk thermal properties from orbit (Nowicki and Christensen 2007). Leveraging the large temperature contrast between rocks and fines during most of the Martian day and night, multi-wavelength observations can be used to deconvolve the contribution of various end-members and yield a rock abundance and fine component properties (Christensen 1986; Nowicki and Christensen 2007; Bandfield et al. 2011). Similarly, in the case of rovers and landers, the knowledge of the rock (or bedrock) areal fraction where temperatures are determined can be used to estimate the contribution of fines to the measured radiances, and help derive their thermal properties (Golombek et al. 2003b; Vasavada et al. 2017), resulting in a "rock-free" (or "fine-free" if the properties of rocks are assumed) derivation of the local thermophysical properties (similar to the fine component end-member derived from multi-wavelength analysis).

5.6. Eolian Features and Activity

Mars' surface marks the interface between geologic and atmospheric processes, which over time have resulted in a surface replete with eolian features (e.g., Greeley et al. 2002). Depositional features include diverse sand dune morphologies (linear, barchan, star) and morphodynamics (transverse, longitudinal, oblique), ripples, wind shadows behind rocks, and wind streaks from craters (Greeley and Iversen 1985). Erosional features include yardangs, which form parallel to the prevailing wind, wind scoured rocks, and ventifacts. Much of our understanding of these features is based on terrestrial observations (Bagnold 1941; Greeley and Iversen 1985) and comparisons between Earth and other planets (Greeley and Iversen 1985). The formation times and spatial extent of these features cover a vast range of scales; from dust devil tracks formed in seconds to kilometer-scale dune fields formed over thousands of years. Some eolian features on Mars are known to be active today, as movement has been observed in time-lapse orbital images (Bridges et al. 2013; Chojnacki et al. 2015), which can be used to infer information about the current wind regime and sediment fluxes. However, caution is required as there are also many examples of inactive or indurated surfaces, which do not necessarily relate to the modern wind field (e.g., Golombek et al. 2010).

For InSight we are primarily interested in small scale features that can be observed with the cameras near the lander and related to in-situ wind measurements. However, regional scale features that can be monitored from orbit are also important as they contain information about the global and regional time-averaged wind regimes, their diurnal and seasonal variability (see Spiga et al. 2018, for an extended discussion on this topic), and how this relates to local wind conditions at the lander site.

Most eolian bedforms in the InSight landing ellipse are observed around fresh, rocky ejecta craters (Figures 10 and 26). Most appear within the crater interior and trapped against the ejected

rocks and crater rim. The majority appear bright, suggesting a coating of dust and recent inactivity. They lack clear sand dune morphology and appear similar to ripples observed by Spirit, Opportunity and Curiosity with a surficial layer of coarse granules and poorly sorted interiors. Bedforms and rocks are largely absent in the inter-crater regions, implying that rock and sand production, as well as recent sand mobilization and deposition, are limited to impact-proximal regions (Figure 26). Dust devil tracks are common in HiRISE images with a dominant northwest trend (Figure 11)

FIG 26. One-hundred meter diameter rocky ejecta crater, showing eolian bedforms both inside the crater and in the ejecta blanket. The brightness of the bedforms suggest they are dust covered ripples. The northeast-southwest orientation and preponderance along the northwest margin of the crater suggest formative winds from the northwest (see also Figure 10, which is also the dominant trend of dust devil tracks (see also Figure 11). Notice the relative lack of bedforms and rocks in the Smooth terrain away from the crater (left side of image). Portion of a HiRISE image at 25 cm/pixel in landing ellipse.

The formation of eolian features critically depends on the ability of the wind to lift small particles from the surface. This is essential for the formation of eolian erosional and depositional features, which requires a mobile sediment source and a significant increase in the abrasive power of the wind to form erosional features. The wind stress at the surface σ determines this transport and is given by:

$$\sigma = \rho u_*^2 \qquad (2)$$

where ρ is the atmospheric density and u_* is the friction velocity. The friction velocity depends on the near surface wind profile and, assuming the simplest model for surface-atmosphere momentum exchanges, can be estimated from the scaling relation:

$$u(z) = \frac{u_*}{\kappa} \ln \frac{z}{z_0} \quad (3)$$

where $u(z)$ is wind velocity at distance z above the surface, $\kappa = 0.4$ is the Karman constant, and z_0 is the roughness length (Monin and Obukhov 1954). If the near surface wind profile can be measured for at least two heights then u_* and z_0 can be determined. Such a measurement was possible using the Pathfinder rover's windsock experiment, which had three windsocks mounted on a mast at 33, 62, and 92 cm above the solar panels (Sullivan et al. 2000). This gave a value of z_0~3 cm for the Pathfinder landing site (Sullivan et al. 2000). The InSight landing site is considerably smoother (Sutton et al. 1978; Murdoch et al. 2017a,b; Teanby et al. 2017). In the aerodynamic roughness length map inferred from orbital measurements by Hébrard et al. (2012), the InSight landing site is characterized by values of z_0 ~ 0.1 - 0.25 cm. IDC images will be used for assessing surface roughness, grain size distribution, and hence for estimating z_0 in the vicinity of the lander site.

To lift particles from the surface, the wind shear stress at the surface must exceed the saltation threshold. Once this threshold is exceeded, saltation can occur resulting in increased sediment transport for bedform creation. The lifting threshold can be estimated by comparing the measured movement of dune field ripples to predictions using GCM derived winds (Ayoub et al. 2014; Runyon et al. 2017). The best fit to observed ripple migration were obtained for a critical stress threshold of 0.01±0.0015 N m^{-2}, which for a typical atmospheric density of 0.02 kg m^{-3} gives a corresponding u_* threshold u_{*t} of 0.7 m s^{-1}. This suggests saltation at the InSight landing site should be initiated for a windspeed of 10 m s^{-1} as measured at the height of the APSS wind sensor.

Turbulence-resolving simulations for the InSight landing site described in Spiga et al. (2018) show that, even when the background wind is lower (5 m s^{-1}), friction velocity u_* larger than 0.7 m s^{-1} might be widespread in the afternoon, as a result of both convective vortices (possibly giving rise to dust devils) and convective gusts associated with convective cells.

The instantaneous particle transport flux τ is given by:

$$\begin{array}{ll} \tau \propto \rho u_*^2 (u_* - u_{*t}) & \text{if } u_* > u_{*t} \\ \tau = 0 & \text{otherwise} \end{array} \qquad (4)$$

in the direction of the wind, so it strongly depends on wind speed. For a unidirectional wind regime and for large sediment availability, the most likely bedform is a transverse dune or ripple, with a bedform strike perpendicular to the wind vector (barchan dunes in the case of limited sediment supply). For varying wind speed and direction, the relationship is more complex (Courrech du Pont et al. 2014). In such cases, the average wind direction predicted by GCMs is often not well correlated to observed dune directions (Greeley et al. 1993; Hayward et al. 2007; Gardin et al. 2012). Recent laboratory experiments, numerical simulations and field measurements have demonstrated that a multidirectional wind regime can produce two dune trends according to sand supply (Courrech du Pont et al. 2014; Gao et al. 2015; Lü et al. 2017). As shown by Courrech du Pont et al. (2014), this is because there are two competing dune growth mechanisms. 1) The bed instability mode: where there is no limit to sand supply (i.e., in transport-limited situations), dunes grow in height selecting the orientation for which the gross bedform-normal transport is maximum (Rubin and Hunter 1987). A modified version of this approach gave an improved match between GCM predicted winds and observed bedform orientations (Sefton-Nash et al. 2014). 2) The fingering mode: where the bed is partially starved of mobilizable sediment, dunes elongate in the direction of the resultant sand flux at their crest. Where dunes grow from fixed sources of sediment, this is the orientation for which the normal-to-crest components of transport cancel each other

(Lucas et al. 2015; Gao et al. 2015). In transition areas from high to low sediment availability, the fingering mode is able to accurately predict the corresponding change in orientation of the dune crests under the same multidirectional wind regime (Fernandez-Cascales et al. 2018).

Many of the important parameters (e.g., u_*, u_{*t}, z_0, wind direction distribution) concerning the interaction of the atmosphere with surface transport and bedform formation are currently poorly constrained on Mars and strongly depend on local conditions. Comparing GCM and mesoscale wind predictions to orbital observations has allowed significant progress, but would be much improved by combined surface wind measurements, saltation thresholds, and bedform observations from a long-lived surface station such as InSight.

IDA onboard the InSight lander offers the opportunity to study the activity of sediment transport (eolian and gravity-driven) in the vicinity of the lander. Knowing the initial conditions and analyzing imaging and wind time series, the eolian transport that occurs at the landing site can be investigated, through: 1) independent derivation of the sediment properties (e.g. Claudin and Andreotti 2006) (grain size distribution, cohesion, avalanche angle), 2) determination of the velocity threshold that initiates the eolian transport (Bridges et al. 2012), 3) measurements of the effect of bedform aspect ratio on the wind shear along the topography of the bedform (Courrech du Pont et al. 2014), and 4) measurements of the sediment flux at the landing site and any seasonal variations (Ayoub et al. 2014). All of these parameters are still unknown or largely debated, but are fundamental for the understanding of sediment transport and bedform dynamics on Mars. Additionally, this science activity will be used in order to assess the saltation noise that will possibly affect the SEIS experiment.

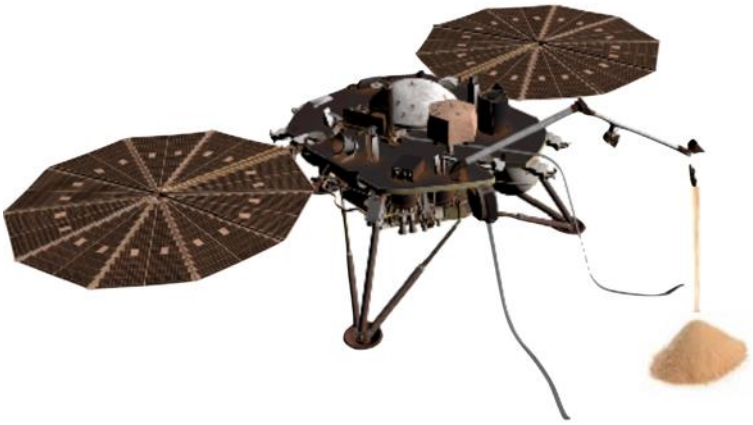

a

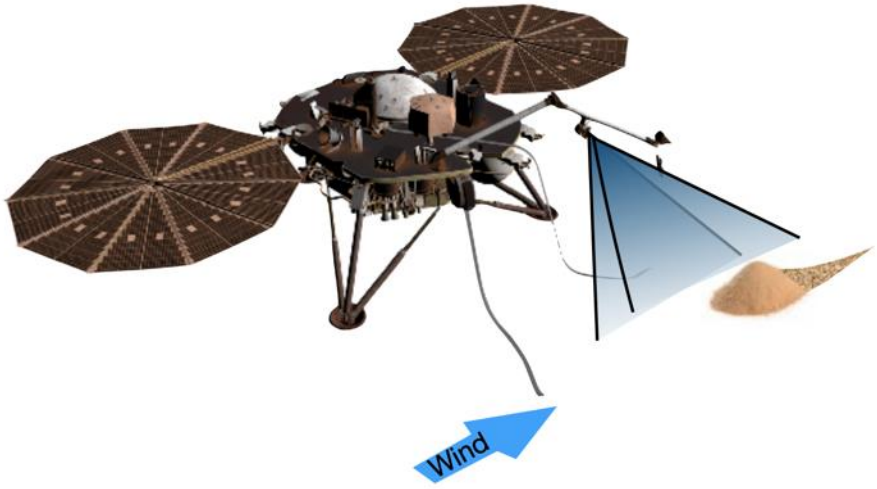

b

Figure 27. a) Sketch of a sand pile created with scoop and b) after wind altered the pile.

In addition to potential bedforms that can be monitored by the cameras, the IDA can be used for specific experiments related to sediment transport investigations. IDA can be used to generate sand/soil piles of different size and aspect ratios next to the lander (Figure 27). Those piles could be monitored with the cameras for generating time series of the piles and their immediate surroundings. Ideally the evolution of the shape of the piles may be tracked by taking stereo images at regular intervals or when the wind blows. Depending on the wind activity (as

measured by APSS), if a sand pile were to migrate away from the lander, a second pile could be created with IDA. Wind data can be collected and combined with the camera images for time lapse monitoring of changes.

InSight will be uniquely suited to monitor the winds that might produce surface changes in that the wind sensors will be taking data continuously. If surface changes are detected, a complete record of the true peak winds that occurred during the interval containing the changes can be acquired, which will help establish an empirical threshold friction wind stress for grain motion. The area near the lander where imaging can detect subtle changes in surface topography can be used to identify changes to best constrain the threshold friction wind speeds (and through the estimated surface roughness, the threshold wind stress). Based on prior experiences with the MER rovers, MSL and Pathfinder, eolian change may not be a rare event, but may be seen on the natural topography and probably even more readily on soil piles produced with the IDA that may be near the angle of repose. Stereo imaging sequences with the IDC will yield DEMs in the near vicinity of the lander (i.e., the workspace) with resolutions on the order of ~1 mm spatially and elevation postings of ~5 mm.

From existing state-of-the-art atmospheric models (global climate and mesoscale models), the wind direction at the InSight landing site is predicted to be seasonally variable, with directions dominated by south-easterly, north-westerly and southerly wind directions. Taking into account the fact that multidirectional wind regimes would develop as a result of diurnal and seasonal variability of near-surface winds, transport modeling fed with Global Climate Model predictions indicates that wind originates from the northwest (~38-60° counterclockwise from north), with possible large departures to this prediction should the sediment supply be severely limited (details and references provided in Spiga et al. 2018). This is broadly consistent with the northeast

orientation of eolian bedforms inside craters, the preponderance of bedforms to the northwest of fresh rocky ejecta crater rims and the dominant northwest trend of dust devil tracks. Both the wind directions and bedform orientations can be verified, by measuring small ripples, small dunes, or modifications to regolith piles created by the scoop and rock wind shadow deposits.

5.7. Surface Alteration and Changes

5.7.1. Albedo Increase with Dust Deposition

Dust removal during landing will increase the surface albedo (e.g. Daubar et al. 2015), thus changing the surface energy balance (Plesa et al. 2016). The resulting surface cooling will cause an instantaneous drop of the average daily surface temperature, and this signal will slowly diffuse into the subsurface, temporarily increasing the subsurface thermal gradient. This will need to be taken into account when inverting HP^3 data taken at depths down to 3 m below the surface, but deeper temperature readings should remain unaffected. In addition, the speed with which the perturbation travels into the subsurface holds clues to the regolith thermal diffusivity, which is defined as $\kappa = k/\rho c$, where k is thermal conductivity, ρ is density, and c is specific heat. As thermal conductivity is directly measured by the HP^3 instrument and c can be considered to be reasonably well constrained, the temperature response to the sudden cooling caused by dust removal can likely be interpreted in terms of the average regolith density.

5.7.2. Dust Deposition on Solar Panels

Dust has been observed to be deposited on the solar panels of all solar powered landers and rovers on Mars. On Mars Pathfinder, The Mars Adherence Experiment was designed to measure the rate of settling of dust onto the solar arrays and found accumulation of 0.28% per day, which also corresponded to the decrease in solar power generated by the arrays (Landis and Jenkins

2000). Both Mars Exploration Rovers also experienced dust deposited on their solar panels that correlated with changes in dust opacity in the atmosphere (Stella and Herman 2010; Vaughan et al. 2010). Because MER also measured the atmospheric opacity (Lemmon et al. 2004), the amount of dust on the solar panels (the dust factor) was also derived (Stella and Herman 2010). These data recorded differences in dust cleaning events between the rovers that are likely due to wind vortices or dust devils (Lorenz and Reiss 2015). Phoenix similarly recorded dust deposition onto the spacecraft from the atmosphere (Drube et al. 2010). InSight will measure atmospheric opacity with the IDC and so will be able to determine the amount of dust on the solar panels similar to MER.

5.7.3. Dust Devils

Reiss and Lorenz (2016) reported a survey of dust devil tracks in the Elysium Planitia landing region for InSight and noted that the observed tracks tended to be considerably smaller (<10 m width) than those measured by Verba et al. (2010) at the Gusev site (mean width ~56 m) for Spirit, even though both sites have similar dust cover (Golombek et al. 2017). On the other hand, dust devil tracks were not observed at the Curiosity landing site at Gale crater.

Crudely equating dust devil activity with evidence of tracks (an imperfect association, since visible track formation depends on the presence of a thin dust layer that can be removed by a vortex, as well as on the vortices themselves) suggests that InSight will observe dust devil activity intermediate between Spirit (which observed many dust devils) and Curiosity, which has observed relatively few (e.g., Moores et al. 2015). The track formation rate of between 0.002 and 0.08 tracks per square kilometer per sol, coupled with the observed lengths and widths, suggests that track-forming (and by analogy, solar-panel-clearing, Lorenz and Reiss 2015) vortex encounters with a lander may have a recurrence interval of some years (much longer than the couple of hundred days

encountered by Spirit). It may be that solar power degradation by dust accumulation on InSight's solar arrays is not mitigated by dust devils as often as was the case for Spirit.

In general, dust devil tracks are rather straight, suggesting motion dominated by a prevailing wind, or meandering or even looping (cycloidal). It seems probable that this property (sinuosity – the ratio of the along-track length to the straight-line start-to-end distance) may be indicative of typical wind conditions. The tracks studied by Reiss and Lorenz (2016) were predominantly straight, and have a rather narrow azimuth distribution (northwest/southeast) suggesting that winds are relatively strong and uniform in direction when dust devils form. This consistent migration direction may permit strategies for dust devil detection by imaging to be optimized for maximizing counts of overall activity (looking upwind) if images are limited due to data volume constraints. On the other hand, if many images can be taken, looking orthogonal to the wind would maximize information on size, miss distance and migration rate for individual encounters. These parameters would be useful in interpreting geophysical signatures of dust devils (e.g., the stiffness of the ground from the elastic deformation induced by the negative load of the passing vortex, e.g. Lorenz et al. 2015 and section 7.4).

5.7.4. Images for Change Detection

Repeated orbital images will benefit several different InSight investigations. The 25-cm/pixel scale and excellent signal to noise ratio of HiRISE (McEwen et al., 2007) on MRO, is capable of detecting changes at scales comparable to those able to be investigated by the lander. Specifically, eolian bedform migration near the lander detected from orbit can be ground-truthed with images from InSight cameras. The albedo of the landing site will be monitored from orbit for fading of the landing-induced darkening (e.g., Daubar et al. 2015), and observed by the lander's cameras allowing comparison between orbital and ground-based images. Dust devils passing close

to the lander are expected to be detected with the lander instrumentation as well, so orbital images will also be searched for the appearance of new dust devil tracks (or perhaps even a dust devil itself).

6. Cartography

6.1. Inertial-Cartographic Tie

Reconstruction of the location of InSight after landing and RISE tracking will yield a superb tie between the cartographic and inertial reference frames and the best know position on the surface of Mars. Previous landers have provided ties between their location with respect to surface features (cartographic frame) and their location with respect to inertial space (e.g., Golombek et al. 1997a, 1999a,b; Arvidson et al. 2004a,b). Since the Mars Orbiter Laser Altimeter (MOLA) updated the Mars cartographic frame (positive east planetocentric coordinate system referenced to the IAU/IAG 2000 frame, which is compatible with the inertial coordinates used by spacecraft navigation teams, Smith et al. 2001), localization after landing by the Mars Exploration Rovers (MER) has shown that the tie between the two frames is roughly 100-300 m (Arvidson et al. 2004a,b).

In the past, the largest uncertainty in the relation of cartographic positions and inertial coordinates has been in the correlation of the reference longitude and the rotation angle ϕ (from equation 1) at a reference time, designated ϕ_0, where the reference epoch is 01-Janaury-2000 @ 12:00. With the longitude origin defined by the center of the crater Airy-0, the accuracy of ϕ_0 has been limited by the resolution of camera images of the crater and by uncertainty in the pointing direction of the cameras with respect to inertial space. This has resulted in uncertainty in ϕ_0 corresponding to uncertainty in surface feature position of ~100 m in the direction of increasing longitude. In contrast, the longitude of Mars landers determined by radio Doppler measurements

have had internal consistency at less than 10 m. Therefore, recently the IAU Working Group on Cartographic Coordinates and Rotational Elements has adopted use of the longitude of the Viking 1 lander as defining, with a value as consistent with the center of Airy-0 being zero as close as currently possible (Kuchynka et al. 2014). Because the Viking 1 lander position has been determined both with radio Doppler and imaging, it provides a good reference to tie Mars fixed positions relative to features. A new IAU model for rotation from Mars-fixed to inertial coordinates has been developed consistent with that definition and with the most recent Mars lander and orbiter data (Jacobson et al. 2018).

After landing, reconstruction of entry, descent and landing (EDL) from spacecraft (section 6.2) and early RISE tracking (section 6.3) will be used to determine the location of the lander in inertial space. The lander will also be imaged by HiRISE, which allows a determination of its location in cartographic space (section 6.4). Each of these methods is described below.

6.2. EDL Reconstruction

The Entry, Descent, and Landing (EDL) team will produce a final pre-entry estimate of the landing ellipse several hours prior to entry. This estimated landing ellipse will be approximately 100 km x 25 km primarily due to residual uncertainty in the navigated state of the spacecraft as it approaches Mars as well as uncertainty in the vehicle aerodynamics and the Martian atmosphere. Immediately following landing, one of the first reconstruction tasks facing the EDL team will be to estimate the landed position of the vehicle.

An initial estimate of landed position will be generated by combining estimated navigation errors with an onboard inertial position estimate generated by onboard propagation of inertial accelerations measured by the Inertial Measurement Unit (IMU). This estimate is expected to be within 1 km of the actual landed location on the surface. For MSL, this technique yielded a result

that was within 105 m of the landed location. The initial estimate will be available about one hour after spacecraft data acquired during EDL is made available to the EDL team. If MaRCO (Mars Cube One communication relay satellites launched with InSight) return data, it will be available in real time and EDL will nominally have an initial landed position estimate within an hour of landing. Without MaRCO, EDL data will be received about four hours after landing via recorded playback from MRO and/or Odyssey and EDL will nominally have an initial landed position estimate within five hours of landing.

6.3. Early RISE Location

The radio Doppler data provided by the RISE experiment will help determine the inertial position of InSight soon after landing. Thirty minutes of Doppler data will be acquired on the first sol after landing, followed by 30 minutes on the second sol. These data are sufficient to determine the lander longitude and distance from the spin axis, R_S, with accuracy of about 20 m (or about 0.0004° in longitude) (Le Maistre et al. 2012). The distance from the equator, R_Z, and hence the latitude, is not well determined from Doppler data given that the rate of change of distance (equation 1) is predominantly due to the Martian diurnal rotation and is not dependent on R_Z.

Some previous landers have used radio range measurements to Earth to determine the R_Z with accuracy ~20 m (e.g., Kuchynka et al. 2014). However, InSight is not planning to take range data, instead maximizing signal power for Doppler and telecommunications. An alternative method for determining R_Z is to combine the Doppler data with topography (Le Maistre 2016). This basically consists of using the estimates and uncertainties of the lander coordinates in the equatorial plane, λ and R_S from the Doppler data to determine the range of possible R_Z values such that the lander is on the surface of the planet, as defined by the topography.

By combining the first two days of Doppler data with knowledge of the topography, R_Z will be determined with 250 m accuracy from combining the 20 m uncertainty in the equatorial coordinates from the first hour of Doppler data with surface topography with 500 m resolution (from the gridded MOLA elevations, Smith et al. 2001). This allows determination of the latitude with accuracy 0.004°. A better estimation of R_Z could be obtained from Digital Elevation Models of higher precision and spatial resolution such as those derived from Mars Express HRSC (Gwinner et al. 2010) and MRO-CTX/HiRISE (Fergason et al. 2017), which have been produced for the InSight landing site (Golombek et al. 2017).

6.4. Cartographic Location

The determination of the location of the lander with respect to cartographic features will be determined by either imaging the spacecraft on the surface with HiRISE and/or identifying common features that can be seen in both surface and orbital images. The Pathfinder lander was initially located by drawing azimuths to streamlined hills and crater rims that could be identified in Viking images (Golombek et al. 1997a, 1999a,b). The MER rovers were located in EDL camera and Mars Orbiter Camera images and features seen in surface images (Arvidson et al. 2004a,b). Phoenix and Curiosity were both imaged directly by HiRISE (e.g., Parker et al. 2012, 2013).

InSight will be located in cartographic space by imaging the spacecraft directly with HiRISE. Current plans are to provide inertial landing coordinates to the HiRISE team from either EDL reconstruction (section 6.2) and/or early RISE tracking (section 6.3) for imaging as soon as orbital passes allow. HiRISE images are 5 km wide, so initial inertial locations should be accurate enough to image the lander on the first try. Once a HiRISE image is acquired, the image can be georeferenced onto landing site maps, which have been georeferenced in a pyramid starting with

MOLA elevation maps, 463 m/pixel; HRSC, 12.5 m/pixel; CTX 5–6 m/pixel; and HiRISE ~0.25–0.3 m/pixel images (Golombek et al. 2017) to determine the cartographic location of the lander.

6.5. Final RISE Location

By the end of the InSight mission, the cumulative Doppler measurements for RISE will determine the position in the equatorial plane very accurately. The uncertainty in the distance from the spin axis, R_S, will be 2 cm, about 5 times better than for any previous lander. The uncertainty in longitude will be about 2 m, or about 0.00003°, limited mainly by uncertainty in the Martian rotation rate times the 40 years from the time of the Viking lander to the InSight landing date given that the Viking lander longitude is currently used to define the Martian longitude system. If InSight is chosen to become a new reference for longitude, then future landers will be able to have longitude determined to 2 cm accuracy. The distance from the equatorial plane, R_Z, will be known to ~1 m accuracy from the combination of the Doppler data and topography, corresponding to a latitude uncertainty of 0.00002°.

7. Physical Properties Investigation

7.1. Physical Properties of Surface Materials

The physical properties of soils, such as thermal conductivity, dielectric constant, seismic velocity, compressibility, shear strength, and penetration resistance depend on its bulk density, which depends on the grain size distribution, grain roundness and angularity, void ratio, porosity, and particle arrangement (Carrier et al. 1973). Bulk density affects all mechanical properties, including the elastic parameters (Young's modulus, E, the shear modulus, G, and Poisson's ratio, ν). As an example, the Young's modulus of loose Hostun sand (France) determined from triaxial tests at 0.1% axial deformation range ($D_r = 0.14$, bulk density $\rho = 1392$ kg/m^3) is between 10 MPa

under a confining stress of 20 kPa, and 30 MPa under 100 kPa. If dense (D_r = 0.88, ρ = 1721 kg/m^3), it ranges between 16 MPa (under 20 kPa) and 46 MPa (under 100 kPa) (Lancelot et al. 1996), which shows the stress dependency of the Young modulus in granular materials. Note also that the elastic modulus of sand is strain dependent, with higher values at low strains (Atkinson and Sallfors 1991). In this regard, the elastic shear modulus governing the propagation of elastic waves (strains smaller than 10^{-3} %) in sand is significantly higher than that governing the interaction of instruments (SEIS, mole or scoop) with the ground (strains larger than $5x10^{-2}$ %).

Once elastic deformation is exceeded by the stress field applied (around the mole during penetration or during scoop operations, for instance), irreversible plastic deformation occurs, with changes in the arrangement of grains. Depending on the bulk density, sand submitted to shear may either contract (loose sands) or expand (dense sands), prior to failure. As a consequence, penetration is much easier in loose sand than in dense sand. Finally, when failure occurs in cohesionless sand its geometry is controlled by the angle of internal friction, which depends on the bulk density.

The most common failure criterion used for granular materials is the Mohr-Coulomb criterion (Holtz and Kovacs 1981). This criterion is defined by the angle of internal friction, ϕ, and cohesion, c, when the grains are bonded together. The friction angle defines a linear relationship between shear failure and the confining pressure of a granular material. As an example, Lee and Seed (1967) measured a friction angle ranging between 34° (at a density of 1440 kg/m^3) and 41° (at 1680 kg/m^3) for rounded Sacramento river sand. The friction angle can be related to the angle of repose for cohesionless materials. In granular materials in which some bonding has developed between the grains, the cohesion is a constant that is independent of the confining pressure. These failure parameters are dependent on the state of the regolith including relative density, particle size

distribution, roundness, angularity, cementation and many other properties. Subsequent sections detail experiments for the InSight mission to capture elastic and failure properties of Martian surface materials. Basic soil parameters of martian surface materials have been derived from all previous landed missions (e.g., Christensen and Moore 1992; Herkenhoff et al. 2008), either by interaction of arms on Viking (Moore et al. 1987) and Phoenix (Shaw et al. 2009) missions, or by interaction of rover wheels with the surface soils by the MPF (Moore et al. 1999), MER (Arvidson et al. 2004a,b; Sullivan et al. 2011) or MSL (Arvidson et al. 2014).

7.2. Simulants

Earth simulants have been used to conduct laboratory tests to constrain the likely physical properties of soils on Mars in preparation for the InSight mission (Delage et al. 2017). These tests include one dimensional compression, shear and measurement of seismic P- and S-wave velocities and have been compared to other terrestrial sands and their physical properties. Two materials used in the tests bound the likely size distribution of soils on Mars and include: a mix of Mojave Mars Simulant (MMS, Peters et al. 2008), which is crushed Miocene basalt, with alluvial sedimentary and igneous grains from the local area, and Eifelsand simulant, which is a mix of crushed basalt and volcanic pumice sand. The behavior of a finer Mars Soil Simulant-Dust (MSS-D, Becker and Vrettos 2016), which is an equal mix of crushed olivine and quartz sand with a bimodal grain size distribution curve with one mode smaller than sand (powder), was also investigated.

Unlike lunar regolith, which is composed of angular particles due to impact comminution from basin size to single atoms, sand on Mars is generally rounded because the smallest impacts are filtered out by the atmosphere (e.g., Paige et al. 2007) and sand grains are mobilized by the wind and saltation rounds the grains (e.g., McGlynn et al. 2011; Goetz et al. 2010; Minitti et al.

2013; Ehlmann et al. 2018). As a result, shear tests carried out on lunar regolith (Scott 1987) or lunar regolith simulants (JSC-1 simulant or other crushed basalts, e.g., McKay et al. 1994; Alshibli and Hasan 2009, Vrettos 2012, Vrettos et al. 2014) may not be entirely relevant, given that the highly angular shape of their grains results in larger friction angles. Note also that some Mars regolith simulants, like JSC Mars 1 (Seiferlin et al. 2008), which is based on mineralogical similarity and made up of weathered volcanic ash also has irregular grain shapes, and thus could have a different mechanical response from sand with rounded grains. In this regard, simulants based on quartz sand on Earth (e.g., WF34, Lichtenheldt et al. 2016), which is typically rounded by fluvial, marine and eolian activity, may be mechanically more representative of soils on Mars that are dominated by rounded and equant basaltic sand grains.

7.3. Physical Properties from HP^3 and Mole Modeling

As outlined in Sec. 2.3., the penetration progress achieved by the HP^3 mole per stroke depends on the mechanical properties of the regolith, and mole progress can be interpreted in a way similar to dynamic penetrometer measurements or a pile-driving process. To translate the penetration speed to a mechanical soil parameter like the angle of internal friction ϕ and density ρ, different types of models can be used. In the simplest form, analytical models can be used to couple energy input into the soil with a soil mechanics model, but more realistic models consider the detailed action of the mole hammering mechanism (Lichtenheldt et al. 2014) together with the soil's mechanical response. The latter may be treated by either soil physics models (Lichtenheldt and Krömer 2016, Kömle et al. 2015, Poganski et al. 2017b) or Discrete Element Models (DE Models, see Lichtenheldt et al. 2014, Lichtenheldt 2015, Lichtenheldt 2017 and pogan et al. 2017a), which are, however, computationally demanding. Therefore, DE Models will only be used

for the detailed study of single or few hammering strokes. The DE Model is a particle based method that can simulate the dynamics of the interaction of the mole with the surrounding regolith and thus provides mole penetration progress and force profiles at various depths. These force profiles can be used as input to pile driving (Poganski et al. 2017a) and soil physics (Lichtenheldt and Krömer 2016) models, which can simulate the entire penetration of the mole. The DE Models are either calibrated by tuning properties to standard laboratory tests using a quartz sand simulant (Poganski et al. 2017a), or by using a direct, systematic identification strategy (Lichtenheldt 2015) on quartz sand (WF34, see Lichtenheldt 2016).

To initialize a DE Model a volume is filled with particles at an assumed packing density. The depth of the simulation volume is either determined by a layer of coarse particles with a weight corresponding to the overburden pressure for this depth at the local gravity (Poganski et al. 2017b) or by retaining the overburden pressure by loading and deleting particles (dynamic boundaries, Lichtenheldt 2017) as the mole is driven into the soil. The overburden pressure is then retained by fixing the boundary particles. The body of the HP^3 mole is then either progressing from the top of the volume (surface penetration) or is embedded within the volume for deeper layers (Figure 28). The hammering mechanism is implemented either using four masses simplifying the hammering mechanism (Poganski et al. 2017a) or using a complex, enhanced multi-body model of the mole hammering mechanism (Lichtenheldt et al. 2014; Lichtenheldt 2017).

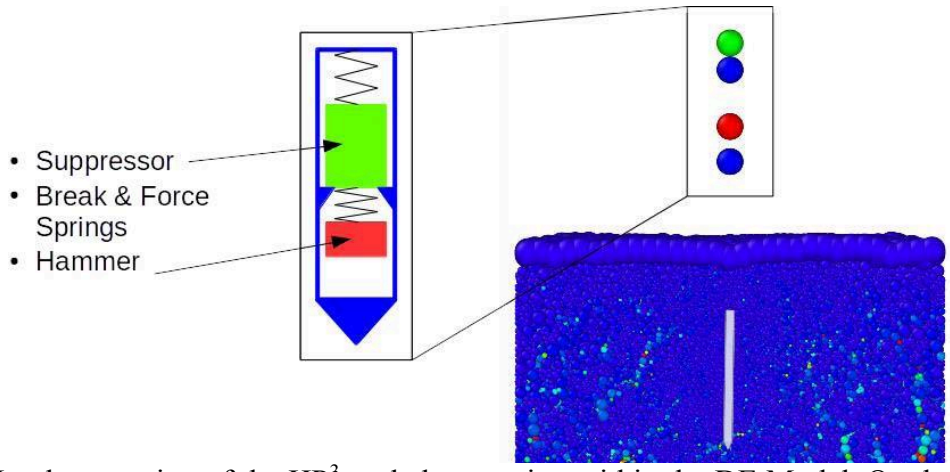

Figure 28. Implementation of the HP^3 mole hammering within the DE Model. On the left side of the panel a schematic representation of the mole hammer mechanism shows the hammer mass (red), the support mass above it (green) and the mole housing (blue). The hammer and support mass are connected by springs that can transfer energy to the mole housing. On the upper right side is the corresponding implementation of the hammer mechanism within the DE Model. The hammer model is rigidly connected with the mole body in the soil model (lower right panel). Thus a more realistic hammer force can be computed from the interaction of hammer mechanism, mole body and the surrounding soil. The colors in the lower right panel show the residual stress when the mole is not moving, with red indicating a higher stress and blue no stress.

A typical hammering cycle consists of multiple hits by either the hammer or the support mass on the mole casing where the second hit in the cycle is generated by the rebound of the support mass (see Lichtenheldt et al. 2014, Lichtenheldt 2016). For any given depth, the force profile of a hammering cycle can be reproduced with these DE Models. Using the model by (Lichtenheldt 2017) it was also possible to simulate the wave propagation in the regolith caused by the hamming strokes (Figure 29).

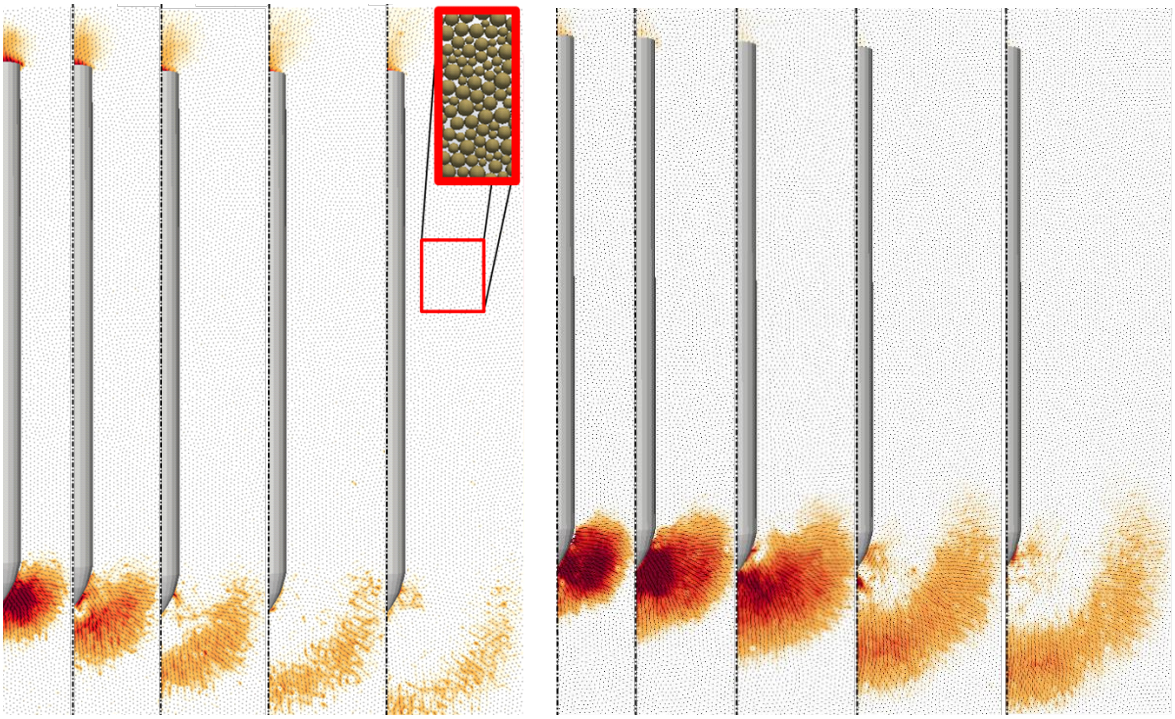

Figure 29. Wave propagation through the soil 2, 3, 4, 6 and 7 ms after the first stroke of the HP^3 mole's hammering cycle on Earth (left) and Mars (right) (Lichtenheldt 2017). The result has been generated by using the model coupling enhanced multi-body dynamics of the hammering mechanism and DE Model presented in (Lichtenheldt et al. 2014, Lichtenheldt 2017; further details in Lichtenhelt 2016). The wave fronts are colored by the interpolated particle velocities. A red and darker color corresponds to faster particles, whereas slower particles are colored lighter red/orange and yellow. Particle velocities in white are below the threshold.

The soil physics models will be used in an approach similar to that of Poganski et al. (2017b) to calculate the model parameters from the physical soil parameters while at the same time taking the mole geometry into account. Given the soil model parameters, coupling of the mole model with the soil model will provide the per-stroke performance of the mole at prescribed depths, from which the overall penetration progress can be reconstructed (e.g., Figure 30).

Due to the complex nature of operating a hammering mechanism inside a non-linear, anisotropic, non-continuous and possibly inhomogeneous soil, a direct inversion of the models for soil parameters is not feasible. Thus, parameter estimation poses an optimization problem, and we

will minimize the error between the measured and simulated progress using ϕ and ρ as free parameters. Both parameters can be assumed to be bound over a reasonable range, but trade-offs between ϕ and ρ exist. In addition, knowledge gathered from laboratory experiments on the relationship of $\phi(\rho)$ (Delage et al. 2107) will help to narrow down the range of admissible parameters, and it should be noted that the progress is much less sensitive to changes of ρ as compared to changes of ϕ. For constant density, inversion of the mole penetration curve could be carried out by fitting the entire depth range simultaneously, but it is expected that parameters will vary with depth. Therefore, we plan to use a stepwise inversion of the penetration curve considering small depth intervals individually. Each depth interval will be considered as a separate optimization problem, and continuity conditions will be imposed to the neighboring sections. In summary, we will thus obtain estimates of density $\rho(z)$ along with estimates of the internal friction angle $\phi(\rho)$ as a function of density. For the pile driving model a parameter tuning approach is carried out to match the mole penetration on Mars.

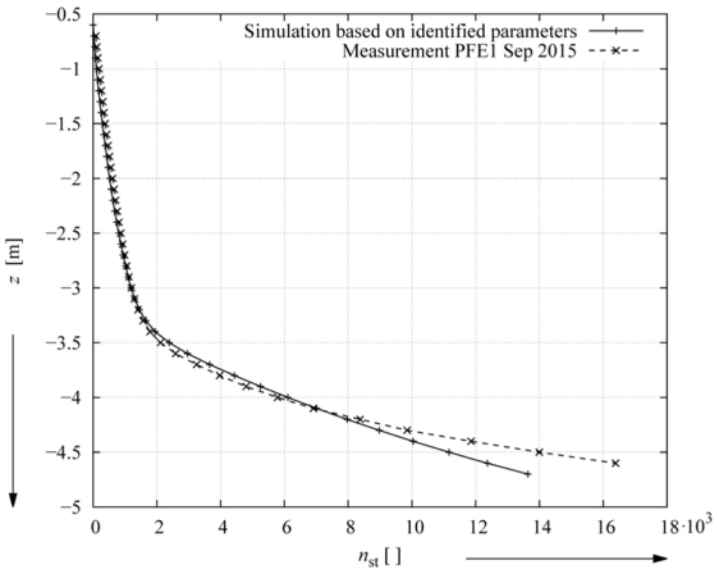

Figure 30: Depth z achieved by the HP^3 mole as a function of the number of hammering strokes n_{st} using the model presented in Lichtenheldt & Krömer (2016). The test was carried out with a

proto-flight equivalent mole model and the simulated profile was calculated using soil mechanical parameters as identified by laboratory tests.

7.4. Physical Properties from Passive SEIS Monitoring

7.4.1. Physical Properties and Regolith Structure

Physical properties of the regolith at the landing site, specifically the seismic velocity profile, can also be constrained by data collected during passive monitoring by SEIS. Constrains on deeper structure from the analysis of seismic signals associated with marsquakes and impacts are developed in Panning et al (2017); this section mostly discusses signals caused by local atmospheric disturbances that might be a significant source of high frequency seismic noise and ground deformation.

As observed in terrestrial field data (Lorenz et al. 2015) and derived from analysis of Large Eddy Simulations for realistic landing site conditions (Kenda et al. 2017), pressure fluctuations associated with dust devils or non-dust carrying convective vortices passing within a few 100 m of a sensitive broad-band seismometer induce measurable tilt at long periods (i.e., < 10 s, Mimoun et al. 2017, Murdoch et al. 2017a). The spectral ratio between this ground tilt and the pressure time series, available from APSS for InSight, depends on the elastic parameters of the sub-surface (Sorrells et al. 1971), with a larger tilt generated for a material with lower rigidity. The frequency-dependent ratio can thus be used to distinguish between different models of sub-surface structure (e.g., regolith thickness) (Kenda et al. 2017).

Seismic velocities and regolith thickness at the landing site can also be derived from observations of high-frequency surface waves above 1 Hz, based on two complimentary approaches. High-frequency seismic signals related to passing dust devils have been observed on Earth (Lorenz et al. 2015) and identified as shallow surface waves (Kenda et al. 2017). Kenda et

al. (2017) have demonstrated that modeling high-energy spectral lines in these signals as multi-mode Rayleigh wave Airy phases (i.e., extrema in group velocity dispersion curves) can constrain sub-surface S-wave velocities. In addition, if the trajectory of the dust devil is constrained, for example by orbital observation of the track, the arrival time difference between surface waves and atmospheric infrasound (Lorenz et al. 2015, Lorenz and Christie, 2015) would constrain the surface-wave velocity, as the sound speed in the martian atmosphere is known (Kenda et al. 2017).

Furthermore, parts of the ambient wavefield that are dominated by Rayleigh waves can be extracted from SEIS recordings and used to measure the elliptical Rayleigh wave polarization by computing the horizontal-to-vertical spectral ratio (Hobiger et al. 2012). As shown by Knapmeyer-Endrun et al. (2017), Rayleigh wave ellipticity of both the fundamental and the first higher mode can be measured for a reasonable model of the landing site structure, and provide additional knowledge of P- and S-wave velocities and layering in the shallow subsurface. If some initial constraints (e.g., from laboratory velocity measurements), orbital regolith thickness mapping (see section 3.5), or analysis of HP^3 seismic signals (Kedar at al. 2017) are available, Rayleigh wave ellipticity inversion can supply information on the thickness and velocities of the sub-regolith layer (Knapmeyer-Endrun et al. 2017). Furthermore, the data can potentially distinguish between a constant velocity in the regolith and a velocity increasing with depth.

The mechanical noise of the lander, transmitted through the ground to the seismometer (Murdoch et al. 2017b), may provide an additional method for determination of the ground physical properties through passive monitoring. As the frequencies of the lander resonances will be related to the ground stiffness under the lander feet, the most promising method for this is likely to be through identification of the frequencies of these resonances. Although many of the lander resonance frequencies of the lander solar panels are all far above the VBB bandwidth (by design),

and many are even above the SP bandwidth, some resonant frequencies may still be observable within the limits of the instrument sampling frequency.

On a global scale, the cut-off frequency of spectra of impact recordings, i.e. the frequency where a sloping asymptote of the acceleration spectral density at low frequencies changes to a flat plateau at high frequencies, can be used to approximate regolith thickness and porosity at the impact site, as it is inversely proportional to the impact shock wave radiation in the regolith. The method has been demonstrated for Apollo lunar data by Gudkova et al. (2011, 2015), and application to SEIS would allow gathering information on regolith properties and their variability away from the landing site (e.g., Daubar et al. 2018).

7.4.2 Elastic properties from LVL Stiffness

Both sensors of the SEIS instrument (VBBs and SPs) are mounted on the mechanical leveling system (LVL), which provides contact to the Martian ground through its three feet. The lengths of the three LVL legs can be adjusted independently to allow for level placement of the sensors at ground tilts of up to 15°. During qualification tests, horizontal resonances of the LVL were observed at frequencies between 35 and 50 Hz, depending on the LVL configuration (Fayon et al. 2018). The resonance frequencies depend on the length of each of the LVL legs, but also on the mechanical coupling between the feet and the ground. The LVL resonance frequencies observed on Mars may thus provide additional information on the physical properties of the top-most ~2-3 cm of soil at the InSight landing site.

To interpret the LVL's structural resonances, a simplified analytical structural model of the LVL has been developed. This model can reproduce the LVL's mechanical behavior (i.e., its resonance frequencies and transfer function), and can be used to infer the strength of the coupling with the ground by fitting the observed resonances. The modeling approach compensates for

inconsistent coupling conditions during seismic acquisition with the short-period sensors (Bagaini and Barajas-Olalde 2007). Four main structural elements characterize the LVL model: one platform and three legs. The mechanical links between the different elements are modeled as springs with strengths derived from mechanical tests on the LVL. The parameter of interest, the foot-ground coupling, is described by the two variables k_v^g and k_h^g, which indicate the stiffness of the vertical and horizontal elastic forces between the feet and the ground.

Tests have shown that this model can correctly describe the eigenmodes and the transfer function of the structure. Its sensitivity to the different model parameters has been studied by changing various parameters such as the mass of the platform, the length of each leg, the stiffness of the springs, the torque between the ground and the legs, and the attenuation coefficient Q of the elastic forces between the legs and the ground.

Simulations with different configurations consistently show that only two of the 21 possible vibrational modes of the LVL (resonances and movements of the structure) have frequencies within the range covered by the SEIS sensors. These two modes correspond to horizontal translations of the platform in X- and Y-direction, respectively, in agreement with the LVL resonances observed in qualification tests. The simulations also show that SEIS, including the LVL and its legs, can be assumed to be perfectly rigid within the frequency band covered by the seismometers, and that the internal mechanical links (i.e., the stiffness of the springs between the platform and the legs in the model) do not affect the resonance frequencies. In contrast, the parameters k_h^g and C_h^g, related to the horizontal elastic force and torque between the feet and the ground, respectively, control the horizontal resonances at frequencies below 50 Hz (i.e., within the range covered by SEIS at its highest acquisition rate of 100 Hz) (Figure 31). The link between these two parameters and the regolith's physical properties (Poisson coefficient ν and Young's

modulus E) can be analytically expressed for the case of a simple circlular plate with radius *a* on a semi-infinite mass (Poulos and Davis 1974):

$$k_h^g = \frac{16(1-\nu)Ea}{(7-8\nu)(1+\nu)}$$

$$C_h^g = \frac{4Ea^3}{3(1-\nu^2)}$$

However, the presence of the cone on the LVL feet complicates the application of these formulas. In this case, more complete expressions that will be derived from additional experiments (Figure 32) are necessary to invert the resonance frequencies in terms of physical properties of the regolith.

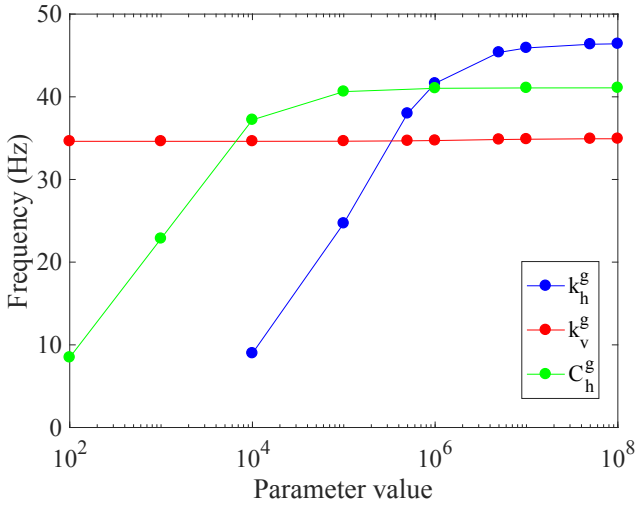

Figure 31. Sensitivity of the LVL resonance frequency to variations in the values of the model parameter describing the elastic stiffness of the material in contact with the LVL feet. Both k^g_h and k^g_v, are in N/m and are related to horizontal and vertical forces, respectively, and the torque stiffness C^g_h, is in Nm/rad, with respect to rotation perpendicular to the vertical.

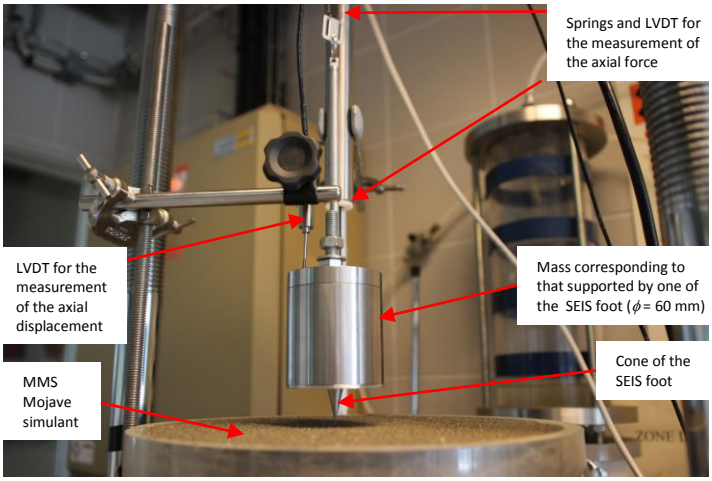

Figure 32. Laboratory penetration tests with the design of the LVL's feet on Mojave simulant, carried out at Ecole des Ponts ParisTech (Delage et al. 2014). The mass of the metal cylinder under Earth gravity corresponds to that supported by one foot of the SEIS under Mars gravity. The angle of the cone has been reduced so as to achieve full cone penetration and full contact of the disk with the regolith under the weight of the SEIS. Both the displacement and force were accurately measured by using a Linear Variable Differential Transformer and, for the force, a spring with adapted stiffness. The cylindrical container accommodating the Martian simulant (MMS Mojave simulant) is placed on the plate of a standard triaxial press that is progressively raised, allowing for progressive penetration of the cone. Parameters $k_g{}^h$ and $C_g{}^h$ were measured once the cone fully penetrated into the simulant, with full contact between the 60 mm diameter disk and the simulant.

7.5. Physical Properties from HP^3-SEIS Hammering

The InSight team has developed a variety of algorithms summarized in Kedar et al. (2017) to use the multitude of HP^3 hammer strokes to extract the elastic physical properties of the shallow sub-surface: P-, and S-wave velocities, Q, as well as the thickness of the regolith layer and possibly even of the shallowest bedrock units. The processing of the HP^3 seismic signals will involve the analysis of the travel-times and amplitudes of the recorded seismic arrivals. As discussed in Kedar et al. (2017), the travel-times of the observed first P- and S-wave phases should enable the determination of the local P- and S-wave velocities from the mole location. The analysis of direct and reflected wave amplitudes and full-waveform inversion may allow increasing the resolution

of the seismic velocity structure to depths below the maximum penetration depth of the mole as well as the extraction of seismic attenuation.

The geometry of the HP^3 experiment with the seismic source (mole) at depth and the receiver located at the surface closely resembles a reverse vertical-seismic profiling (reverse VSP) experiment. Established active seismic-exploration processing techniques can be used to isolate reflections and transform the reflection information into subsurface images. Figure 33 displays the resultant P-wave seismic-reflection image from processing simulated SEIS recordings for the HP^3 experiment. A layered near-surface velocity, density and attenuation (Q) model including interfaces at 5 m marking the transition from fine-grained regolith to coarse ejecta, at 11 m to fractured basalt, and at 24 m to compact basalt, served as input to the finite-element modeling (Figure 33b). Conventional VSP processing steps such as separating the direct waves from reflected waves and Kirchhoff depth migration were employed. In this idealized setting (e.g., noise free data; correct P-wave velocity used for migration), all three interfaces of the input model including the deepest interface at 24 m depth could be resolved (Figure 33c). Multi-component seismic imaging techniques may even allow producing images of S-wave reflections and P-to-S and S-to-P-wave conversions.

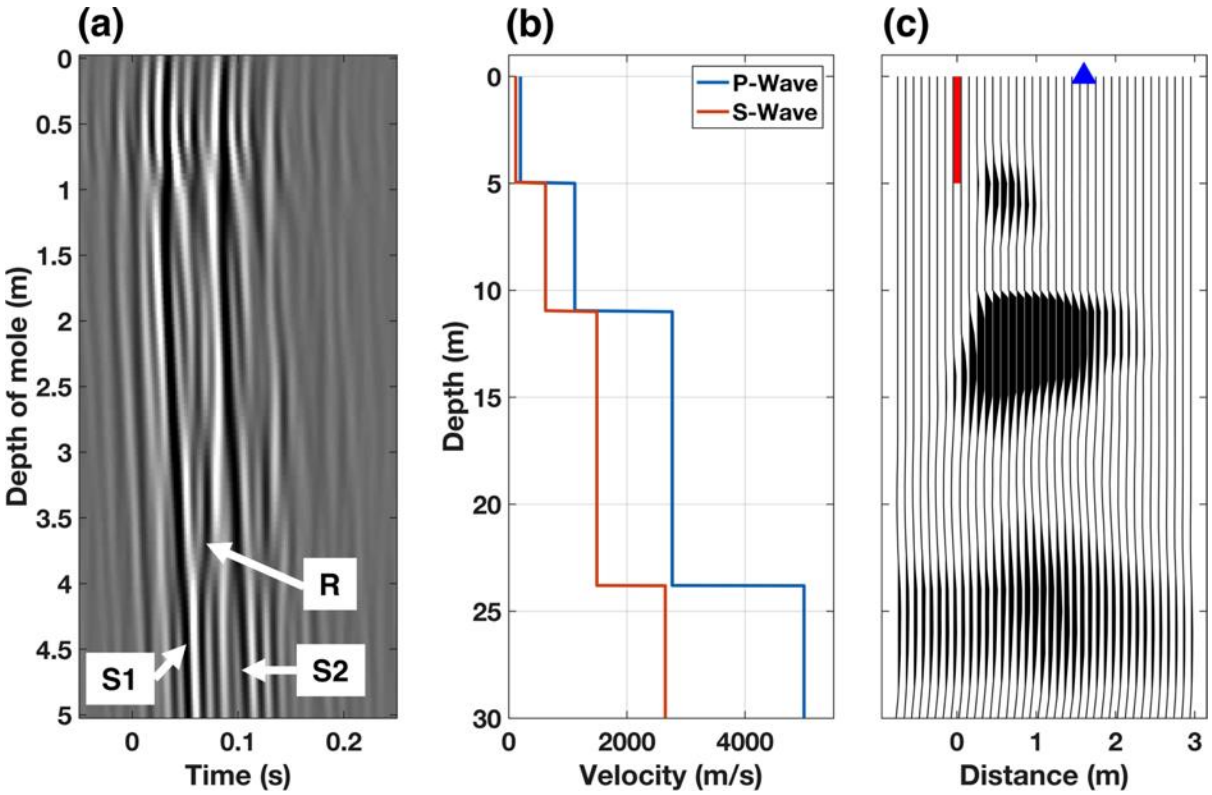

Figure 33. (a) Simulated waveform data for the HP^3 experiment after the reconstruction to 200 sps (see Figure 3). S1 and S2 mark the two hits of one hammering cycle (see Lichtenheldt et al. 2014) and R denotes a reflection. (b) P- and S-wave velocity structure used for the simulation. (c) Final processed seismic-reflection image. The red line marks the trajectory of the HP^3 mole penetrating from the surface to 5 m depth, the blue triangle marks the location of the SEIS instrument and the darker areas are the three interfaces.

7.6. Physical Properties from Arm Experiments

The IDA is equipped with a bucket-like scoop mounted on the end. This scoop can be used in evaluating regolith mechanical properties at the InSight landing site. Specifically, forces acting on the IDA can be monitored via the motor currents in the arm in a similar fashion to mechanical measurements with the Viking and Phoenix lander robotic arms (Moore et al. 1987; Shaw et al. 2009). Additionally, regolith can be manipulated into piles to determine some of its inherent properties. An overview of the proposed experiments is shown in Figure 34. These experiments will be calibrated in a testbed that has been constructed at JPL for InSight activities (Trebi-Ollennu, 2013) and with numerical simulations described below.

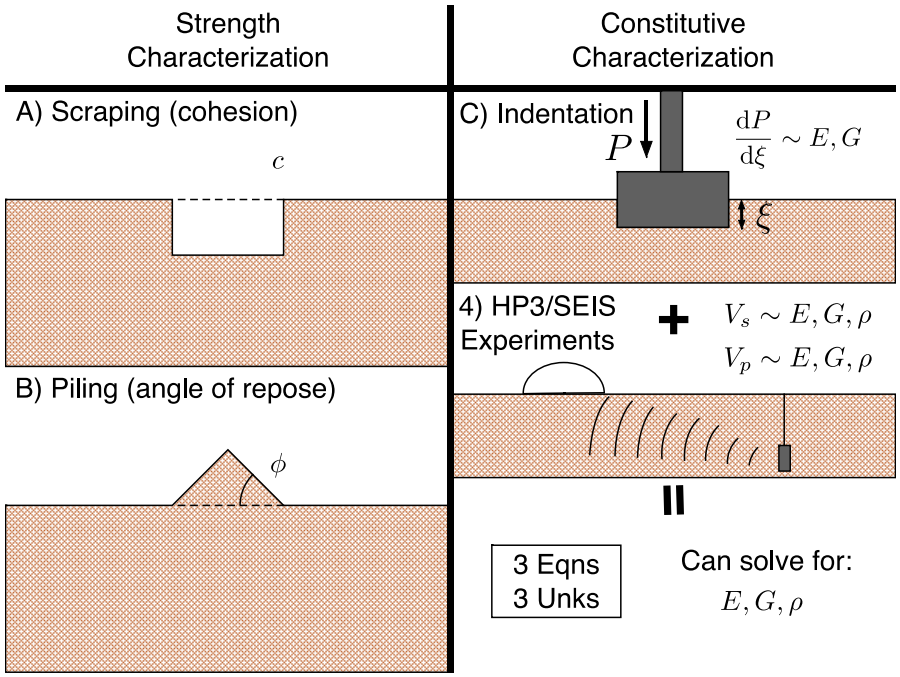

Figure 34: Overview of soil mechanics tests to be conducted with IDA showing A) scraping, B) piling, C) indentation, and HP^3-SEIS hammering.

7.6.1. Scraping and Trenching

The IDA has a scoop attached that can be used to conduct backhoe-style trenching, scraping, and scooping activities at the landing site. A schematic of this activity can be seen in Figure 34. Similar tests were conducted during the Viking and Phoenix mission (Moore et al. 1987; Shaw et al. 2009), which used methods that had been used for lunar soils (Wilkinson and DeGennaro 2007). In that work, force data during scooping operations was measured directly from IDA motor currents. These data combined with relative positioning data during scooping (measured to within 2 mm) for location and scooping depth can directly be used to calculate the cohesion similar to Phoenix (Shaw et al. 2009).

7.6.2. Piling

The material scooped up by the arm during trenching or scraping can also be used to create a pile, which can be observed by the IDA camera. Multiple scoops and dumping procedures will

need to occur to build up the piles high enough for imaging. From these images, the angle of the pile can be directly visualized and calculated. This angle is a direct measurement of a specific friction angle or the angle of repose, ϕ_a (Carrigy 1970; Horstman and Melosh 1989). An example of a pile and the measured angle is shown in Figure 34B. This angle of repose is important for characterizing a regolith and directly relates to other scientific investigations on Mars including the slope of the slip face of sand dunes.

7.6.3. Indentation

In perhaps the conceptually simplest experiment, but most challenging to implement, the flat part of the scoop can be pushed into the ground. This is shown schematically in Figure 34C. Utilizing the IDA's relative positioning and currents, the depth of penetration (ξ) and indentation force (P) can be measured. These quantities are directly related to the elastic constants, Young's modulus (E) and the shear modulus (G), through Boussinesq's formula. We utilize the equations derived by Pharr et al. (1992) and shown in Equation 5.

$$\frac{dP}{d\xi} = \beta \frac{2}{\sqrt{\pi}} \sqrt{A} E_r \tag{5}$$

Specifically, the derivative of the load with respect to the displacement is calculated during the initial elastic unloading phase upon lifting the scoop after indentation. β is the scoop's geometric indentation shape factor (e.g. circle = 1, triangle = 1.034, square = 1.012), which will be calculated for the arbitrary, but specific geometry that works best in the testbed for the IDA. A is the area of the indentation shape. E_r is the reduced modulus of elasticity, which relates regolith material properties (E, ν) to the scoop's material properties (E_s, ν_s) in Equation 6.

$$\frac{1}{E_r} = \frac{1-\nu^2}{E} + \frac{1-{\nu_s}^2}{E_s} \tag{6}$$

The optimal solution for the scoop's punching shape will be selected through testing in the testbed at JPL. When combined with Equations 7 and 8, which are directly calculated from the SEIS and HP3 experiments detailed in previous sections, a system of three equations and three unknowns can be set up to solve for the elastic constants (any 2 of E, G, ν, and λ, Lamé constant) and ρ of the Martian regolith at the landing site. These properties are classic quantities used on Earth for engineering design/analysis and will be particularly useful for future planned missions to Mars.

$$V_P = \sqrt{\frac{\lambda + 2G}{\rho}} \tag{7}$$

$$V_S = \sqrt{\frac{G}{\rho}} \tag{8}$$

7.6.4. SEIS Tilt During Indentation

During indentation experiments the resulting tilt can be measured by SEIS. Using an elastic ground deformation model (as in Murdoch et al. 2017a,b), we calculate that for a 50 N vertical force applied on the ground by the robotic arm scoop, the apparent horizontal acceleration on SEIS due to the tilt is estimated to be 2.3×10^{-7}, 5.0×10^{-7} and 1.7×10^{-6} m s^{-2} at distances of 1.5 m, 1 m and 0.5 m from the closest SEIS foot, respectively. These acceleration amplitudes should be easily detectable by SEIS given the noise level requirement of 2.5×10^{-9} m s^{-2} (Mimoun et al. 2017).

The elastic ground parameters (shear modulus, Poisson's ratio, Young's modulus) can be constrained by solving a system of nonlinear equations derived from the elastic ground deformation model. The inputs would be the measured and known parameters (i.e., the relative position of the three SEIS feet and the lander scoop on the ground, the vertical force applied by the lander scoop, and the resulting tilt of SEIS). In addition to the elastic measurements, if the

ground can be imaged with the IDC before and after the experiment, the observed plastic deformation of the regolith will provide further information on the material strength and porosity.

7.6.5. Numerical Models of Arm Interactions

The same DE Model code discussed in Section 7.3 was used to model the mechanical interaction of the IDA scoop with the regolith (Figure 35). Computational time was reduced by using grains larger than the actual size, while maintaining a similar size ratio to the actual particle size distribution. The scoop was implemented as a geometrically realistic, but simplified mesh model with the motion of the mesh controlled by a script during the model run. Thus, simple actions like indentations or more complex trenching and piling can be modeled. These model runs can deliver two basic types of output. The first one is the force in all three axes acting on the scoop during the soil interaction, which can be directly compared to the force acting on the IDA during operations. Our results in comparison to Phoenix trenching activities (Shaw et al. 2009) yield somewhat higher forces due to a larger depth of penetration. The second output is the redistribution of grains. Thus, trench depths, trench angles, and the angle of repose of piles can be calculated. In future work, more advanced DE Models (Kawamoto et al. 2016) will be utilized to model different particle shapes and the exact scoop geometry.

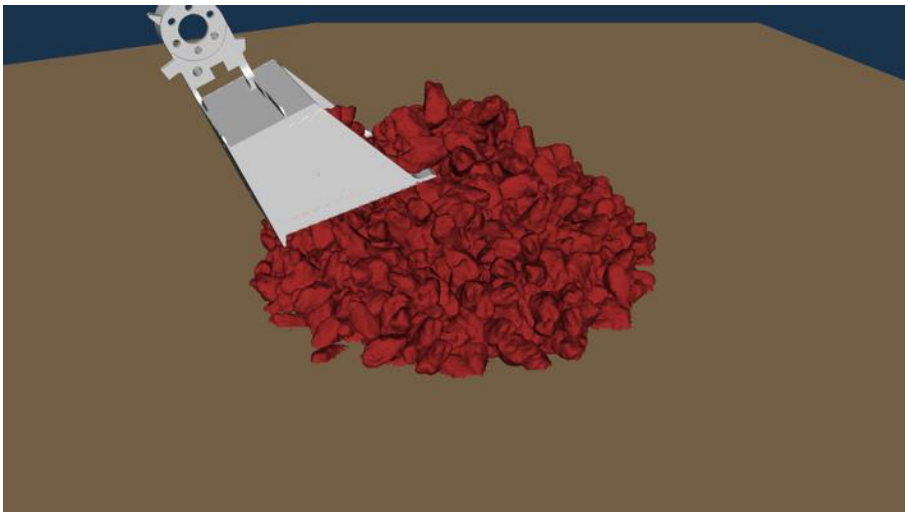

Figure 35: The InSight scoop interacting with granular particles captured from three-dimensional X-ray computed tomography. The exact geometry of the scoop can be replicated in advanced DE Models. These methods can simulate different particle size distributions and particle shapes.

8. Discussion

The results of the geology and physical properties investigations will directly test many predictions of the surface and subsurface that have been made using remote sensing data during the landing site evaluation (Golombek et al. 2017). To first order, comparison of the surface seen from the lander is "ground truth" to the orbital data and interpretations. At the broadest level, orbital observations support a model in which basalts deposited during the Hesperian have developed an impact generated regolith 3-17 m thick that has been modified by eolian processes. The information developed from the geology and physical properties investigations can be used to test this model as well as specific characteristics of the surface, materials present and geologic processes that have modified and shaped or are shaping the surface.

The shallow subsurface model of the InSight landing site was developed from the onset diameter of rocky ejecta craters (Warner et al. 2017), observations of nearby scarps at Hephaestus Fossae (Golombek et al. 2017, Warner et al. 2017), and predictions of fragmentation theory based

on crater counts and rock distributions (Golombek et al. 2017, Charalambous et al. 2017). Knapmeyer-Endrun et al. (2017) used seismic velocities measured in regolith simulants (e.g., Delage et al., 2017) as well as field measurements of soils on top of young basalt flows in the Cima volcanic field in the Mojave desert, where tephra and eolian material grade into a rubble zone of basaltic clasts and then highly fractured rock (e.g., Wells et al. 1985). This produces a step wise rapid increase in seismic velocities, elastic properties and seismic attenuation Q (Knapmeyer-Endrun et al. 2017; Delage et al. 2017). Warner et al. (2017) used the onset diameter of rocky ejecta craters, the depth to the inner crater in nested craters, and roll-offs in the size-frequency distribution of rocky and non-rocky ejecta craters to measure the thickness of the regolith (3-17 m) at the landing site. In addition, fragmentation theory constrained by measured crater counts and rock abundance has been used to simulate the thickness of the regolith at the InSight landing site (Golombek et al. 2017, Charalambous 2005, Charalambous et al. 2017). Finally, the regolith thickness expected from impact gardening of the surface has also been related to the cratering record on the Moon (Oberbeck and Quade 1968) and Mars (Hartmann et al. 2001). These predictions of regolith thickness and elastic and seismic properties of the subsurface can be tested by InSight. The physical properties investigation will constrain the subsurface structure of the landing site using the HP^3 by the penetration of the mole, SEIS monitoring during mole hammering and by passive SEIS monitoring (e.g., Rayleigh wave inversion and other methods). The thickness of the regolith estimated by rocky ejecta craters at the specific landing location, fragmentation theory and impact gardening can thus be compared with measurements made by InSight.

Surface materials at the landing site have been estimated from thermophysical properties and albedo in orbital remote sensing data (Golombek et al. 2017). Surface materials are expected to be dominated by very fine to fine sand that is either cohesionless or has very low cohesion (less

than a few kPa). The albedo, dust cover index, and variations in thermal inertia all suggest the surface has an optically thick but thermally thin coating of dust similar to dusty portions of the Gusev cratered plains. Although the InSight lander carries no imagers capable of resolving sand size grains, other techniques can be used. First, the HP^3 radiometer can determine the thermal inertia at the surface and compare it to that obtained from orbit as has been done by MER and MSL (Fergason et al. 2006; Hamilton et al. 2014; Vasavada et al. 2017). From images of the radiometer spots, the surfaces of the spots can be seen and thus related to the thermal inertia measurements. Specifically, the areal fraction of rocks in the spots can be determined and from the size-frequency distribution of the rocks, the thermal inertia of the rocky component can be estimated and separated from the thermal inertia of the fine component (Golombek et al. 2003b). The thermal inertia of the fine component can be related to the particle size for cohesionless material (Presley and Christensen 1997a,b) and any cohesion via theory (Piqueux and Christensen 2009, 2011) or soil mechanics measurements of soils by the robotic arm. In addition, the elastic properties derived from SEIS and indentation experiments, can be related to simulant properties (e.g., Delage et al. 2017) to see if they are consistent.

Fragmentation theory developed by Charalambous (2015) applied to the InSight landing site based on rock abundances from orbit and surface rock counts from the Spirit and Phoenix landers (Golombek et al. 2017) can be extrapolated to sand size particles (Charalambous et al. 2017), thus allowing a comparison with the observations by InSight. Specific objectives for testing fragmentation theory would be to count the rocks around the landing site in HiRISE and compare their distribution with those measured by InSight as has been done at VL1, VL2, MPF and PHX (Golombek et al. 2008b, 2012b). This would not only provide another example in the model's library, but it would also help quantify better the landing site's maturity index which controls the

abundance of smaller particles. This improved maturity index would help in the re-estimation of mole's probability of success penetrating 3-5 m, together with seismic signals obtained from hitting rocks during the mole's progress, and the final penetration depth. The particle size of the soils inferred from the thermal inertia can also be used to better understand the relative contributions from fragmentation versus eolian activity.

The surface at the InSight landing site is expected to have a thin coating of dust (Golombek et al. 2017). It is expected that surface dust near the lander will be dispersed by the lander retro-rockets as has been observed by Phoenix and MSL (Daubar et al. 2015; Seelos et al. 2014). The dust is expected to be redeposited from the atmosphere over time and the relative albedo can be measured in repeat HiRISE images (e.g., Daubar et al. 2016) and perhaps CRISM with its 18 m/pixel resolution (e.g., Seelos et al. 2014). Surface images can identify pockets of dust by their relatively bright reddish color that might be protected from dispersal by the retrorocket exhaust. Although the imagers do not have individual color filters (Maki et al. 2018), spectra from the Bayer filter blue, green, and red pixels can be used to identify dusty surfaces by their bright reddish color. As a result, surface images can confirm the dusty surface expected in orbital data.

The smooth terrain that the InSight ellipse is mostly located on is expected to be relatively smooth and flat with few rocks. The slopes at several meter and ~100 m length scale were measured in orbital images and DEMs (Fergason et al. 2017; Beyer 2017; Golombek et al. 2017) and surface slopes around the lander from stereo images can be compared with those measured from orbit. Rock abundance is also expected to be low from measurement of shadows in HiRISE images, unless landing is near a rocky ejecta crater (Golombek et al. 2017). In either case, rock size-frequency distributions from stereo images of the surface can be compared with those from orbit (e.g., Golombek et al. 2008b, 2012b; Heet et al. 2009).

If rocks are relatively close to the lander, the texture, fabric and morphology of rocks can provide clues to the rock type (e.g., McSween et al. 1999). The color can be related to their surface visible spectra, with basalts expected to have a relatively low reflectance in the visible (and especially in the red for dust free surfaces, e.g., McSween et al. 2004). The morphometry (shape and roundness) of the rocks observed by the lander can also be related to the depositional and erosional processes that have acted on them (e.g., Garvin et al. 1981; Yingst et al. 2007, 2008, 2013; Craddock and Golombek 2016). Finally, if a small vesicular volcanic rock is nearby the lander and can be pushed by the robotic arm, it might be possible to derive the rock's density and composition (e.g., Thomson et al. 2008).

If landing were to occur close to a crater, the morphology and morphometry of the crater can be compared to that measured from orbit. In addition to rocky and non-rocky ejecta craters in a variety of degradational states (Warner et al. 2017; Sweeney et al. 2016), the most common craters at the landing site are secondary craters from Corinto, a fresh rayed crater about 600 km northeast of the landing site (Bloom et al. 2014), with distinct thermal rays that extend for over 2000 km. The thermal rays are composed of dense swarms of small secondaries and several thermal rays cross the landing ellipse (Golombek et al. 2017). Corinto secondary craters have shallow depth diameter ratios (~0.05) with conical to parabolic shapes and bright ejecta. If InSight landed near a Corinto secondary its morphometry and mophology could be compared to that observed from orbit. Finally, if a small primary crater (~10 cm) is in view of the lander, it can be related to the density of the atmosphere that it survived without ablating completely to impact the surface (e.g., Paige et al. 2007).

Eolian bedforms on the smooth terrain are present around relatively fresh craters where sand size particles have been moved by the wind. Most of the bedforms appear similar to ripples

and are bright in HiRISE images suggesting they are dust covered and thus not recently active. As the craters degrade and fill in, the number and size of the bedforms decrease, suggesting the bedforms transition into a soil unit with slight near-surface cohesion from possible cements left by thin films of water (e.g., Haskins et al. 2005; Hurowitz et al. 2006). As a result, cohesion might be expected in soils of the smooth terrain away from craters. Any bedforms in view by the lander can be related to bedforms seen from orbit and the meteorology data recorded on the lander to compare with wind direction, speed and any changes through time.

9. Conclusions and Summary

Investigations of the geology and physical properties of the surface where InSight lands will be conducted by the color cameras, instrument deployment arm and scoop, the HP^3 mole and radiometer, and the seismometer. The instrument deployment system includes two color cameras, one mounted on an instrument deployment arm that can acquire full color, stereo panoramas, high-resolution images of the surface including the crescent shaped instrument deployment workspace. The IDA has a scoop that can perform basic soil mechanics investigations from calibrated motor currents and surface indentations, scraping, trenching and piling. The HP^3 will measure the thermal conductivity at 50 cm intervals as the mole penetrates 3-5 m below the surface and the penetration rate depends on the soil density, cohesion and angle of internal friction, which can be analyzed by comparing results with laboratory experiments and numerical models. An infrared radiometer can measure the surface temperature of two surface spots to determine the thermal inertia, which can be related to particle size and/or cohesion. Stereo images of the radiometer spots can be used to separate the thermal inertia of the rocky component as well as the fine or soil component. Passive SEIS monitoring of atmospherically generated pressure fluctuations, dust devils or wind vortices, resulting Rayleigh waves, and resonance frequencies of the leveling system and the lander's solar

panels by the seismometer will provide information on the shallow subsurface physical properties. Finally, the analysis of seismic signals from the mole hammering will reveal the near-surface reflectivity structure and elastic-properties that will reduce travel-time and amplitude errors of globally propagating seismic waves. Meteorology instruments will measure pressure and wind speed and direction continuously and thus will record dust devils or wind vortices and peak winds that can be related to imaged dust devil tracks, eolian changes and threshold friction wind stress for grain motion on Mars.

Geologic mapping in medium and high-resolution orbital images indicates the InSight landing site in western Elysium Planitia, just north of the dichotomy boundary, is underlain by basaltic lava flows. Images show a diversity of morphologies, including flow fronts, lobate ridges, inflation plateaus, smooth and platy surface textures, lobate ridges, and vents suggesting low viscosity flows erupted in the Early Hesperian. The plains surface was deformed by wrinkle ridges, which have been interpreted to be fault-propagation folds, in which slip on thrust faults at depth are accommodated by asymmetric folding in strong, but weakly bonded layered material (such as basalt flows) near the surface. Partially filled craters and the maximum thickness of strong basalt from rocky ejecta craters indicate the basalts are 200-300 m thick and are underlain by weak sediments. The lack of rocks in most fresh craters <50 m diameter and concentric or nested craters argue for a surficial fragmented regolith 3-17 m thick. Exposures of relatively fine-grained regolith around 10 m thick that grades with depth into coarse breccia overlying strong jointed bedrock in nearby Hephaestus Fossae in southern Utopia Planitia, suggests the regolith was built up by impacts in agreement with fragmentation theory constrained by the size-frequency distribution of craters and observed rock abundance.

Investigation of the InSight landing site in remote sensing data during landing site selection indicates a smooth, flat surface with very low rock abundance punctuated by relatively fresh rocky ejecta craters as well as small secondary craters from Corinto crater ~600 km to the north-northeast. Relatively homogeneous thermal inertia of the surface indicates it is dominated by fine to very fine sand that is either cohesionless or has very low cohesion with no difference in properties within a few tens of centimeters of the surface. The dust cover index, albedo and thermophysical properties indicate the surface is covered by an optically thick but thermally thin (~hundreds of μm) coating of dust. Eolian bedforms are concentrated in the ejecta and interiors of fresh craters and relatively absent in the inter-crater smooth plains indicating sand organizes into bedforms soon after crater formation and rapidly migrate over the rims and into the interiors of the craters. Northwest trending dust devil tracks are ubiquitous and the northeast orientation of bedforms inside craters and concentration of bedforms on the outer northwest margins of crater rims suggest formative winds from the northwest. These observations indicate the surface is shaped by impact and eolian processes, consistent with the estimated slow erosion and degradation rates of the rocky ejecta craters.

The geology and physical properties investigation are central to finding locations that are smooth, flat (<15°), rock free (no rocks >3 cm high) and load bearing in the workspace where the instruments can be placed by the arm. Placing the instruments on the surface is the highest priority project activity immediately after landing. Stereo color images are used to create mosaics, DEMs and instrument deployment products that delineate areas that meet instrument deployment requirements. The geology subgroup will evaluate the surficial geology and map soils, rocks, eolian bedforms and other geological features such as craters from stereo color mosaics and derived products. The physical properties subgroup will derive the thermal inertia of the two

radiometer spots on the surface, separate the rocky from fine components from stereo surface images, and estimates particle size and cohesion of the fine component to determine if the soil is load bearing. The arm and deployment engineers determine the workspace from the attitude of the lander and topography of the surface, evaluate locations in the workspace where the arm can deploy the instruments, and assess tether configurations. Instrument teams consider noise sources and specific placement locations. Given the choice, the seismometer would be placed as far away from lander feet as possible, and more than 1 m to the right (east) of the heat flow probe, which would also be placed as far away from the lander as possible.

The geology investigation characterizes the geology of the InSight landing site, and provides ground truth for orbital remote sensing data. Similar investigations for previous missions have established the basic geologic evolution of the local region, identified the geologic materials present, and quantified their areal coverage. The information gathered about the geology of the surface can be used to infer the geologic processes that have operated on it and the shallow subsurface structure. This will test specific predictions made using orbital remote sensing during landing site selection including: rock size-frequency distributions, surface slopes, thermal inertia and soil properties, and eolian features and activity. Continuous measurements of wind speed and direction offer a unique opportunity to correlate dust devils and high winds with eolian changes imaged at the surface and to determine the threshold friction wind stress for grain motion on Mars. The removal of dust by thrusters during landing will darken the surface, and then brightening with time can be determined using surface and orbital images. This brightening is expected from dust settling from the atmosphere, and that rate of dustfall can be compared with the amount of dust present in the atmosphere (from camera opacity measurements) and dust falling on the solar panels (from solar array energy).

Reconstruction of the location of InSight after landing and RISE tracking will yield a superb tie between the cartographic and inertial reference frames. InSight will be the best know position on the surface of Mars. An initial estimate of landed position will be generated by combining estimated navigation errors with an onboard inertial position estimate generated by onboard propagation of accelerations, which is expected to be within 1 km of the actual landed location. The first hour of radio Doppler tracking will determine the lander longitude and distance from the spin axis to about 20 m, which when combined with surface topography of the landing site (relatively constant) will also determine the inertial location to much better than 1 km. These estimates of inertial location generated within a few days after landing should be sufficient to target a HiRISE image of the lander on the surface. Once a HiRISE image is acquired, the image can be georeferenced onto landing site maps, which have been georeferenced in a pyramid starting with MOLA elevation maps, 463 m/pixel; HRSC images, 12.5 m/pixel; CTX 5–6 m/pixel; and HiRISE ~0.25–0.3 m/pixel, to determine the landers cartographic position. By the end of the nominal InSight mission (1 Mars year), the inertial location from radio Doppler tracking measurements will be accurate to around 2 m, surpassing previous landers locations by a factor of 5, which if used as a new reference for longitude on Mars (currently referenced to VL1), will provide a new longitude reference accurate to about 2 cm.

Soil mechanics parameters and elastic constants of near surface materials will be determined from soil mechanics experiments with the arm and scoop (indentations, scraping, trenching and piling), passive monitoring of seismic waves, mole penetration and thermal conductivity measurements from the surface to 3-5 m depth, and the measurement of seismic waves generated during mole hammering. Calibrated motor currents of the arm and interactions of the scoop with the surface can be used to derive standard soil mechanics parameters such as the

angle of repose or angle of internal friction from piles of soil created on the surface, cohesion from scraping and elastic constants (Young's and shear moduli) from indentations. The HP^3 mole penetration speed will be used to constrain the angle of internal friction and soil density using soil physics models and laboratory studies of simulants. SEIS passive monitoring of atmospheric disturbances, high-frequency surface waves, lander mechanical noise, and cut-off frequency of impacts can be used to estimate P- and S-wave velocities with depth in the shallow subsurface as well as well as regolith thickness and porosity. SEIS measurement of HP^3 mole hammering will be used to extract elastic physical properties, P- and S-wave velocities, seismic attenuation and their variations with depth via seismic exploration techniques. Combining these different techniques will yield soil mechanics parameters as well as seismic velocities and attenuation with depth that will reduce travel-time and amplitude errors of globally propagating seismic waves.

The results of the InSight geology and physical properties investigations will determine and test the presence and mechanical properties of the expected 3-17 m thick fragmented regolith built up on top of Hesperian lava flows by impact and eolian activity and determine its seismic properties for the seismic investigation of Mars' interior. Surface material properties characterized by the InSight lander can be compared to those expected from orbital remote sensing data at the landing site such as thermal inertia, particle size and cohesion, rock abundance, and dustiness. Geologic processes expected from orbital data that are important in shaping the surficial layer (impact and eolian) can be compared with that found from the lander. These comparisons of the surface seen from the lander are "ground truth" to orbital remote sensing data and interpretations and are important for future landing site selection on Mars.

Acknowledgements

A portion of the work was supported by the InSight Project at the Jet Propulsion Laboratory, California Institute of Technology, under a contract with the National Aeronautics and Space Administration. N. A. Teanby is supported by the UK Space Agency. French authors acknowledge the support by Centre National d'Études Spatiales (CNES) and IPGP authors the financial support of the UnivEarthS Labex program at Sorbonne Paris Cite (ANR-10-LABX-0023, ANR-11-1013 IDEX-0005-02, and ANR SIMARS). The work by C. Schmelzbach and J. Robertsson was partly supported by ETH Research Grant ETH-06 17-2. This paper is InSight Contribution Number 40.

References:

D.A. Alexander, et al. (2006), Processing of Mars Exploration Rover imagery for science and operations planning, J. Geophys. Res., 111, E02S02, doi:10.1029/2005JE002462.

K.A. Alshibli, A. Hasan, Strength properties of JSC-1A lunar regolith simulant. Journal of Geotechnical and Geoenvironmental Engineering, 2009. **135**(5): p. 673-679.

R.E. Arvidson, Anderson, R. C., Bartlett, P., Bell, III, J. F., Blaney, D., Christensen, P. R., Chu, P., Crumpler, L., Davis, K., Ehlmann, B. L., Fergason, R., Golombek, M. P., et al., 2004a,

Localization and physical properties experiments conducted by Spirit at Gusev crater: Science, 305, 5685, 821-824, DOI: 10.1126/science.1099922.

R.E. Arvidson, Anderson, R. C., Bartlett, P., Bell, III, J. F., Christensen, P. R., Chu, P., Davis, K., Ehlmann, B. L., Golombek, M. P., et al., 2004b, Localization and physical properties experiments conducted by Opportunity at Meridiani Planum: Science, 306, Issue 5702, 1730-1733, DOI: 10.1126/science.1104211.

R. Arvidson, Adams, D., Bonfiglio, G., Christensen, P., Cull, S., Golombek, M., Guinn, J., Guinness, E., Heet, T., Kirk, R., Knudson, A., Malin, M., Mellon, M., McEwen, A., Mushkin, A., Parker, T., Seelos, F., Seelos, K., Smith, P., Spencer, D., Stein, T., Tamppari, L., 2008, Mars Exploration Program 2007 Phoenix landing site selection and characteristics: J. Geophys. Res., Planets, 113, E00A03, doi:10.1029/2007JE003021.

R.E. Arvidson et al. (2014), Terrain physical properties derived from orbital data and the first 360 sols of Mars Science Laboratory Curiosity rover observations in Gale Crater, J. Geophys. Res. Planets, 119, 1322–1344, doi:10.1002/ 2013JE004605.

J.H. Atkinson, Sallfors, G. (1991) Experimental determination of soil properties. General Report to Session 1. Proceedings of the 10th ECSMFE, Florence 3, 915-956.

F. Ayoub, Avouac, J.P., Newman, C.E., Richardson, M.I., Lucas, A., Leprince, S., Bridges, N. T., 2014. Threshold for sand mobility on Mars calibrated from seasonal variations of sand flux. Eighth International Conference on Mars, Pasadena, CA, July 14-18, 2014, Abstract #1064, Lunar and Planetary Institute, Houston.

C. Bagaini, Barajas-Olalde, C. (2007) Assessment and compensation of inconsistent coupling conditions in point-receiver land seismic data. Geophysical Prospecting, 55: 39–48. doi:10.1111/j.1365-2478.2006.00606.x

R.A. Bagnold, 1941. The physics of blown sand and desert dunes. Methuen, New York.

J.L. Bandfield, R. R. Ghent, A. R. Vasavada, D. A. Paige, S. J. Lawrence, M. S. Robinson (2011) Lunar surface rock abundance and regolith fines temperatures derived from LRO Diviner Radiometer data, J. Geophys. Res.-Planets, 116, 18, doi:10.1029/2011je003866.

W.B. Banerdt et al. 2018, The InSight Mission, Space Science Reviews, this issue.

D. Banfield et al. 2018 APSS, Space Science Reviews, this issue.

A. Becker, C. Vrettos, Tests on the thermal conductivity of regolith quasi-analogues at different porosities, in Earth and Space 2016, 15th ASCE International Conference on Engineering, Science, Construction and Operations in Challenging Environments (2016)

R.A. Beyer, Meter-scale slopes of candidate InSight landings sites from point photoclinometry. Space Sci. Rev. 211, 97–107 (2017). doi:10.1007/s11214-016-0287-7

A.B. Binder, R. E. Arvidson, E. A. Guinness, et al., The geology of the Viking Lander 1 site, J. Geophys. Res. 82, 4439–51, 1977.

J.E. Bleacher, Orr, T.R., de Wet, A.P., Zimbelman, J.R., Hamilton, C.W., Garry, W.B., Crumpler, L.S., Williams, D.A. (2017) Plateaus and sinuous ridges as the fingerprints of lava flow inflation in the Eastern Tharsis Plains of Mars. Journal of Volcanology and Geothermal Research, 342, 29-46, doi: 10.1016/j.jvolgeores.2017.03.025.

C. Bloom, Golombek, M., Warner, N., and Wigton, N., 2014, Size frequency distribution and ejection velocity of Corinto crater secondaries in Elysium Planitia, Eighth International Conference on Mars, Pasadena, CA, July 14-18, 2014, Abstract #1289, Lunar and Planetary Institute, Houston.

N.T. Bridges, F. Ayoub, J-P. Avouac, S. Leprince, A. Lucas, S. Mattson, 2012, Earth-like sand fluxes on Mars, Nature 485, 339–342.

N. Bridges, Geissler, P., Silvestro, S., Banks, M., 2013. Bedform migration on Mars: Current results and future plans. Aeolian Research 9, 133–151.

D.C. Catling et al., A lava sea in the northern plains of Mars: circumpolar Hesperian oceans reconsidered, in 42nd Lunar and Planetary Science Conference (Lunar and Planetary Institute, Houston, 2011). Abstract #2529.

D.C. Catling et al., Does the Vastitas Borealis formation contain oceanic or volcanic deposits? in Third Conference on Early Mars, Lake Tahoe, NV, May 21–25, 2012 (Lunar and Planetary Institute, Houston, 2012). Abstract #7031.

W.D. Carrier, J.K. Mitchell, A. Mahmood (1973), The relative density of lunar soil, Proc. Lunar Sci. Conf., 4th, 4, 118–120.

M.A. Carrigy, Experiments on the angles of repose of granular materials. Sedimentology, 1970. **14**(3-4): 147-158.

C. Charalambous, On the evolution of particle fragmentation with applications to planetary surfaces. PhD Thesis, Imperial College London (2015)

C. Charalambous, W. T. Pike, M. P. Golombek (2017), Estimating the grain size distribution of Mars based on fragmentation theory and observations, Abstract P41C-2843, 2017 Fall AGU Meeting, New Orleans, LA, 11–15 Dec.

M. Chojnacki, Johnson, J. R., Moersch, J. E., Fenton, L. K., Michaels, T. I., Bell, III, J. F., 2015. Persistent aeolian activity at Endeavour crater, Meridiani Planum, Mars; new observations from orbit and the surface. Icarus 251, 275–290.

T.E. Chamberlain, H.L. Cole, R.G. Dutton, G.C. Greene, J.E. Tillman, 1976. Atmospheric measurements of Mars: The Viking Meteorology Experiment. Bull. Amer. Met Soc., 57, 1094-1104.

P.R Christensen, (1986), The spatial distribution of rocks on Mars, Icarus, 68, 217-238.

P.R. Christensen, H.J. Moore, The martian surface layer, in MARS, ed. by H.H. Kieffer, B.M. Jakosky, C.W. Snyder, M.S. Matthews (University of Arizona Press, Tucson, 1992), pp. 686–727

P.R. Christensen, B.M. Jakosky, H.H. Kieffer, M.C. Malin, H.Y. McSween Jr., K. Nealson, G.L. Mehall, S.H. Silverman, S. Ferry, M. Caplinger, M. Ravine, The Thermal Emission Imaging System (THEMIS) for the Mars 2001 Odyssey mission. Space Sci. Rev. 110, 85–130 (2004)

P. Claudin, Andreotti B., 2006. A Scaling low for aeolian dunes on Mars, Venus, Earth and for subaqueous ripples. Earth Planet. Sci., 252, 30-44.

J.F. Clinton, Giardini, D., Lognonné, P., Banerdt, B., van Driel, M., Drilleau, M., Murdoch, N., Panning, M., Garcia, R., Mimoun, D., Golombek, M., Tromp, J., Weber, R., Böse, M., Ceylan, S., Daubar, I., Kenda, B., Khan, A., Perrin, L., Spiga, A., 2017, Preparing for InSight: An invitation to participate in a blind test for Martian seismicity: Seismological Research Letters, 88, 1290-1302, doi: 10.1785/0220170094.

J.F. Clinton et al., 2018, Marsquake Service - building a Martian seismicity catalogue for InSight, Space Science Reviews, this issue.

S. Courrech du Pont, C. Narteau, X. Gao, 2014, Two modes for dune orientation. Geology, 42, 743-746.

R.A. Craddock, Golombek, M. P., 2016, Characteristics of terrestrial basaltic rock populations: Implications for Mars lander and rover science and safety: Icarus, 274, 50-72, doi:10.1016/j.icarus.2016.02.042.

I.J. Daubar, McEwen, A. S., Golombek, M. P., 2015, Albedo changes at Martian landing sites, 46th Lunar and Planetary Science, Abstract #2225, Lunar and Planetary Institute, Houston.

I.J. Daubar, Dundas, C.M., Byrne, S., Geissler, P., Bart, G.D., McEwen, A.S., Russell, P.S., Chojnacki, M., Golombek, M.P., 2016, Changes in blast zone albedo patterns around new martian impact craters: Icarus, 267, 86-105, doi.org/10.1016/j.icarus.2015.11.032.

I.J. Daubar et al. (2018) Impact-seismic investigations of the InSight mission, Space Science Reviews, this issue.

R.G. Deen (2003), Cost savings through Multimission code reuse for Mars image products, paper presented at 5th International Symposium on Reducing the Cost of Spacecraft Ground Systems and Operations, Deep Space Commun. and Navig. Syst. Cent. of Excellence (DASCANSO), Jet. Propul. Lab., Pasadena, Calif.

R. Deen, P. Zamani, H. Gengl, J. Maki, InSight software interface specification: Camera Experiment Data Record (EDR) and Reduced Data Record (RDR) data products, in preparation, to be published by NASA Planetary Data System (2018).

V. Dehant, Folkner W., Renotte E., Orban D., Asmar S., Balmino G., Barriot J.P., Benoist J., Biancale R., Biele J., Budnik F., Burger S., de Viron O., Häusler B., Karatekin Ö., Le Maistre S., Lognonné P., Menvielle M., Mitrovic M., Pätzold M., Rivoldini A., Rosenblatt P., Schubert G., Spohn T., Tortora P., Van Hoolst T., Witasse O., Yseboodt M., 2009, Lander Radioscience for obtaining the rotation and orientation of Mars, Planet. Space Sci., 57, 1050-1067, DOI: 10.1016/j.pss.2008.08.009.

V. Dehant, Le Maistre S., Rivoldini A., Yseboodt M., Rosenblatt P., Van Hoolst T., Mitrovic M., Karatekin Ö., Marty J.C., Chicarro A., 2011, Revealing Mars' deep interior: Future geodesy missions using radio links between landers, orbiters, and the Earth, Planet. Space Sci., 57, 1069-1081, DOI: 10.1016/j.pss.2010.03.014.

P. Delage, Belmokhtar M., De Laure E., Bencharef S. (2014) The response of various shapes of the SEIS feet. Technical report submitted to IPGP.

P. Delage, Karakostas, F., Dhemaied, A., Belmokhtar, M., Lognonné, P., Golombek, M., De Laure, E., Hurst, K., Dupla, J.-C., Kedar, S., Cui, Y. J., Banerdt, B., 2017, An investigation of the mechanical properties of some Martian regolith simulants with respect to the surface properties at the InSight mission landing site: Space Science Reviews, 211, 191-213, DOI 10.1007/s11214-017-0339-7.

L. Drube, et al. (2010), Magnetic and optical properties of airborne dust and settling rates of dust at the Phoenix landing site, J. Geophys. Res., 115, E00E23, doi:10.1029/2009JE003419.

B.L. Ehlmann et al., 2018, Chemistry, mineralogy, and grain properties at Namib and high dunes, Bagnold dune field, Gale Crater, Mars: A synthesis of curiosity rover observations, J. Geophys. Res. Planets special issue, Bagnold dunes, 15 January 2017; revised 14 May 2017 2017JE005267

L. Fayon et al. 2018, Elastic stiffness of SEIS and the mechanical properties of soils, in preparation.

R.L. Fergason, P.R. Christensen, J.F. Bell III, M.P. Golombek, K.E. Herkenhoff, H.H. Kieffer, Physical properties of the Mars Exploration Rover landing sites as inferred from Mini-TES derived thermal inertia. J. Geophys. Res. 111(E2), E02S21 (2006). doi:10.1029/2005JE002583

R. Fergason, Kirk, R. L., Cushing, G., Galuzska, D. M., Golombek, M. P., Hare, T. M., Howington-Kraus, E., Kipp, D. M., Redding, B. L., 2017, Analysis of local slopes at the InSight landing site on Mars: Space Science Reviews, 211, 109-133, DOI 10.1007/s11214-016-0292-x.

L. Fernandez-Cascales, Lucas A., Rodriguez S., Gao X., Spiga A., Narteau C., 2018, First quantification of relationship between dune orientation and sediment availability, Olympia Undae, Mars. Earth Planet. Sci. Lett., under review

W. M. Folkner, C. F. Yoder, D. N. Yuan, E. M. Standish, R. A. Preston, Interior structure and seasonal mass redistribution of Mars from radio tracking of Mars Pathfinder, Science, 278, 1749-1752, 1997

W.M. Folkner, J.G. Williams, D.H. Boggs, R.S. Park, P. Kuchynka. "The planetary and lunar ephemerides DE430 and DE431." *Interplanet*. *Netw*. *Prog*. *Rep* 196 (2014): 1-81

W. Folkner et al. 2018 The Rotation and Interior Structure Experiment on the InSight Mission to Mars, Space Science Reviews, this issue.

H.V. Frey, Impact constraints on, and a chronology for, major events in early Mars history. J. Geophys. Res. 111, E08S91 (2006). doi:10.1029/2005JE002449

X. Gao, C. Narteau, O. Rozier, S. Courrech du Pont, 2015, Phase diagrams of dune shape and orientation depending on sand availability. Scientific Reports, 5, 14677.

E. Gardin, Allemand, P., Quantin, C., Silvestro, S., Delacourt, C., 2012. Dune fields on Mars: Recorders of a climate change? Plan. & Space Sci. 60, 314–321.

J.B. Garvin, Mouginis-Mark, P.J., Head, J.W., 1981. Characterization of rock populations on planetary surfaces: Techniques and a preliminary analysis of Mars and Venus. Moon Planets 24, 355–387

J.B. Garvin, Sakamoto, S. E. H., Schnetzler, C., Frawley, J. J., 2003, Craters on Mars: Global geometric properties from gridded MOLA topography, 6th International Conference on Mars, California Institute of Technology, Pasadena, California, 20– 25 July, Abs. #3277.

W. Goetz et al., Microscopy analysis of soils at the Phoenix landing site, Mars: classification of soil particles and description of their optical and magnetic properties. J. Geophys. Res. 115, E00E22 (2010). doi:10.1029/2009JE003437

M.P. Golombek, Plescia, J. B., Franklin, B. J. (1991). Faulting and folding in the formation of planetary wrinkle ridges. Proc. Lunar Planet. Sci. Conf. 21, 679–693.

M.P. Golombek, N.T. Bridges (2000), Erosion rates on Mars and implications for climate change: Constraints from the Pathfinder landing site, J. Geophys. Res. Planets, 105(E1), 1841–1853, doi:10.1029/1999JE001043.

M.P. Golombek, R.J. Phillips, Mars Tectonics, in Planetary Tectonics, ed. by T.R. Watters, R.A. Schultz (Cambridge University Press, Cambridge, 2010), pp. 183–232, Chap. 5

M.P. Golombek, Cook, R. A., Economou, T., Folkner, W. M., Haldemann, A. F. C., Kallemeyn, P. H., Knudsen, J. M., Manning, R. M., Moore, H. J., Parker, T. J., Rieder, R., Schofield, J. T., Smith, P. H., Vaughan, R. M., 1997a, Overview of the Mars Pathfinder mission and assessment of landing site predictions: Science, 278, 1743-1748.

M.P. Golombek, R.A. Cook, H.J. Moore, T.J. Parker, Selection of the Mars Pathfinder landing site. J. Geophys. Res. 102, 3967–3988 (1997b)

M.P. Golombek, and the Mars Pathfinder science team, 1999a, Overview of the Mars Pathfinder mission: Launch through landing, surface operations, data sets, and science results, J. Geophys. Res., 104, 8523-8553.

M.P. Golombek, Moore, H. J., Haldemann, A. F. C., Parker, T. J., and Schofield, J. T., 1999b, Assessment of Mars Pathfinder landing site predictions, J. Geophys. Res., 104, 8585-8594.

M.P. Golombek et al., Selection of the Mars Exploration Rover landing sites. J. Geophys. Res. 108(E12), 8072 (2003a). doi:10.1029/2003JE002074

M.P. Golombek, A.F.C. Haldemann, N.K. Forsberg-Taylor, E.N. DiMaggio, R.D. Schroeder, B.M. Jakosky, M.T. Mellon, J.R. Matijevic, Rock size-frequency distributions on Mars and implications for Mars Exploration Rover landing safety and operations. J. Geophys. Res. 108(E12), 8086 (2003b). doi:10.1029/2002JE002035

M.P. Golombek et al., Assessment of Mars Exploration Rover landing site predictions. Nature 436, 44–48 (2005). doi:10.1038/nature03600

M.P. Golombek et al., Geology of the Gusev cratered plains from the Spirit rover traverse. J. Geophys. Res. 110, E02S07 (2006a). doi:10.1029/2005JE002503

M.P. Golombek, J. A. Grant, L. S. Crumpler, R. Greeley, R. E. Arvidson, J. F. Bell III, C. M. Weitz, R. Sullivan, P. R., Christensen, L. A. Soderblom, S. W. Squyres (2006b), Erosion rates at the Mars Exploration Rover landing sites and long-term climate change on Mars, J. Geophys. Res. Planets, 111, E12S10, doi:10.1029/2006JE002754.

M.P. Golombek, A.F.C. Haldemann, R.A. Simpson, R.L. Fergason, N.E. Putzig, R.E. Arvidson, J.F. Bell III, M.T. Mellon, Martian surface properties from joint analysis of orbital, Earth-based, and surface observations, in The Martian Surface: Composition, Mineralogy and Physical Properties. ed. by J.F. Bell III (Cambridge University Press, Cambridge, 2008a), pp. 468–497 Chap. 21

M.P. Golombek et al., Size-frequency distributions of rocks on the northern plains of Mars with special reference to Phoenix landing surfaces. J. Geophys. Res. 113, E00A09 (2008b). doi:10.1029/2007JE003065

M. Golombek, K. Robinson, A. McEwen, N. Bridges, B. Ivanov, L. Tornabene, R. Sullivan (2010), Constraints on ripple migration at Meridiani Planum from Opportunity and HiRISE observations of fresh craters, J. Geophys. Res., 115, E00F08, doi:10.1029/2010JE003628.

M. Golombek, J. Grant, D.D. Kipp, A. Vasavada, R. Kirk, R. Fergason, P. Bellutta, F. Calef, K. Larsen, Y. Katayama, A. Huertas, R. Beyer, A. Chen, T. Parker, B. Pollard, S. Lee, R. Hoover, H. Sladek, J. Grotzinger, R. Welch, E. Noe Dobrea, J. Michalski, M.M. Watkins, Selection of the Mars Science Laboratory landing site. Space Sci. Rev. 170, 641–737 (2012a). doi:10.1007/s11214-012-9916-y

M. Golombek, A. Huertas, D. Kipp, F. Calef, Detection and characterization of rocks and rock size-frequency distributions at the final four Mars Science Laboratory landing sites. Mars 7, 1–22 (2012b). doi:10.1555/mars.2012.0001

M.P. Golombek, N.H. Warner, V. Ganti, M.P. Lamb, T.J. Parker, R.L. Fergason, R. Sullivan (2014), Small crater modification on Meridiani Planum and implications for erosion rates and climate change on Mars, J. Geophys. Res. Planets, 119, 2522–2547, doi:10.1002/2014JE004658.

M. Golombek, Kipp, D., Warner, N., Daubar, I. J., Fergason, R., Kirk, R., Beyer, R., Huertas, A., Piqueux, S., Putzig, N. E., Campbell, B. A., Morgan, G. A., Charalambous, C., Pike, W. T., Gwinner, K., Calef, F., Kass, D., Mischna, M., Ashley, J., Bloom, C., Wigton, N., Hare, T., Schwartz, C., Gengl. H., Redmond, L., Trautman, M., Sweeney, J., Grima, C., Smith, I. B., Sklyanskiy, E., Lisano, M., Benardini, J., Smrekar, S., Lognonné, P., Banerdt, W. B., 2017, Selection of the InSight landing site: Space Science Reviews, 211, 5-95, DOI 10.1007/s11214-016-0321-9.

J. Gomez-Elvira, C. Armiens, L. Castaner, M. Dominguez, M. Genzer, F. Gomez, R. Haberle, A.-M. Harri, V. Jimenez, H. Kahanpaa, L. Kowalski, A. Lepinette, J. Martin, J. Martinez-Frias, I. McEwan, L. Mora, J. Moreno, S. Navarro, M.A.de Pablo, V. Peinado, A. Pena, J. Polkko, M. Ramos, N.O. Renno, J. Ricart, M. Richardson, J. Rodriguez-Manfredi, J, Romeral ,E.

Sebastian, J Serrano, M. dela Torre Juarez, J Torres, F. Torrero, R. Urqui, L. Vazquez, T. Velasco, J. Verdasco, M.-P. Zorzano, J. Martin-Torres, 2012. REMS: The environmental sensor suite for the Mars Science Laboratory Rover. Space Sci. Rev., 170, 583-640.

S. Goossens, T.J. Sabaka, A. Genova, E. Mazarico, J.B. Nicholas, G.A. Neumann, 2017. Evidence for a low bulk crustal density for Mars from gravity and topography, Geophys. Res. Lett. 44 doi:10.1002/2017GL074172.

R. Greeley, Bridges, N. T., Kuzmin, R. O., Laity, J. E., 2002. Terrestrial analogs to wind-related features at the Viking and Pathfinder landing sites on Mars. J. Geophys. Res. 107 (E1), E5005.

R. Greeley, Iversen, J. D., 1985. Wind as a geological process on Earth, Mars, Venus and Titan. No. 4 in Cambridge Planetary Science Series. Cambridge Univ. Press, Cambridge.

R. Greeley, Skypeck, A., Pollack, J. B., 1993. Martian aeolian features and deposits – Comparisons with general circulation model results. J. Geophys. Res. 98, 3183–3196.

T.K.P. Gregg (2017), Patterns and processes: Subaerial lava flow morphologies: A review, Journal of Volcanology and Geothermal Research, 342, 3-12, doi: 10.1016/j.jvolgeores.2017.04.022

M. Grott, J. Helbert, R. Nadalini, Thermal structure of Martian soil and the measurability of the planetary heat flow, J. Geophys. Res., 112, E09004 (2007).

M. Grott, Thermal disturbances caused by lander shadowing and the measurability of the martian planetary heat flow, Plan. Space Sci., 57, 71-77 (2009)

T.V. Gudkova, P. Lognonné, J. Gagnepain-Beyneix (2011) Large impacts detected by the Apollo seismometers: impactor mass and source cutoff frequency estimation, Icarus, 211, 1049-1065

T. Gudkova, P. Lognonné, K. Miljkovic, J. Gagnepain-Beyneix (2015) Impact cut-off frequency-momentum scaling law inverted from Apollo seismic data, Earth Planet. Sci. Lett., 427, 57-65, doi:10.1016/j.epsl.2015.06.037

K. Gwinner, F. Scholten, F. Preusker, S. Elgner, T. Roatsch, M. Spiegel, R. Schmidt, J. Oberst, R. Jaumann, C. Heipke, Topography of Mars from global mapping by HRSC high-resolution digital terrain mod- els and orthoimages: characteristics and performance. Earth Planet. Sci. Lett. 294, 506–519 (2010). doi:10.1016/j.epsl.2009.11.007

V.E. Hamilton, A.R. Vasavada, E. Sebastián, M. de la Torre Juárez, M. Ramos, et al. (2014), Observations and preliminary science results from the first 100 sols of MSL Rover Environmental Monitoring Station ground temperature sensor measurements at Gale Crater, J. Geophys. Res. Planets, 119, 745–770, doi:10.1002/2013JE004520.

M. Hamm, M. Grott, E. Kührt, et al., A method to derive surface thermophysical properties of asteroid (162173) Ryugu (1999JU3) from In-Situ Surface Brightness Temperature Measurements, Plan. Space Sci., submitted (2018)

H. Hansen-Goos, M. Grott, R. Lichtenheld et al., Predicted penetration performance of the InSight HP3 mole , Lunar and Planetary Science Conference, 45, abstract 1325 (2014)

K.C. Horstman, H.J. Melosh, Drainage pits in cohesionless materials: Implications for the surface of Phobos. Journal of Geophysical Research: Solid Earth, 1989. **94**(B9): p. 12433-12441.

W.K. Hartmann, Anguita J. de la Casa, M. Berman, D.D. Ryan, E. Martian, Cratering 7: The role of impact gardening. Icarus 149, 37–53 (2001)

L.A. Haskin et al., 2005, Water alteration of rocks and soils on Mars at the Spirit rover site in Gusev crater, 436, 66-69, July 2005|doi:10.1038/nature03640.

R. K. Hayward, K.F. Mullins, L.K. Fenton, T.M. Hare, T.N. Titus, M.C. Bourke, A. Colaprete, P.R. Christensen (2007), Mars Global Digital Dune Database and initial science results, J. Geophys. Res., 112, E11007, doi:10.1029/2007JE002943.

E. Hébrard, C. Listowski, P. Coll, B. Marticorena, G. Bergametti, A. Määttänen, F. Montmessin, F. Forget (2012), An aerodynamic roughness length map derived from extended Martian rock abundance data, J. Geophys. Res., 117, E04008, doi:10.1029/2011JE003942.

T.L. Heet, R.E. Arvidson, S.C. Cull, M.T. Mellon, K.D. Seelos, Geomorphic and geologic settings of the Phoenix lander mission landing site. J. Geophys. Res. 114, E00E04 (2009). doi:10.1029/2009JE003416

M. Hobiger, N. Le Bihan, C. Cornou, P.-Y. Bard (2012) Multicomponent signal processing for Rayleigh wave ellipticity estimation, IEEE Signal Process. Mag. 29, 29–39, doi:10.1109/MSP.2012.2184969

R.D. Holtz, W.D. Kovacs, An Introduction to Geotechnical Engineering (1981) Prentice Hall.

K. Hon, Kauahikaua, J., Denlinger, R., Mackay, K. (1994) Emplacement and inflation of pahoehoe sheet flows: Observations and measurements of active lava flows on Kilauea Volcano, Hawaii. Geological Society of America Bull., 106 (3), 351-370.

C.B. Hundal, M. P. Golombek, I. J. Daubar (2017), Chronology of fresh rayed craters in Elysium Planitia, Mars, 48th Lunar Planet. Sci. Conf., Abstract 1726.

J.A. Hurowitz, S. M. McLennan, N. J. Tosca, R. E. Arvidson, J. R. Michalski, D. W. Ming, C. Schroder, S. W. Squyres (2006), In situ and experimental evidence for acidic weathering of rocks and soils on Mars, J. Geophys. Res., 111, E02S19, doi:10.1029/2005JE002515.

R.A. Jacobson, A.S. Konopliv, R.S. Park, W.M. Folkner, The rotational elements of Mars and Its satellites, Planetary and Space Science, in press, 2018.

B.M. Jakosky, P.R. Christensen (1986), Global duricrust on Mars: Analysis of remote sensing data, Journal of Geophysical Research, 91(No. B3), 3547-3560.

R. Kawamoto, et al., Level set discrete element method for three-dimensional computations with triaxial case study. Journal of the Mechanics and Physics of Solids, 2016. 91: p. 1-13.

S. Kedar, Andrade, J., Banerdt, B., Delage. P., Golombek, M., Grott, M., Hudson, T., Kiely, A., Knappmeyer, M., Knapmeyer-Endrun, B., Krause, C., Kawamura, T., Lognonne, P., Pike, T., Ruan, Y., Spohn, T., Teanby, N., Tromp, J., Wookey, J., 2017, Analysis of regolith properties using seismic signals generated by InSight's HP^3 penetrator: Space Science Reviews, 211, 315-337, DOI 10.1007/s11214-017-0391-3.

B. Kenda, P. Lognonné, A. Spiga, T. Kawamura, S. Kedar, W. B. Banerdt, R. Lorenz, D. Banfield, M. Golombek (2017) Modeling of ground deformation and shallow surface waves generated by Martian dust devils and perspectives for near-surface structure inversion, Space Sci. Rev., 211, 501-524, doi:10.1007/s11214-017-0378-0

H.H. Kieffer, Thermal model for analysis of Mars infrared mapping, J. Geophys. Res. Planets, 118, 451470 (2013)

B. Knapmeyer-Endrun, M. Golombek, M. Ohrnberger (2017) Rayleigh wave ellipticity modeling and inversion for shallow structure at the proposed InSight landing site in Elysium Planitia, Space Sci. Rev., 211, 339-382, doi:10.1007/s11214-016-0300-1

N.I. Kömle, J. Poganski, G. Kargl, J. Grygorczuk, Pile driving models for the evaluation of soil penetration resistance measurements from planetary subsurface probes, Plan. Space Sci.,109-110, 135–148 (2015)

A.S. Konopliv, Yoder, C.F., Standish, E.M., Yuan, D.N. Sjogren, W.L., 2006. A global solution for the Mars static and seasonal gravity, Mars orientation, Phobos and Deimos masses, and Mars ephemeris. Icarus, 182(1), pp.23-50.

A.S. Konopliv, Asmar S.W., Folkner W.M., Karatekin Ö., Nunes D.C., Smrekar S.E., Yoder C.F., Zuber M.T., 2011, Mars high resolution gravity fields from MRO, Mars seasonal gravity, and other dynamical parameters, Icarus, 211, 401-428.

A.S. Konopliv, Park R.S., Folkner W.M., 2016, An improved JPL Mars gravity field and orientation from Mars orbiter and lander tracking data, Icarus, 274, 253-260, DOI: 10.1016/j.icarus.2016.02.052.

P. Kuchynka, Folkner, W.M., Konopliv, A.S., Park, R.S., Le Maistre S., Dehant, V., 2014. New constraints on Mars rotation determined from radiometric tracking of the Opportunity Mars Exploration Rover. Icarus, 229: 340–347, ISSN 0019-1035. http://dx.doi.org/10.1016/j.icarus.2013.11.015.

L. Lancelot, Shahrour I., Al Mahmoud M. (1996). Comportement du sable d'Hostun sous faibles contraintes. Rev. Fr. Géotech. 74, 63–74.

G.A. Landis, P.P. Jenkins (2000), Measurement of the settling rate of atmospheric dust on Mars by the MAE instrument on Mars Pathfinder, J. Geophys. Res., 105, 1855–1857

E. Larose, Khan A., Nakamura Y., Campillo M. (2005) Lunar subsurface investigated from correlation of seismic noise. Geophysical Research Letters 32: L16201, doi: 10.1029/2005GL023518

S. Le Maistre, Rosenblatt, P., Rivoldini, A., Dehant, V., Marty, J-C., Karatekin, Ö., 2012. Lander radio science experiment with a direct link between Mars and the Earth. Planet. Space Sci. 68 (July (1)), 105–122, ISSN 0032-0633. http://dx.doi.org/10. 1016/j.pss.2011.12.020.

S. Le Maistre, 2016. InSight coordinates determination from direct-to-Earth radio-tracking and Mars topography model. Planetary and Space Science, 121, 1–9, http://dx.doi.org/10.1016/j.pss.2015.11.003.

K.L. Lee, Seed H.B. (1967) Drained strength characteristics of drained sands. J. Soil Mech. Found. Div. SM6, 117–141.

M.T. Lemmon, et al. (2004) Atmospheric imaging results from the Mars Exploration Rovers: Spirit and Opportunity, Science 306, 1753-1756. doi:10.1126/science.1104474

R. Lichtenheldt, O. Krömer, Soil modeling for InSight's HP3-Mole: From highly accurate particle-based towards fast empirical models, ASCE Earth and Space Conference (2016)

R. Lichtenheldt, B. Schäfer, O. Krömer, Hammering beneath the surface of Mars - Modeling and simulation of the impact-driven locomotion of the HP3-Mole by coupling enhanced multi-body dynamics and discrete element method, Shaping the future by engineering: 58th Ilmenau Scientific Colloquium, IWK, urn:nbn:de:gbv:ilm1-2014iwk-155:2 (2014)

R. Lichtenheldt, A novel systematic method to estimate the contact parameters of particles in discrete element simulations of soil, Particle-based Methods IV, pp 430-441, ISBN:978-84-944244-7-2 (2015)

R. Lichtenheldt, Lokomotorische Interaktion planetarer Explorationssysteme mit weichen Sandböden, Verlag Dr. Hut, ISBN 978-3-8439-2704-8, Munich, 2016

R. Lichtenheldt, Covering shock waves on Mars induced by InSight's HP3-MOLE – Efficient co-simulation using DEM and multi-domain dynamics, COUPLED PROBLEMS 2017, ISBN: 978-84-943928-3-2, Artes Gráficas Torres S.L.

P. Lognonné et al. 2018, SEIS, SEIS: The Seismic Experiment for Internal Structure of InSight Space Science Reviews, this issue.

R. Lorenz, S. Kedar, N. Murdoch, P. Lognonné, T. Kawamura, D. Mimoun, W. B. Banerdt (2015) Seismometer detection of dust devil vortices by ground tilt, Bull. Seism. Soc. Am., 105, 3015-3023

R. Lorenz, D. Christie (2015) Dust devil signatures in infrasound records of the International Monitoring System, Geophys. Res. Lett., 42, doi:10.1002/2015GL063237

R.D. Lorenz, Reiss, D., 2015. Solar panel clearing events, dust devil tracks, and in-situ vortex detections on Mars. Icarus, 248, pp.162-164.

P. Lü, C. Narteau, Z. Dong, O. Rozier, S. Courrech du Pont, 2017, Unravelling raked linear dunes to explain the coexistence of bedforms in complex dune fields. Nature Communications, 8, 14239.

A. Lucas, C. Narteau, S. Rodriguez, O. Rozier, Y, Callot, A. Garcia, S. Courrech du Pont, 2015. Sediment flux from the morphodynamics of elongating linear dunes Geology, 43, 1027–1030.

J.N. Maki, Lorre, J. J., Smith, P. H., Brandt, R. D., Steinwand, D. J., 1999. The color of Mars: Measurements from the Pathfinder landing site, Journal of Geophysical Research (Planets), April 25th 1999, 104(E4):8781-8794. doi:10.1029/98JE01767.

J.N. Maki, J.F. Bell, KE Herkenhoff, S.W. Squyres, A. Kiely, M. Klimesh, M. Schwochert, T. Litwin, R. Willson, A. Johnson, M. Maimone, E. Baumgartner, A. Collins, M. Wadsworth, S.T. Elliot, A. Dingizian, D. Brown, E.C. Hagerott, L. Scherr, R. Deen, D. Alexander, J. Lorre, The Mars Exploration Rover Engineering Cameras, J. Geophys. Res., 108(E12), 8071, December 2003, doi:10.1029/2003JE002077.

J. Maki, D. Thiessen, A. Pourangi, P. Kobzeff, T. Litwin, L. Scherr, S. Elliott, A. Dingizian, M. Maimone, The Mars Science Laboratory Engineering Cameras, Space Science Reviews, 170:77-93, doi:10.1007/s11214-012-9882-4, 2012.

J.N. Maki, et al., 2018, The Mars InSight lander cameras, Space Science Reviews, this issue.

N. Mangold, Allemand, P., Thomas, P. G., Vidal, G. (2000). Chronology of compressional deformation on Mars: Evidence for a single and global origin. Planet. Space Sci., 48, 1201–1211.

J.P. Marshall, T.L. Hudson, J.E. Andrade, Experimental investigation of InSight HP^3 mole interaction with Martian regolith simulant. Quasi-Static and dynamic penetration testing, Space Sci. Rev., 211, 1–4, 239–258 (2017)

A.S. McEwen, Malin, M. C., Carr, M. H., and Hartmann, W. K. (1999). Voluminous volcanism on early Mars revealed in Valles Marineris. Nature, 397, 584–586.

A.S. McEwen, Tornabene, L.L., Team, H., Eliason, E.M., Bergstrom, J.W., Bridges, N.T., Hansen, C.J., Delamere, W.A., Grant, J.A., Gulick, V.C., Herkenhoff, K.E., Keszthelyi, L., Kirk, R.L., Mellon, M.T., Squyres, S.W., Thomas, N., Weitz, C.M., 2007. Mars Reconnaissance Orbiter's High-Resolution Imaging Science Experiment (HiRISE). J. Geophys. Res. 112, E05S02. doi:10.1029/2005JE002605

G.E. McGill, A.M. Dimitriou, Origin of the Martian global dichotomy by crustal thinning in the Late Noachian or Early Hesperian. J. Geophys. Res. 95, 12,595–12,605 (1990)

I.O. McGlynn, C.M. Fedo, H.Y. McSween Jr. (2011), Origin of basaltic soils at Gusev crater, Mars, by aeolian modification of impact-generated sediment, J. Geophys. Res., 116, E00F22, doi:10.1029/2010JE003712.

D.S. McKay, Carter J.L., Boles W.W., Allen C., Allton J. (1994). JSC-1: a lunar soil simulant. Engineering, Construction, and Operations in Space IV American Society of Civil Engineers, 857-866.

H.Y. McSween, Jr., Murchie, S. L., Crisp, J. A., Bridges, N. T., Anderson, R. C., Bell III, J. F., Britt, D. T., Brückner, J., Dreibus, G., Economou, T., Ghosh, A., Golombek, M. P., Greenwood, J. P., Johnson, J. R., Moore, H. J., Morris, R. V., Parker, T. J., Rieder, R., Singer, R., Wänke, H., 1999, Chemical, multispectral, and textural constraints on the composition and origin of rocks at the Mars Pathfinder landing site: J. Geophys. Res., 104, 8679-8715.

H.Y. McSween, et al. (2004), Basaltic rocks analyzed by the Spirit rover in Gusev crater, Science, 305, 842–845.

M. Mehta, Rennó, N.O., Marshall, J., Rob Grover, M., Sengupta, A., Rusche, N. A., Kok, J.F., Arvidson, R.E., Markiewicz, W.J., Lemmon, M.T., Smith, P.H., 2011. Explosive erosion during the Phoenix landing exposes subsurface water on Mars. Icarus 211, 172–194. doi:10.1016/j.icarus.2010.10.003

M. Mehta, Sengupta, A., Rennó, N.O., Norman, J.W. Van, Huseman, P.G., Gulick, D.S., Pokora, M., 2013. Thruster Plume Surface Interactions: Applications for Spacecraft Landings on Planetary Bodies. AIAA J. 51, 2800–2818. doi:10.2514/1.J052408

M.T. Mellon, B.M. Jakosky, H.H. Kieffer, P.R. Christensen, High-Resolution thermal inertia mapping from the Mars Global Surveyor Thermal Emission Spectrometer, Icarus, 148, 437-455, (2000)

M.T. Mellon, R. L. Fergason, N. E. Putzig (2008), The thermal inertia of the surface of Mars, in The Martian Surface: Composition, Mineralogy, and Physical Properties, edited by J. F. Bell III, Cambridge University Press.

H.J. Melosh, (1989), Impact Cratering: A Geologic Process, Oxford University Press, London.

G.G. Michael, G. Neukum (2010), Planetary surface dating from crater size-frequency distribution measurements: Partial resurfacing events and statistical age uncertainty, Earth Planet. Sci. Lett., 294(3–4), 223–229, doi:10.1016/j.epsl.2009.12.041.

D. Mimoun, N. Murdoch, P. Lognonné, K. Hurst, W. T. Pike, J. Hurley, T. Nébut, W. B. Banerdt, SEIS Team (2017) The noise model of the SEIS seismometer of the InSight mission to Mars, Space Sci. Rev., 211, 383-428, doi:10.1007/s11214-017-0409-x

M.E. Minitti, Kah, L.C., Yingst, R.A., Edgett, K.S., Anderson, R.C., Beegle, L.W., Carsten, J.L., Deen, R.G., Goetz, W., Hardgrove, C. Harker, D.E., 2013. MAHLI at the Rocknest sand shadow: Science and science-enabling activities. J. Geophys. Res., Planets, 118(11), 2338-2360.

S. Monin, Obukhov, A., 1954. Basic laws of turbulent mixing in the ground layer of the atmosphere. Tr. Akad. Nauk SSSR Geofiz. Inst. 24, 163–187.

H.J. Moore, R. E. Hutton, G. D. Clow, C. R. Spitzer, Physical properties of the surface materials of the Viking landing sites on Mars, U.S. Geol. Surv. Prof. Pap., 1389, 222pp., 2plates, 1987.

H.J. Moore, D. Bickler, J. Crisp, et al., Soil-like deposits observed by Sojourner, the Pathfinder rover, J. Geophys. Res. 104, 8729–46, 1999.

J.E. Moores, Lemmon, M.T., Kahanpää, H., Rafkin, S.C., Francis, R., Pla-Garcia, J., Bean, K., Haberle, R., Newman, C., Mischna, M. Vasavada, A.R., 2015. Observational evidence of a suppressed planetary boundary layer in northern Gale Crater, Mars as seen by the Navcam instrument onboard the Mars Science Laboratory rover. Icarus, 249, pp.129-142.

P. Morgan, Grott M., Golombek M., Delage P., Knapmeyer-Endrun B., Piqueux S., Daubar I. J., Charalambous C., Pike T., Müller N., Hagermann A., Siegler M., Lichtenheldt R., Teanby

N., Kedar S., 2018, A pre-landing assessment of regolith properties at the InSight landing site, Space Science Reviews, this issue.

K. Mueller, Golombek, M. P. (2004). Compressional structures on Mars. Annu. Rev. Earth Planet. Sci., 32, 435–464, doi:10.1146/annurev.earth.32.101802.120553.

N. Murdoch, B. Kenda, T. Kawamura, A. Spiga, P. Lognonné, D. Mimoun, W. B. Banerdt (2017a) Estimations of the seismic pressure noise on Mars determined from Large Eddy Simulations and demonstration of pressure decorrelation techniques for the Insight mission, Space Sci. Rev., 211, 457-483, doi:10.1007/s11214-017-0343-y

N. Murdoch, D. Mimoun, R. F. Garcia, W. Rapin, T. Kawamura, P. Lognonné (2017b) Evaluating the wind-induced mechanical noise on the InSight seismometers, Space Sci. Rev., 211, 419-455, doi:10.1007/s11214-016-0311-y

T.A. Mutch, R. E. Arvidson, A. B. Binder, E. A. Guinness, E.C. Morris, The geology of the Viking Lander 2 site, J. Geophys. Res. 82, 4452–67, 1977.

G. Neugebauer, G. Munch, H. Kieffer, J. S.C. Chase, and E. Miner (1971), Mariner 1969 infrared radiometer results: Temperatures and thermal properties of the martian surface, Astron. J., 76, 719-728.

R.T. Nishiyama, A.J. Bedard, 1991. A "Quad-Disc" static pressure probe for measurement in adverse atmospheres: With a comparative review of static pressure probe designs. Rev. Sci. Instr., 62, 2193.

S.A. Nowicki, P.R. Christensen (2007), Rock abundance on Mars from the Thermal Emission Spectrometer, Journal of Geophysical Research, 112, E05007, doi:05010.01029/02006JE002798.

V.R. Oberbeck, W.L. Quaide, Genetic implications of lunar regolith thickness variations. Icarus 9, 446–465 (1968)

L. Ojha, S.E. Smrekar, D. Nunes, Geophysical Characterization of Elysium Planitia: Implications for the InSight Mission (in preparation) 2018.

D.A. Paige, Golombek, M.P., Maki, J.N., Parker, T.J., Crumpler, L.S., Grant, J.A., Williams, J.P., 2007, MER small crater statistics: Evidence against recent quasi-periodic climate variations, The Seventh International Conference on Mars, July 9-13, 2007, Pasadena, CA, Abstract #3392, Lunar and Planetary Institute, Houston (CD-ROM).

T.J. Parker, Calef, F. J., Golombek, M. P., Hare, T. M., 2012, High-resolution basemaps for localization, mission planning, and geologic mapping at Meridiani Planum and Gale crater 43rd Lunar and Planetary Science, Abstract #2535, Lunar and Planetary Institute, Houston.

T.J. Parker, Malin, M. C., Calef, F. J., Deen, R. G., Gengl, H. E., Golombek, M. P., Hall, J. R., Pariser, O., Powell, M., Sletten, R. S., the MSL Science Team, 2013, Localization and 'contextualization' of Curiosity in Gale crater, and other landed Mars missions: 44th Lunar and Planetary Science, Abstract #2534, Lunar and Planetary Institute, Houston.

G.H. Peters, W. Abbey, G.H. Bearman, G.S. Mungas, J.A. Smith, R.C. Anderson, S. Douglas, L.W. Beegle, Mojave Mars simulant—characterization of a new geologic Mars analog. Icarus **197**, 470–479 (2008). doi:10.1016/j.icarus.2008.05.004

G.M. Pharr, W.C. Oliver, and F.R. Brotzen, On the generality of the relationship among contact stiffness, contact area, and elastic modulus during indentation. Journal of materials research, 1992. **7**(3): p. 613-617.

R.J. Pike (1974), Depth/diameter relations of fresh lunar craters: Revision from spacecraft data, Geophys. Res. Lett., 1, 291–294, doi:10.1029/GL001i007p00291.

S. Piqueux, P.R. Christensen, A model of thermal conductivity for planetary soils: 2. Theory for cemented soils. J. Geophys. Res. 114, E09006 (2009). doi:10.1029/2008je003309

S. Piqueux, P.R. Christensen, Temperature-dependent thermal inertia of homogeneous Martian regolith. J. Geophys. Res. 116, E07004 (2011). doi:10.1029/2011je003805

T. Platz, G. Michael, K. L. Tanaka, J. A. Skinner Jr., C. M. Fortezzo (2013), Crater-based dating of geological units on Mars: Methods and application for the new global geological map, Icarus, 225, 806–827, doi:10.1016/j.icarus.2013.04.021.

D.H. Plemmons, Mehta, M., Clark, B.C., Kounaves, S.P., Peach, L.L., Rennó, N.O., Tamppari, L.K., Young, S.M.M., 2008. Effects of the Phoenix Lander descent thruster plume on the Martian surface. J. Geophys. Res. 113, E00A11. doi:10.1029/2007JE003059

A.-C. Plesa, M. Grott, M. T. Lemmon, et al., Interannual perturbations of the Martian surface heat flow by atmospheric dust opacity variations, J. Geophys. Res. Planets, 121, 2166–2175, (2016)

J. Poganski, N.I. Kömle, G. Kargl, et al., Extended pile driving model to predict the penetration of the Insight/HP^3 Mole into the martian soil, Space Sci. Rev. 211, 1–4, 237–237 (2017a)

J. Poganski et al., DEM modelling of a dynamic penetration process on Mars as a part of the NASA InSight Mission. Procedia Engineering, (2017b) 175: 43-50.

H.-G. Poulos, E.-H. Davis (1974) Elastic solutions for soil and rock mechanics. Wiley, New York.

B.A. Preblich, A.S. McEwen, D.M. Studer (2007), Mapping rays and secondary craters from Martian crater Zunil. J. Geophys. Res. Planets 112. Doi:10.1029/2006JE002817.

M.A. Presley, P.R. Christensen, Thermal conductivity measurements of particulate materials, Part I: A review. J. Geophys. Res. 102, 6535–6549 (1997a)

M.A. Presley, P.R. Christensen, Thermal conductivity measurements of particulate materials, Part II: Results. J. Geophys. Res. 102, 6551–6566 (1997b)

M.A. Presley, P.R. Christensen, The effect of bulk density and particle size sorting on the thermal conductivity of particulate materials under Martian atmospheric pressures, J. Geophys. Res., 102(E4), 9221-9229 (1997c).

M.A. Presley, R.A. Craddock, Thermal conductivity measurements of particulate materials: 3. Natural samples and mixtures of particle sizes, J. Geophys. Res., 111, E09013, (2006).

N.E. Putzig, M.T. Mellon, Apparent thermal inertia and the surface heterogeneity of Mars. Icarus 191(1), 68–94 (2007). doi:10.1016/j.icarus.2007.1005.1013

D. Reiss, Lorenz, R.D., 2016. Dust devil track survey at Elysium Planitia, Mars: implications for the InSight landing sites. Icarus, 266, pp.315-330.

A. Rivoldini, T. Van Hoolst, O. Verhoeven, A. Mocquet, V. Dehant. Geodesy constraints on the interior structure and composition of Mars. Icarus, 213:451–472, June 2011. doi: 10.1016/j.icarus.2011.03.024.

D.M. Rubin, Hunter, R.E., Bedform Alignment in Directionally Varying Flows. Science 237, 276–278, Jul. 1987.

S. Ruff, P.R. Christensen, Bright and dark regions on Mars: particle size and mineralogical characteristics based on Thermal Emission Spectrometer data. J. Geophys. Res. 107(E12), 5127 (2002). doi:10.1029/2001JE001580

K.D. Runyon, Bridges, N. T., Ayoub, F., Newman, C. E., Quade, J. J., 2017. An integrated model for dune morphology and sand fluxes on Mars. Earth Planet. Sci. Let. 457, 204–212.

C. Schmelzbach, Green, A.G., Horstmeyer, H., 2005. Ultra-shallow seismic reflection imaging in a region characterized by high source-generated noise. Near Surface Geophysics 3, 33–46.

R.F. Scott, (1987). Failure. Géotechnique, 37(4), 423–466.

R.A. Schultz, (2000). Localization of bedding-plane slip and backthrust faults above blind thrust faults: Keys to wrinkle ridge structure. J. Geophys. Res., 105, 12 035–12 052.

K.D. Seelos, F.P. Seelos, C.E. Viviano- Beck, S.L. Murchie, R.E. Arvidson, B.L. Ehlmann, A. A. Fraeman (2014), Mineralogy of the MSL Curiosity landing site in Gale crater as observed by MRO/CRISM, Geophys. Res. Lett., 41, 4880–4887, doi:10.1002/ 2014GL060310.

E. Sefton-Nash, Teanby, N. A., Newman, C., Clancy, R. A., Richardson, M. I., 2014. Constraints on Mars' recent equatorial wind regimes from layered deposits and comparison with general circulation model results. Icarus 230, 81–95.

K. Seiferlin, P. Ehrenfreund, J. Garry, K. Gunderson, E. Hütter, G. Kargl, A. Maturilli, J.P. Merrison, Simulating martian regolith in the laboratory. Planet. Space Sci. **56**(15), 2009–2025 (2008)

A. Seiff, J.E. Tillman, J.R. Murphy, J.T. Schofield, D. Crisp, J.R. Barnes, C. LaBaw, C. Mahoney, G.R. Wilson, R. Haberle, 1997. The atmosphere structure and meteorology instrument on the Mars Pathfinder Lander. J. Geophys. Res., 102, 4045-4056.

K.D. Seelos, F. P. Seelos, C. E. Viviano- Beck, S. L. Murchie, R. E. Arvidson, B. L. Ehlmann, A. A. Fraeman (2014), Mineralogy of the MSL Curiosity landing site in Gale crater as observed by MRO/CRISM, Geophys. Res. Lett., 41, 4880–4887, doi:10.1002/ 2014GL060310.

C. Sens-Schönfelder, Larose, E. (2008): Temporal changes in the lunar soil from correlation of diffuse vibrations. - Physical Review E, 78, 4, 045601(R). DOI: doi.org/10.1103/PhysRevE.78.045601

A. Shaw, R.E. Arvidson, R. Bonitz, J. Carsten, H.U. Keller, M.T. Lemmon, M.T. Mellon, M. Robinson, A. Trebi-Ollennu (2009), Phoenix soil physical properties investigation, J. Geophys. Res., 114, E00E05, doi:10.1029/2009JE003455.

M.A. Siegler, S.E. Smrekar, M. Grott, et al., The InSight Mars lander and its effect on the subsurface thermal environment, Space Sci. Rev., 211, 1–4, 259–275 (2017)

G.G. Sorrells, J. A. McDonald, Z. A. Der, E. Herrin (1971) Earth motion caused by local atmospheric pressure changes, Geophys. J. R. Astr. Soc., 26, 83-98

D.E. Smith et al., Mars Orbiter Laser Altimeter (MOLA): experiment summary after the first year of global mapping of Mars. J. Geophys. Res. 106, 23,689–23,722 (2001)

P.H. Smith, et al. (2009), H_2O at the Phoenix landing site, Science, 325, 58–61.

A. Spiga et al. 2018 Atmospheric science with InSight, Space Science Reviews, this issue, (2018)

T. Spohn, M. Grott, et al., The Heat Flow and Physical Properties Package (HP^3) for the InSight Mission, Space Science Reviews, this issue, (2018)

P.M. Stella, J.A. Herman, The Mars surface and solar array performance, in 35th IEEE Photovoltaic Specialists Conference, Honolulu, 20–25 June 2010 (2010), pp. 002631–002635. doi:10.1109/PVSC.2010.5617185

R. Sullivan, Greeley, R., Kraft, M., Wilson, G., Golombek, M., Herkenhoff, K., Murphy, J., Smith, P., 2000. Results of the Imager for Mars Pathfinder windsock experiment. J. Geophys. Res. 105, 24547–24562.

R. Sullivan, R. Anderson, J. Biesiadecki, T. Bond, H. Stewart (2011), Cohesions, friction angles, and other physical properties of Martian regolith from Mars Exploration Rover wheel trenches and wheel scuffs, J. Geophys. Res., 116, E02006, doi:10.1029/2010JE003625.

J.L. Sutton, Levoy, C. B., Tillman, J. E., 1978. Diurnal variations of the Martian surface layer meteorological parameters during the first 45 sols at two Viking Lander sites. J. Atmos. Sci. 35, 2346–2355.

J. Sweeney, N. H. Warner, M. P. Golombek, R. L. Kirk, R. L. Fergason, A. Pivarunas (2016), Crater degradation and surface erosion rates at the InSight landing site, western Elysium Planitia, Mars, 47th Lunar Planet. Sci. Conf., Abstract 1576.

J. Sweeney, N.H. Warner, M.P. Golombek, V. Ganti, M.P. Lamb, R.L. Fergason, R.L. Kirk, F.J. Calef (2018), Degradation of one-hundred-meter-scale impact craters on Mars with implications for surface process rates in the Hesperian and Amazonian, J. Geophys. Res. Planets. In review

K.L. Tanaka, J.A. Skinner, J.M. Dohm, R.P. Irwin, E.J. Kolb, C.M. Fortezzo, T. Platz, G.G. Michael, T.M. Hare (2014), Geologic Map of Mars, 1:20,000,000, USGS Scientific Investigations Map 3292.

T. Tanimoto, Eitzel M, Yano T (2008) The noise cross-correlation approach for Apollo 17 LSPE data: Diurnal change in seismic parameters in shallow lunar crust. Journal of Geophysical Research 113: E08011, doi:10.1029/2007JE003016

P.A. Taylor, D.C. Catling, M. Daly, C.S. Dickinson, H.P. Gunnlaugsson, A-M. Harri, C.F. Lange, 2008. Temperature, pressure and wind instrumentation in the Phoenix meteorological package. J. Geophys. Res. 113, E00A10, doi:10.1029/2007JE003015.

N.A. Teanby, Stevanovi´c, J., Wookey, J., Murdoch, N., Hurley, J., Myhill, R., Bowles, N. E., Calcutt, S. B., Pike, W. T.. Seismic coupling of short-period wind noise through Mars' regolith for NASA's InSight lander. Space Sci. Rev. (2017) 211: 485. https://doi.org/10.1007/s11214-016-0310-z

E. Theilig, Greeley, R. (1986) Lava flows on Mars: Analysis of small surface features and comparisons with terrestrial analogs. J. Geophys. Res., 91(B13), E193–E206, doi: 10.1029/JB091iB13p0E193.

B.J. Thomson, P. H. Schultz, N.T. Bridges, 2008, Extracting scientific results from robotic arm support operations: A technique for estimating the density and composition of rocks on Mars, Mars 4, 27-32, 2008; doi:10.1555/mars.2008.0003

A. Trebi-Ollennu et al. 2018 IDA, Space Science Reviews, this issue

J. Vaucher, D. Baratoux, N. Mangold, P. Pinet, K. Kurita, M. Grégoire, The volcanic history of central Elysium Planitia: implications for martian magmatism. Icarus 204, 418–442 (2009)

A.F. Vaughan, et al., 2010. Pancam and microscopic imager observations of dust on the Spirit rover: Cleaning events, spectral properties, and aggregates. Mars 5, 129–145. http://dx.doi.org/10.1555/mars.2010.0005.

A.R. Vasavada, S. Piqueux, K.W. Lewis, et al, Thermophysical properties along Curiosity's traverse in Gale crater, Mars, derived from the REMS ground temperature sensor, Icarus, 284, 372-386 (2017) doi:10.1016/j.icarus.2016.11.035.

C.A. Verba, Geissler, P.E., Titus, T.N. Waller, D., 2010. Observations from the high resolution imaging science experiment (HiRISE): Martian dust devils in Gusev and Russell craters. J. Geophys. Res. Planets, 115(E9). Doi: 10.1029/2009JE003498

VICAR, 2016, Video Image Communication And Retrieval image processing software system, Open Source Release 2, http://www-mipl.jpl.nasa.gov/vicar_open.html

C. Vrettos, Shear strength investigations for a class of extra-terrestrial analogue soils. J. Geotech. Geoenviron. Eng. **138**, 508–515 (2012)

C. Vrettos, A. Becker, K. Merz, L. Witte, Penetration tests in a mold on regolith quasi-analogues at different relative densities, Earth & Space 2014, 14th ASCE International Conference on Engineering, Science, Construction and Operations in Challenging Environments (2014)

G.P.L. Walker, (1991), Structure, and origin by injection of lava under surface crust, of tumuli, "lava rises", "lava-rise pits", and "lava-inflation clefts" in Hawaii, Bull. Volcanol., 53(7), 546-558.

N.H. Warner, S. Gupta, F. J. Calef, P. Grindrod, K. Goddard (2015), Minimum effective area for high resolution crater counting of martian terrains, Icarus, 245, 198–240, doi:10.1016/j.icarus.2014.09.024.

N.H. Warner, Golombek, M. P., Sweeney, J., Fergason, R., Kirk, R., Schwartz, C., 2017, Near surface stratigraphy and regolith production in southwestern Elysium Planitia, Mars: Implications for Hesperian-Amazonian terrains and the InSight lander mission: Space Science Reviews, 211, 147-190, DOI 10.1007/s11214-017-0352-x.

T.R. Watters, (1988). Wrinkle ridge assemblages on the terrestrial planets. J. Geophys. Res., 93, 10 236–10 254.

W.A. Watters, L.M. Geiger, M.A. Fendrock, R. Gibson (2015), Morphometry of small recent impact craters on Mars: Size and terrain dependence, short-term modification, J. Geophys. Res. Planets, 210(2), 226–254, doi:10.1002/2014JE004630.

S.G. Wells, J.C. Dohrenwend, L.D. McFadden, B.F. Turrin, K.D. Mahrer, Late Cenozoic landscape evolution on lava flow surfaces of the Cima volcanic field, Mojave Desert, California. Geol. Soc. Am. Bull. 96, 1518–1529 (1985)

S.C. Werner, K.L. Tanaka, Redefinition of the crater-density and absolute-age boundaries for the chronostratigraphic system of Mars. Icarus 215, 603–607 (2011)

M.A. Wieczorek et al. (2012) The crust of the Moon as seen by GRAIL, Science 339(6120), 671–675, DOI: 10.1126/science.1231530.

A. Wilkinson, A. DeGennaro, Digging and pushing lunar regolith: Classical soil mechanics and the forces needed for excavation and traction. Journal of Terramechanics, 2007. **44**(2): 133-152.

M.M. Withers, R.C. Aster, C.J. Young, E.P. Chael, High-frequency analysis of seismic background noise as a function of wind speed and shallow depth. Bull. Seismol. Soc. Am. 86, 1507–1515 (1996)

R.A. Yingst, Haldemann, A.F.C., Biedermann, K.L., et al., 2007. Quantitative morphology of rocks at the Mars Pathfinder landing site. J. Geophys. Res. 112, E06002. doi:10.1029/2005JE002582.

R.A. Yingst, Crumpler, L., Farrand, W.H., et al., 2008. Morphology and texture of particles along the Spirit rover traverse from sol 450 to sol 745. J. Geophys. Res. 113, E12S41. doi:10.1029/2008JE003179.

R.A. Yingst, et al., 2013. Characteristics of pebble- and cobble-sized clasts along the Curiosity rover traverse from Bradbury Landing to Rocknest. J. Geophys. Res. Planets 118, 2361–2380. doi:10.1002/2013JE004435.

C.F. Yoder, Standish E.M., 1997, Martian precession and rotation from Viking lander range data, J. Geophys. Res., 102(E2), pp. 4065-4080.